Neural circuit analysis of the dorsal nucleus of the lateral lemniscus and new viral approaches to neural circuit analysis in Mongolian gerbils

Christian Porres

Dissertation
der Fakultät für Biologie
der Ludwig–Maximilians–Universität
München

vorgelegt von
Christian Porres
aus Köln

München, den 05.07.2012

Erstgutachter: Prof. Dr. Benedikt Grothe
Zweitgutachter: Prof. Dr. Hans Straka
Tag der mündlichen Prüfung: 08.11.2012

"... porque ves allí, amigo Sancho Panza,
donde se descubren treinta o pocos más desaforados gigantes,
con quien pienso hacer batalla y quitarles a todos las vidas, ..."

Don Quijote de la Mancha

"... que hay algunos que se cansan en saber y averiguar cosas que,
después de sabidas y averiguadas,
no importan un ardite al entendimiento ni a la memoria."

Don Quijote de la Mancha

Contents

Zusammenfassung

Auditorische Stimuli werden in verschiedenen parallel und in Serie angeordneten neuralen Netzwerken des auditorischen Hirnstamms verarbeitet. Im ersten Teil dieser Dissertation wird die synaptische Integration exzitatorischer Eingänge zu Neuronen des dorsalen Nukleus des lateralen Lemniscus (DNLL) der mongolischen Wüstenrennmaus untersucht. Der zweite Teil der Arbeit betrachtet die Möglichkeit des Einsatzes viraler Vektoren in der mongolischen Wüstenrennmaus. Das Ziel war es, die Palette der verfügbaren Methoden zur Analyse neuronaler Netzwerke in diesen Tieren um einen genetischen Ansatz zu erweitern.

Der DNLL erhält exzitatorische Eingänge vom superioren Olivenkernkomplex (SOC) und sendet GABAerge inhibitorische Projektionen zum kontralateralen DNLL und zu beiden inferioren Colliculi (ICs). Diese GABAerge Inhibition kann den auslösenden auditorischen Reiz für mehrere Millisekunden überdauern und unterscheidet sich damit grundsätzlich von der im SOC vorherrschenden schnellen, glycinergen Inhibition. Es wird vermutet, daß diese persistierende Inhibition (PI) die weitere Verarbeitung räumlicher Information von Echos unterdrückt und damit eine neuronale Grundlage zur Schallquellenlokalisation in nachhallenden Umgebungen bildet. Die Mechanismen zur Generierung der PI sind nicht vollständig erklärt. Eine mögliche Erklärung zielt auf den Mechanismus der Neurotrnasmitterausschüttung in DNLL Neuronen. Demzufolge könnten Neurotransmitter “spill over” oder asynchrone Transmitterausschüttung die GABAerge Inhibition der DNLL Neurone zeitlich verlängern. Ein zweiter Mechanismus argumentiert, daß die Aktivität in DNLL Neuronen durch die Integration exzitatorischer synaptischer Eingänge zeitlich ausgedehnt wird und somit auch die Inhibition die die DNLL Neurone auf ihre Zielzellen ausüben. In dieser Arbeit wurde mit Hilfe der “patch-clamp” Methode die Integration exzitatorischer Eingänge in DNLL Neuronen untersucht mit dem Ziel die mögliche Existenz dieses zweiten Mechanismus zu zeigen. Die Ergebnisse zeigen, daß fünf simultan erregte exzitatorische Fasern benötigt werden, die im Durchschnitt ∼18 Vesikel ausschütten, um ein Aktionspotential (AP) in einem DNLL Neuron auszulösen. Ein einzelner starker präsynaptischer Stimulationspuls ist außerdem ausreichend mehrere APs auszulösen. Die Input-Output Funktionen (IO-Fs) von DNLL Neuronen sind abhängig von NMDA Rezeptorströmen, welche die Aktivität von DNLL Neuronen zeitlich verlängern. Anders als Kalziumleitfähigkeiten sind auch Kaliumleitfähigkeiten in der Lage die IO-Fs von DNLL Neuronen zu beeinflussen. Die NMDA Rezeptorstrom abhängige Aktivitätsverlängerung in

DNLL Neuronen ist sowohl in juvenilen, als auch in adulten Tieren vorhanden und gipfelt in einer Verlängerung der GABAergen Inhibition die von DNLL Neuronen generiert wird. Somit ist die Integration exzitatorischer Eingänge in DNLL Neuronen grundsätzlich geeignet zum Enstehen der PI beizutragen.

Virale Vektoren werden benutzt um den genetischen Inhalt eines Organismus zu verändern. In mongolischen Wüstenrennmäusen, von denen es derzeit keine transgenen Tierlinien gibt, können virale Vektoren benutzt werden diesen Nachteil auszugleichen. Wir haben lentivirale Vektoren und Vektoren basierend auf dem Semliki Forest Virus (SFV) stereotaktisch in den IC und den medialen Nukleus des Trapezkörpers (MNTB) von mongolischen Wüstenrennmäusen injiziert. Die lentiviralen Konstrukte induzieren die Expression des transgenen Proteins im IC, nicht aber in MNTB Neuronen. Der SFV-Vektor ist in der Lage in beiden Nuklei Expression auszulösen, entfaltet aber zusätzlich eine stark zytotoxische Wirkungen. In einer weiteren Experimentreihe wurde ein eGFP exprimierender attenuierter Pseudorabiesstamm (PRV-152) in den IC injiziert. Dieser Vektor ist in der Lage alle Nuklei des auditorischen Hirnstamms retrograd der Injektionsstelle in juvenilen und adulten mongolischen Wüstenrennmäusen zu infizieren. Die PRV-152 Infektion breitet sich nach etwa 20 Stunden über die erste Synapse zu infizierten Zellen zweiter Ordnung aus. Die PRV-152 Infektion kann ebenfalls vom DNLL ausgehend ausgelöst werden und zeigt einen ausgeprägten Neurotropismus. Die induzierte Expression des eGFPs ist hoch und ermöglicht eine deutliche Darstellung der infizierten Neurone, so daß PRV-152 ein vielversprechendes Werkzeug zur anatomischen Untersuchung neuronaler Netzwerke darstellt. Ebenfalls wurde untersucht, ob die PRV-152 Infektion zusätzlich die elektrophysiologische Untersuchung der infizierten Neurone erlaubt. 37 % der infizierten Neurone erster Ordnung und 78 % der infizierten Neurone zweiter Ordnung zeigen eine signifikant heruntergesetzte Erregbarkeit. Diese Ergebnisse zeigen deutlich, daß PRV-152 eine anatomische, nicht aber eine elektrophysiologische Untersuchung neuronale Netzwerke ermöglicht.

Abstract

Auditory stimuli are processed by several parallel and serial neural circuits in the auditory brainstem. In the first part of this PhD thesis, synaptic integration of excitatory inputs in the neural network of the dorsal nucleus of the lateral lemniscus (DNLL) in Mongolian gerbils is investigated. The second part of this study analyses the feasibility of the use of viral vectors in Mongolian gerbils. This work aims to add to the available methods for neural circuit analysis in these animals by establishing tools for genetic manipulation.

The DNLL receives excitatory inputs from the superior olivary complex (SOC) and provides GABAergic inhibition to its contralateral counterpart and both inferior colliculi (ICs). This GABAergic inhibition can outlast the triggering auditory stimulus by tens of milliseconds and thus differs substantially from the fast glycinergic inhibition prevailing in the SOC. It is thought that this persistent inhibition (PI) suppresses further processing of sound source information cues of lagging sounds, thereby providing the neuronal basis for sound localisation in reverberant environments. The mechanisms which PI is generated are still under debate. One hypothesized mechanism focuses on the output mechanism in DNLL neurons, favouring transmitter spillover or asynchronous release to evoke PI. A second mechanism states that integration of excitatory inputs leads to temporally extended activity in DNLL neurons, thereby prolonging the GABAergic output. Here, we tested *in vitro* the feasibility of the integration based mechanism in Mongolian gerbils. We analyzed the integration of excitatory inputs to DNLL neurons and found that five simultaneously stimulated excitatory fibres, each releasing on average ∼18 vesicles are sufficient to trigger a single action potential (AP) in a DNLL neuron. A strong presynaptic stimulation pulse could trigger multiple APs. The input-output functions (IO-Fs) of DNLL neurons were dependent on NMDA receptor (NMDAR) mediated currents, which temporally extended the neuron's activity. The synaptic IO-Fs of DNLL neurons could also be modulated by voltage gated potassium, but not by calcium conductances. The NMDAR dependent activity amplification, which is maintained into adult stages, is shown to prolong the GABAergic output of DNLL neurons, thus contributing to PI generation.

Viral vectors are widely used to alter the genetic content of a host organism. In Mongolian gerbils this approach may be suitable to compensate for the lack of genetic strategies in neural circuit analysis such as transgenic animal lines. Lentiviral and Semliki forest viral vectors were stereotactically injected into the IC or the

medial nucleus of the trapezoid body (MNTB) in Mongolian gerbils. The lentiviral constructs were able to induce expression of the transgenic protein in the IC but not in MNTB principal neurons. The Semliki forest viral vector induced expression in both nuclei but also caused strong cytotoxic effects in the infected cells. In a further experiment, an eGFP expressing pseudorabies virus based on the attenuated Bartha strain (PRV-152) was stereotactically injected into the IC and was able to retrogradely infect the nuclei of the auditory brain stem in juvenile and adult Mongolian gerbils. PRV-152 spread synaptically to 2^{nd} order neurons by $\sim$20 hours after injection. Infection could also be started in the DNLL and showed a strongly pronounced neurotropism. The virus induced eGFP expression was high and allowed for a detailed visualization of the infected neurons, establishing PRV-152 as an effective tool for anatomical circuit analysis. The feasibility of using this virus in conjunction with electrophysiological investigations was also tested. 37 % of 1^{st} and 78 % of 2^{nd} order infected neurons show a significant decrease of excitability, which impedes the use of PRV-152 in combination with electrophysiological recordings for physiological analysis of neural circuits.

1 Introduction

Sound is a mechanical wave, which is transmitted in a medium by pressure fluctuations from the equilibrium pressure. Each movement in the medium will move the composing molecules and thereby change, at a restricted location, the equilibrium pressure of the medium. As a consequence, all movement necessarily produces sound. Thus, sounds provide us with an exhaustive image of the world around us. The interpretation of this sound image is limited by the abilities and specialisations of the listener's sensory organs and their ability to process and interpret this sound information. Humans, for example, are able to detect sound waves of frequencies between 20 Hz to 20 kHz (Moore, 1977), bats use ultrasonic sound based echolocation for orientation and hunting (Griffin and Galambos, 1941) and Asian and African elephants are capable of communicating over a distance of several kilometres in the infrasound frequency range (Payne et al., 1986; Poole et al., 1988). One highly important cue encoded in the sound image of the surroundings is the localisation of the sound source. Humans are able to distinguish pure tone sound sources with a single degree resolution (Mills, 1958; Perrott and Saberi, 1990). Elephants and pigs localise sounds with similar acuity (Heffner and Heffner, 1980, 1989), while animals with smaller head size like the Mongolian gerbil show less elaborate abilities for localisation tasks (Heffner and Heffner, 1988; Maier and Klump, 2006; Maier et al., 2008). However, fast and accurate sound source localisation is of importance for many behaviours ranging from mating behaviour to predator-prey interactions. Hence, the reception and processing of sounds and the fast and exact localisation of

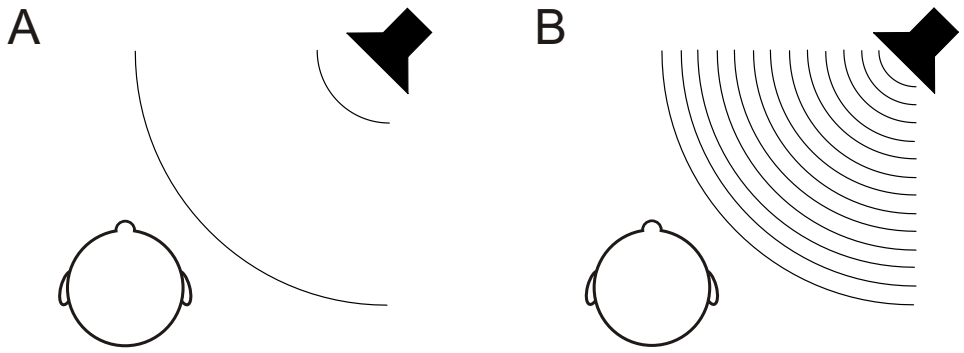

Figure 1.1: Cues in sound localisation A Sound waves with a period length longer than the distance between the listener's ears are processed using interaural time differences (ITDs). Sounds, if not generated directly in front of the listener (0 ITD), arrive at both ears with a certain time delay. This difference in arrival time is used to localize the sound source of low frequency sounds (below 1.5 kHz in humans). **B** Sound waves with a period length shorter than the distance between the listener's ears are processed using interaural intensity differences (IIDs). For those higher frequencies (beyond 1.5 kHz in humans) sound intensity is significantly attenuated by the listeners head. Therefore the intensity difference between both ears can be used to localize a sound source. Modified from Grothe et al., 2010.

the sound source is essential for the survival of the individual and the entire species.

Sound localisation in the azimuthal plane is based on the comparison of the inputs to both ears. The computing of these binaural cues is then done across several neural circuits, processing in parallel and in series along the ascending auditory pathway (for review: Pollak et al., 2003; Grothe et al., 2010). When a sound originates from elsewhere other than directly before the listener, it will first arrive at one ear and then, with a short time delay, at the other (see fig. 1.1 A). This difference in arrival time at both ears is called interaural time difference (ITD). Additionally, the listener's head attenuates the intensity of the sound and creates an acoustic shadow on the second ear, which results in an amplitude difference between both ears (see fig. 1.1 B; Thompson, 1882). This intensity difference at the two ears is called interaural intensity difference (IID). The Duplex theory of azimuthal sound localisation established ITDs and IIDs as the two cues used to localize sound sources in the azimuthal plane (Rayleigh, 1907). Generally, higher frequency sounds (beyond $\sim$ 1.5 kHz in humans) are mainly processed as IIDs (Thompson, 1882) and

lower frequency sounds as ITDs. This difference in processing is necessary as lower frequency sounds are not attenuated significantly by the head and difference in binaural arrival times of higher frequency sounds cannot be processed unambiguously as the period length of the sound wave is shorter than the listeners head (Palmer and Russell, 1986).

There are exceptions to this general rule in that lower frequency sounds can produce significant IIDs in the near field (<1-2 m, Brungart and Rabinowitz, 1999; Shinn-Cunningham et al., 2000) and high frequency sounds with a low frequency amplitude modulation envelope can generate ITDs (Yost et al., 1971; Griffin et al., 2005).

1.1 Sound processing in mammals: from the outer ear to the superior olivary complex

After passing the outer ear (*pinna* and *meatus*), sound waves cause vibrations in the tympanic membrane. These movements are mechanically transmitted through the middle ear via the three ossicles (*malleus, incus, stapes*) to the oval window and the adjoining inner ear. The inner ear or cochlea is a spiral-shaped structure composed of three fluid filled chambers: *scala tympani, scala vestibuli and scala media*. Vibrations of the oval window are transduced to the perilymph of the scala tympani and scala vestibuli and the endolymph of the scala media. The movements of these viscous fluids are finally relayed to the basilar membrane at the bottom of the scala media on which the organ of corti is located. In the organ of corti mechanotransducers, the inner hair cells, generate a graduated electric potential. This graduated signal is then transformed via the specialised ribbon synapses into action potentials (APs) in neurons of the spiral ganglion, which project to the cochlear nucleus (CN). The CN then provides inputs to the nuclei of the superior olivary complex. Here, in the lateral and medial superior olive (LSO, MSO) binaural

inputs are processed for the first time in the auditory brainstem.

Anatomical and cellular specialisations ensure that information of an auditory stimulus is preserved through the auditory pathway. Due to the structure of the basilar membrane (decreasing stiffness and increasing width from base to apical end), higher sound frequencies are transduced by inner hair cells located at the base of the basilar membrane and lower sound frequencies by hair cells at the apical end of the membrane (von Békésy, 1960). Thus, sound frequencies are mapped tonotopically along the cochlea. This "frequency to place" organisation is continued in auditory nerve fibres and throughout the nuclei of the auditory brainstem.

Timing information of an auditory stimulus is transferred by the phenomenon of "phase locking" (for frequencies up to 2-3 kHz; Galambos and Davis, 1943; Kiang et al., 1965). Spiral ganglion neurons and later on neurons of auditory nuclei involved in temporal coding preserve timing information by firing APs to a specific phase of a sound wave cycle. Phase locking is a prerequisite for ITD coding in the MSO.

1.2 Two parallel neural circuits process IIDs and ITDs in the superior olivary complex

1.2.1 IID processing in the neural circuit of the LSO

IIDs are processed in the neural circuit of the LSO (see fig. 1.2 A). LSO neurons receive excitatory inputs from spherical bushy cells of the ipsilateral anteroventral cochlear nucleus (AVCN; Stotler, 1953; Cant and Casseday, 1986; Thompson and Thompson, 1987) and fast glycinergic inhibition via the ipsilateral MNTB, which itself is driven by globular bushy cells of the contralateral AVCN (see fig. 1.2 A; Moore and Caspary, 1983; Kuwabara et al., 1991). The MNTB acts as a fast and precise inhibitory relay and translates the excitatory inputs from the contralateral ear reliably into inhibition thereby preserving the timing information content (Held,

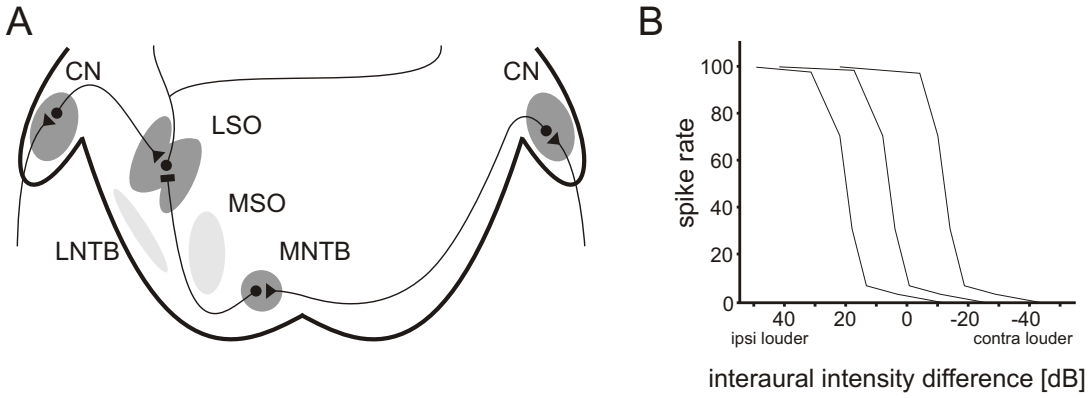

Figure 1.2: Interaural intensity differences (IIDs) A In mammals IIDs are computed in the lateral superior olive (LSO). LSO neurons receive excitatory inputs from the ipsilateral cochlear nucleus (CN) and inhibitory inputs from the contralateral CN via the medial nucleus of the trapezoid body (MNTB, modified from Couchman, 2011). **B** These example IID-functions show the decreasing firing rate of LSO neurons when the sound stimulus at the ear contralateral to the LSO gets louder. This is due to increased inhibition from the MNTB and decreased ipsilateral excitation. Sound source information in the LSO is represented as a population code.

1893; Moore and Caspary, 1983; Kuwabara et al., 1991; Forsythe, 1994; Joris and Yin, 1995; Taschenberger and von Gersdorff, 2000). A sound presented with high amplitude to the ipsilateral and with low amplitude to the contralateral ear will lead to a high firing rate in LSO neurons as the excitation LSO neurons receive is high whilst inhibition is low (see fig. 1.2 B). If the sound level at the contralateral ear is increased, the inhibition to LSO neurons increases and the firing rate will subsequently decrease (Tsuchitani and Boudreau, 1966; Moore and Caspary, 1983). Each LSO neuron shows a characteristic IID function tuned to a best frequency. Sound source information in the LSO is represented by a population code (Park et al., 2004).

1.2.2 ITD processing in the neural circuit of the MSO

ITD coding takes place in the neural circuit of the MSO (see fig. 1.3 A). MSO neurons receive excitatory and inhibitory inputs from both ears (see fig. 1.3 A). Spherical bushy cells of both AVCN project to the MSO neurons (Stotler, 1953;

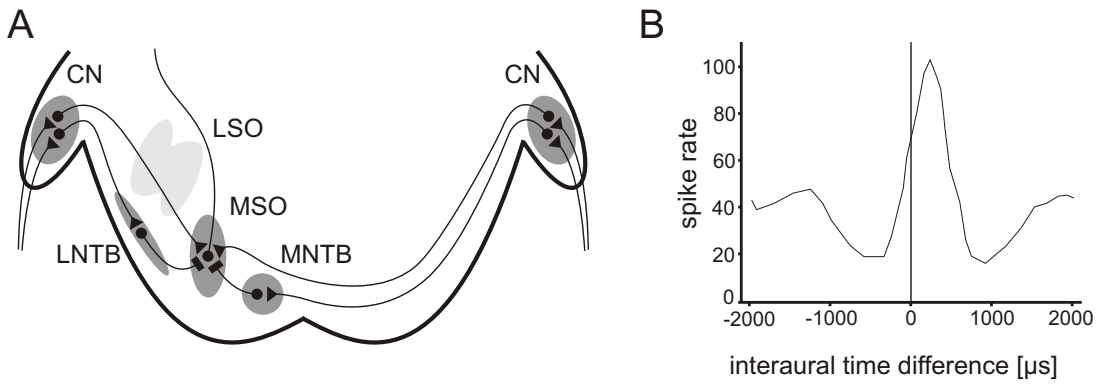

Figure 1.3: Interaural time differences (ITDs) A In mammals ITDs are computed in the medial Superior Olive (MSO). MSO neurons receive excitatory inputs from both cochlear nuclei. Importantly, MSO neurons also receive inhibitory inputs from both CN via the MNTB (contralateral inputs) and the LNTB (ipsilateral inputs, modified from Couchman, 2011). **B** This example ITD-function shows that the peak firing rate is shifted from 0. ITDs are therefore encoded on the slope of the ITD function to provide the greatest dynamic firing range. Sound source information in the MSO is represented as a population code.

Smith et al., 1993). Inhibitory projections are provided by globular bushy cells of the ipsilateral ventral cochlear nucleus via the ipsilateral lateral nucleus of the trapezoid body (LNTB) and by globular bushy cells of the contralateral ventral cochlear nucleus via the ipsilateral MNTB (Clark, 1969; Kuwabara et al., 1991; Cant and Hyson, 1992; Grothe and Sanes, 1993; Kapfer et al., 2002). MSO neurons function as fast and precise coincidence detectors (Goldberg and Brown, 1969; Yin et al., 1990; Brand et al., 2002). Two mechanisms of ITD processing are still debated. In 1948 L. A. Jeffress postulated that binaural inputs, phase locked to a certain phase of a sound wave, are integrated by a population of coincidence detector neurons. The diverging distance from both ears is equalized by axonal delay lines and ITDs are presented in a topographic place code by maximally firing neurons (Jeffress, 1948; Carr and Konishi, 1990; Reyes et al., 1996). Although this mechanism could be demonstrated in the avian auditory system (Parks and Rubel, 1975; Carr and Konishi, 1990; Overholt et al., 1992; Joseph and Hyson, 1993), strong evidence suggests that in mammals ITDs are processed in a different

way (for review: Grothe, 2003; McAlpine and Grothe, 2003; Grothe et al., 2010). It seems that in mammals, additionally to the integration of binaural excitatory inputs, the integration of phase locked (and therefore fast and precise) inhibitory inputs from both ears is of major importance to ITD coding (Brand et al., 2002; Pecka et al., 2008). The contralateral glycinergic inhibition is thought to precede the contralateral excitation at the MSO neurons. This scenario would result in a delayed net postsynaptic potential (PSP) evoked by contralateral stimulation. Additionally, the ipsilateral inhibition is thought to arrive at the MSO neuron with a slight delay when compared to the ipsilateral excitation. This induces a shortened net PSP to the ipsilateral stimulus. Both effects would shift the maximum firing of ITD functions to more positive ITDs (Grothe, 2003). This mechanism would explain the inhibition-mediated shift in ITD functions reported in mammals (Fitzpatrick et al., 2000; McAlpine et al., 2001; Brand et al., 2002), which results in MSO neuron peak firing rates at ITDs outside the physiologically relevant range of ITDs (see fig. 1.3 B), thereby contradicting the Jeffress model. Unlike the place code presentation predicted in the Jeffress model, which was shown to be the mechanism in avian sound processing, it seems that in mammals ITDs are represented by a population code similar to IIDs (McAlpine and Grothe, 2003).

In general IID and ITD processing relay on the fast and precise transmission of APs along the ascending auditory pathway, thereby preserving exactly the timing information of the auditory stimulus. Furthermore, in mammals, fast and temporally precise glycinergic inhibition is of major importance for the processing of sound localisation cues. Several structural specialisations in the auditory pathway contribute to the preservation of this timing information. The massive release sites of the inner hair cells' ribbon synapses and their release properties ensure a reliable and fast signal transfer (Moser and Beutner, 2000; Khimich et al., 2005). Pre-

and postsynaptic modulations at the endbulb of Held in the AVCN are capable of further sharpening the temporal precision of the transferred signal (Chanda and Xu-Friedman, 2010). The large calyx of Held synapses in the MNTB, together with the ion channel composition of the MNTB principal neurons, ensure a fast and reliable translation of excitation to glycinergic inhibition (Brew and Forsythe, 1995; Schneggenburger et al., 1999; Taschenberger and von Gersdorff, 2000) which is crucial for IID and ITD processing.

In contrast to these adaptations for fast and precise signal transfer in the ascending auditory pathway, a longer lasting inhibition is introduced at the level of the dorsal nucleus of the lateral lemniscus (DNLL). This GABAergic inhibition acts on a significantly longer timescale compared to the fast glycinergic inhibition in the SOC.

1.3 The neural circuit of the dorsal nucleus of the lateral lemniscus

The DNLL is located ventrally to the inferior colliculus (IC) and dorsally to the SOC (see fig. 1.4 A). It receives excitatory inputs from the ipsilateral (and to some minor extent from the contralateral) MSO and the contralateral LSO (Adams, 1979; Glendenning et al., 1981; Shneiderman et al., 1988). Glycinergic inputs are provided from the ipsilateral LSO (Brunso-Bechtold et al., 1981; Glendenning et al., 1981). The DNLL itself projects to its contralateral counterpart via the commissure of Probst and to both IC (Adams, 1979; Glendenning et al., 1981; Shneiderman et al., 1988; Kelly et al., 2009). The DNLL's projections are almost exclusively GABAergic (Adams and Mugnaini, 1984; Moore and Moore, 1987; Marie et al., 1997).

Due to their inputs, DNLL neurons are sensitive to both IIDs and ITDs (Brugge et al., 1970; Markovitz and Pollak, 1994; Kelly et al., 1998; Fitzpatrick and Kuwada, 2001; Kuwada et al., 2006). As DNLL neurons faithfully reflect the binaural prop-

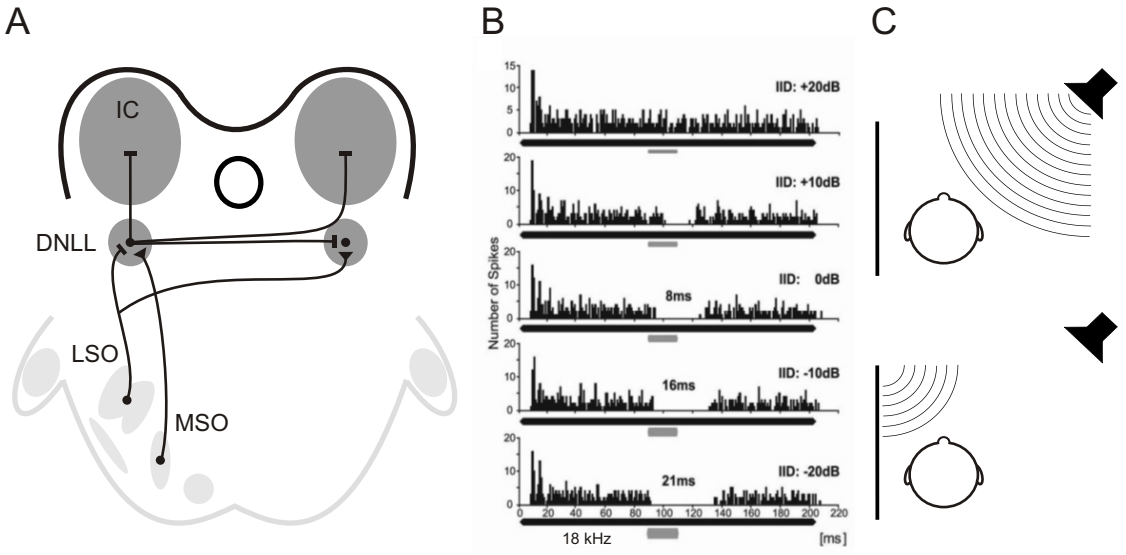

Figure 1.4: Sound localisation in a reverberant environment. **A** The neural circuit of the DNLL contributes to sound localisation in reverberant environments. It receives inputs from both SOCs and provides GABAergic inhibition to the contralateral DNLL and both ICs **B** When a DNLL neuron is excited by a sound stimulus to the contralateral ear (black bar) a second, shorter sound stimulus presented to the ipsilateral ear (gray bar) can inhibit this activity. Depending on the amplitude of the second stimulus inhibition can outlast the triggering stimulus by tens of milliseconds (data from Pecka et al., 2007). **C** In reverberant environments the listener perceives first the sound stimulus and afterwards the echoes mirrored by walls and other acoustic obstacles. The persistent inhibition generated in the DNLL is thought to suppress the further processing of the localisation cues of lagging sounds.

erties of their LSO and MSO inputs (Seidl and Grothe, 2005; Kuwada et al., 2006) they can be used as an easy accessible read-out for the activity of the SOC (Siveke et al., 2006, 2007). The best frequency distribution of DNLL neurons mirrors the entire audiogram of the animal. Animals well adapted to low frequency hearing possess a high number of ITD sensitive DNLL neurons, which can be driven by excitatory inputs from both ears (EE neurons; Kuwada et al., 2006; Siveke et al., 2007). In animals which do not hear low frequencies, IID sensitive neurons prevail in the DNLL. Those neurons are excited by one ear and inhibited by the other (EI neurons; Markovitz and Pollak, 1994; Kelly et al., 1998). The lateral crossing of excitatory LSO projections causes the excitation of IID-sensitive DNLL neurons, when presented sounds are louder at the contralateral ear. Presentation of louder

sounds to the ipsilateral ear will inhibit DNLL neurons due to the lack of excitation from the contralateral LSO and a glycinergic inhibition from the ipsilateral LSO and strong GABAergic inhibition from the contralateral DNLL (Yang and Pollak, 1994; Burger and Pollak, 2001; for review: Pollak et al., 2003).

Interestingly, *in vivo* experiments have shown that, in contrast to the glycinergic inhibition, the GABAergic inhibition of the DNLL can outlast the underlying auditory stimulus by tens of milliseconds (see fig. 1.4 B; Yang and Pollak, 1994; Kelly and Kidd, 2000; Pecka et al., 2007). This long lasting GABAergic inhibition indicates that the mode of processing in the DNLL is categorically different from the fast and precise glycinergic inhibition of the SOC. This so called persistent inhibition (PI) has been described so far in bats, rats, barn owls and gerbils (Yang and Pollak, 1994; Litovsky et al., 1999; Pecka et al., 2007).

It was suggested that PI is the cellular basis for the precedence effect or at least contributes to it. The precedence effect is a psychoacoustic phenomenon wherein directional information of echoes is suppressed although the reverberation itself is perceived (Wallach et al., 1949). When two similar sounds are presented from different directions with a delay shorter than ∼2 ms, the sound source is localised to a point in between the sources of both sounds (summing localisation). If the second sound is presented with a lag of ∼2 to ∼20-30 ms, the location of the trailing sound is not identified (localisation dominance), and if the delay exceeds the echo threshold (∼20-30 ms), both sounds are perceived and localised individually (for review: Blauert, 1997; Litovsky et al., 1999).

How can PI generated in the DNLL affect the ability to locate the source of a sound? On base of their results Burger and Pollak (2001) discussed that GABAergic inputs from the contralateral DNLL together with excitatory inputs from the contralateral CN create EI properties and thereby IID sensitivity in their IC target neurons (see fig. 1.5 A). Excitation of the opposite DNLL by a trailing sound would result in a PI of the contralateral DNLL and a release from inhibition in

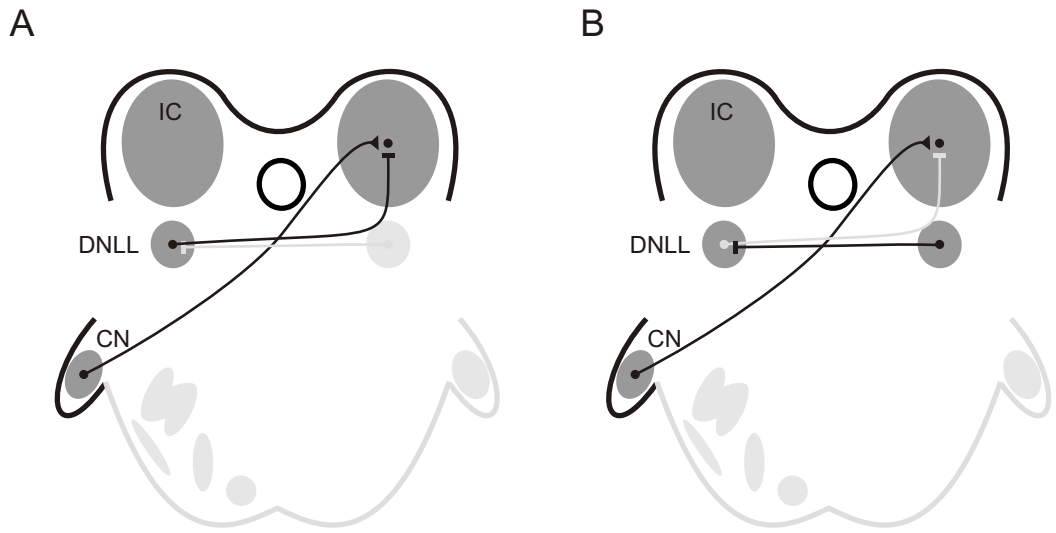

Figure 1.5: PI generated in the DNLL affects the ability of sound localisation. **A** GABAergic inhibition from the contralateral DNLL and excitatory inputs from the contralateral CN are supposed to create EI properties and thereby IID sensitivity in their IC target neurons. **B** Excitation of the opposite DNLL by a trailing sound results in a PI of the contralateral DNLL and a release from inhibition in the formerly suppressed IC neurons. During the period of PI, IC neurons respond to binaural signals to which they were unresponsive before. Burger and Pollak (2001) suggested that the release from inhibition in the EI cells would degrade the population code representation of IIDs.

the formerly suppressed IC neurons (see fig. 1.5 B). During the period of PI, IC neurons respond to binaural signals to which they were previously unresponsive. Burger and Pollak (2001) suggested that the activity in IC neurons would allow for the perception of the trailing sound but not its localisation as the release from inhibition in the EI cells would degrade the population code representation of IIDs in the IC. In this scenario, the accuracy of the IID population coding is decreased, resulting in a loss of place information. However, this hypothesis cannot explain the facultative character of the precedence effect. It has been shown that the precedence effect can break down in humans so that the trailing sound can be localized (Clifton, 1987). This would not be possible if the place information is discarded. It furthermore indicates that spatial information is selectively disregarded during processing. With this in mind, Pecka et al. (2007) hypothesized that the increased activity in a subpopulation of IC neurons does not degrade IID population coding,

but marks the lagging sound as an echo, which then is selectively ignored in higher brain centres.

Beside its importance for the processing of localisation cues of lagging sounds the DNLL network may contribute also to other tasks. A recent study by Mysore and Knudsen (2012) defined an ideal neural circuit for facultative categorization of competitive inputs, which is likely to play an important part in sensory systems. This hypothesised ideal neural network was composed of a feed forward lateral inhibition circuit, which was additionally connected through reciprocal inhibition and mirrors exactly the neural circuit of the DNLL. A previous study gives support to the assumption that the DNLL network's function is not restricted to processing tasks in "echo suppression". It was shown that the DNLL network is generally involved in the selective filtering of spurious localisation cues, which are also generated by the interference of several sound waves arriving simultaneously from spatially separated sources in noisy environments (Meffin and Grothe, 2009).

PI seems to be relevant for sound localisation in reverberant environments by suppressing the further processing of sound source information of the lagging sounds (see fig. 1.4 C; Yang and Pollak, 1998; Kelly and Kidd, 2000; Pecka et al., 2007). Although the physiological relevance of PI in the neural circuit of the DNLL is known or assumed, it is still under debate how this long lasting inhibition is generated on a cellular level. Two different mechanisms generating PI were hypothesized.

1.4 Two hypotheses to explain the generation of persistent inhibition

One of these hypothesized mechanisms, the "output based" mechanism focuses on the GABAergic output of DNLL neurons (see fig. 1.6 A). It states that similar to SOC neurons, DNLL neurons relay their inputs faithfully and that the time course of GABAergic inhibition required for PI is generated by release mechanisms

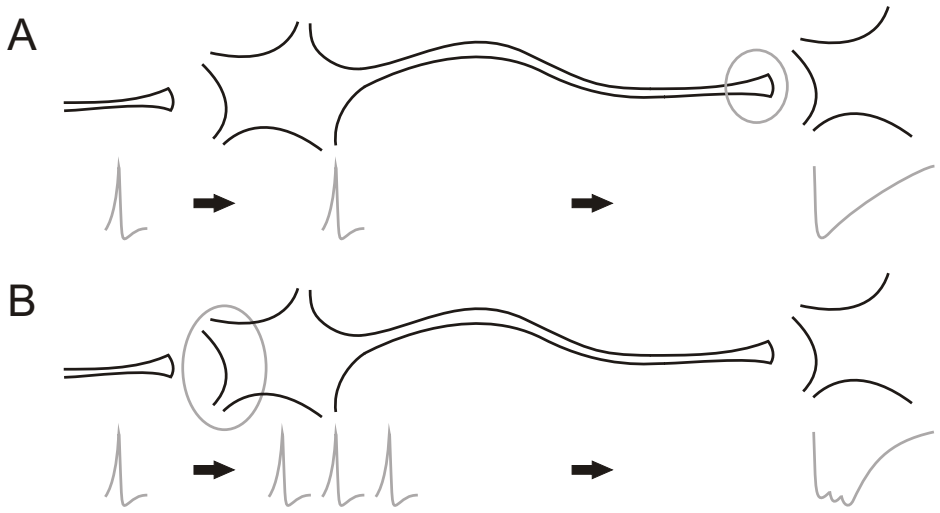

Figure 1.6: The hypothesized mechanisms to generate PI in the neural circuit of the DNLL A Excitatory inputs to the DNLL neuron are reliably integrated. Output mechanisms like asynchronous release or spillover prolong the GABAergic release and contribute to the time course of persistent inhibition (circle). **B** Excitatory inputs to the DNLL neuron are integrated and trigger an ongoing activity in the DNLL neuron. This ongoing activity will lead to a prolonged GABA release and therefore contribute to the time course of persistent inhibition. These mechanisms are not mutually exclusive (circle).

only (Wu and Kelly, 1996; Pecka et al., 2007). This could be achieved for example by strong asynchronous release or transmitter spillover. Indeed, previous *in vitro* experiments showed that the required synaptic GABAergic decay time constants for PI could be achieved by fibre stimulation in the commissure of Probst (Pecka et al., 2007), indicating that release mechanisms could be solely responsible for the long decay time constants. Further support is brought to this hypothesis by the lack of clear ongoing activity in DNLL neurons for short auditory stimuli (Covey, 1993; Bajo et al., 1998; Siveke et al., 2006; Pecka et al., 2007).

The second mechanism, the "integration based" mechanism, argues that the integration of excitatory inputs contributes to the generation of PI (see fig. 1.6 B). In this scenario, a single excitatory presynaptic event is integrated into multiple APs by the DNLL neuron itself. This would lead to an integration induced temporal extension of activity in DNLL neurons and thus automatically extend the time course of the DNLL neurons' GABAergic output (Kelly and Kidd, 2000). This

second hypothesis was supported by findings of *in vivo* (Kelly and Kidd, 2000) and *in vitro* (Fu et al., 1997) studies. Importantly, these mechanisms are not mutually exclusive, but could rather contribute synergistically to the long lasting GABAergic inhibition in the DNLL.

1.5 Virus infection as a tool for neural circuit analysis

The structure of the neural network of the DNLL is well defined and investigated. Both the excitatory inputs to and the GABAergic outputs from the DNLL are well segregated from those of other circuits (Adams, 1979; Glendenning et al., 1981; Moore and Caspary, 1983; Kelly et al., 2009). The DNLL network is therefore a suitable subject for neural circuit analysis using methods such as electrophysiological recordings in combination with fibre stimulation, calcium imaging and pharmacological block of conductances. This is in contrast to circuits such as the IC, where a less homogenous structure combined with highly divergent input and output patterns (for review: Pollak et al., 2003) makes the use of such methods less exact.

To circumvent these difficulties, genetic strategies in neural circuit analysis are widely used. Knock-out mice are created to investigate the influence of single proteins on the function and development of neural circuits (Matsumoto et al., 2011; Hirtz et al., 2011). Recently, genetic approaches were applied to visually distinguish connected cells (Livet et al., 2007) or manipulate single neurons within a neural circuit (Boyden et al., 2005; Zhang et al., 2007; Petreanu et al., 2007; for review: Yizhar et al., 2011. Unfortunately, genetic manipulation is uncommon in gerbils, although a new strategy to establish transgenic animal lines, which does not rely on embryonic stem cells, may overcome this inconvenience in the near future (Meyer et al., 2010). Today, a combination of different methods can be used to compensate for the lack of transgenic animal lines. Electroporation or a gene gun

can be used to introduce genetic information into cells of an organism (Neumann et al., 1982; Lo et al., 1994). Conventional markers which are able to cross synapses (e.g. wheat germ agglutinin-horseradish peroxidase; for review: Ugolini, 2010) can be used to identify connected neurons in a neural circuit. However, due to the small amount of marker which is transferred from 1st to 2nd order neurons this staining method is limited by an increasing dilution effect.

An alternative and more powerful option to those strategies is the use of viral vectors (Köbbert et al., 2000; Ekstrand et al., 2008). Viral vectors are used as a vehicle to introduce genetic information into cells of interest and thereby change their genetic content (Walther and Stein, 2000; Thomas et al., 2010). To maximise the benefit of this approach in neural circuit analysis a suitable viral vector should have the following characteristics: 1. It should be able to reliably introduce the transgenic information into a high proportion of cells in different brain areas. 2. The infection should be carried to non-dividing, differentiated cells and should also be highly neurospecific. 3. The transgenic protein should be stably expressed and show proper functioning in the host cells. 4. The virus itself should not cause damage to the infected cells to prevent major changes in their functionality (Lois et al., 2001;for review: Walther and Stein, 2000; Trono, 2000; Kootstra and Verma, 2003).

In general, with a viral vector two different experimental approaches can be pursued. First, the genetic content of the whole neural circuit can be changed (see fig. 1.7 A). For such an experimental design, viruses which show transneuronal spread, like α herpesviruses or rabies viruses are used (for review: Ugolini, 2010). The viral vector induced expression of a fluorescent protein would allow for the visual identification of functionally connected neurons of a circuit. The advantage of this method is that the use of replication competent viruses circumvents the dilution problem apparent when using tracers like wheat germ agglutinin-horseradish peroxidase (see fig. 1.7 A, left; (Smith et al., 2000; Wickersham et al., 2007); for review: Ugolini,

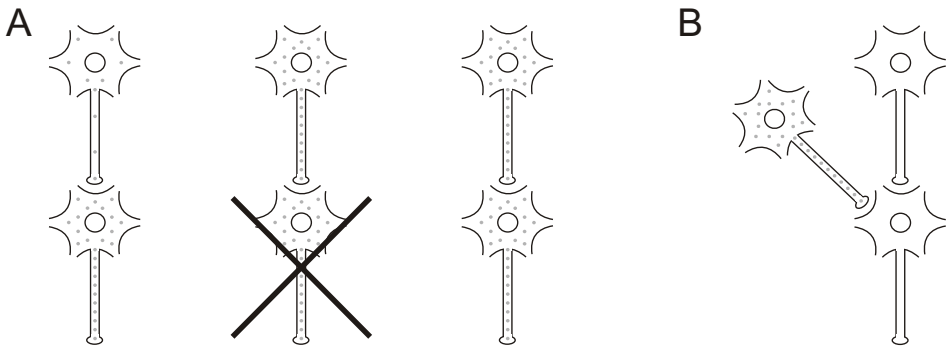

Figure 1.7: Two strategies for the use of viral vectors in neural circuit analysis A common analysis strategy is the identification of connected neurons contributing to the neural circuit. **A** Conventional markers capable of staining connected neurons (e.g. wheat germ agglutinin-horseradish peroxidase) are limited by an increasing dilution effect as only a small amount of the marker is transferred from 1st to 2nd order neurons (left). Replication competent viruses that are able to infect and stain connected neurons by expression of fluorescent protein circumvent this dilution problem as they are self-amplifying, but show usually cytotoxic effects which result in the death of infected cells (middle). A more suitable viral vector would allow the modification of the genetic content to mark and manipulate neurons (e.g. expression of GFP and ChR2) of a neural circuit without harming the neurons (right). With such a tool, connected neurons could be detected and further investigated (modified from Ugolini, 2010). **B** If the genetic alteration (e.g. expression of ChR2 or NpHR) by the viral vector is restricted to a subpopulation of neurons, the contribution of these neurons to their respective circuits can be isolated.

2010). Aside from the expression of fluorescent protein with this vector strategy, it is possible to drive an upregulation (Cazzin et al., 2011) or knockdown (Tiscornia et al., 2003; Campeau et al., 2009) of an endogenous protein. Regrettably, the use of such viruses often leads to the degradation of infected cells due to cytotoxic effects (see fig. 1.7 A, middle). A more suitable viral vector would allow for the same genetic manipulations without causing damage to, and therefore modification of, the circuit (see fig. 1.7 A, right).

The second approach aims to alter the properties of a restricted group of neurons of a neural circuit to see how this subpopulation affects the outcome of the entire circuit (see fig. 1.7 B). An elegant approach involves the introduction of genes coding for channelrhodopsin 2 (ChR2) and halorhodopsin (NpHR), a light sensitive cation channel and ion pump, allowing the experimenter to excite and silence specific neurons by exposing them to light of defined wavelength ((Boyden et al.,

2005; Zhang et al., 2007); for review: Yizhar et al., 2011).

A restriction of virus infection to specific brain areas is achieved by stereotactic injection into the target area. Further, the use of viral vectors in combination with cell type specific promoters allows the restriction of the infection to specific neurons (Boëda et al., 2001; Nathanson et al., 2009; Jianwei et al., 2011). This would also overcome existing disadvantages of transgenic organisms where genetic alterations are often not as specific as desired. The major problem arising from this strategy to analyze neural networks is the change of the network itself by the viral vector or the transgenic protein. If the virus or the transgenic protein induces side effects like cytotoxicity (Glasgow et al., 1997) experimental approaches have to be planned with great caution. Also a lack of neurospecificity can compromise the experimental outcome (Blömer et al., 1997; Ehrengruber et al., 2003). In the following different viral vectors and their properties are introduced.

1.6 Lentivirus

Lentiviruses are retroviruses, usually derived from the human immunodeficiency virus (HIV) and are widely used as viral vectors (Naldini et al., 1996; Kootstra and Verma, 2003). The promoter defines the expression level of the transgenic protein (Naldini et al., 1996) and neurospecificity of infection (Yizhar et al., 2011). The wild type virus' tight restriction in the host range is by-passed by pseudotyping the viral construct with the vesicular stomatitis virus glycoprotein (Naldini et al., 1996; Zufferey et al., 1997). As with other retroviruses, lentiviruses introduce their genetic information into the host's genome. Thereby, stable or at least long lasting expression of the transgenic protein is accomplished (Walther and Stein, 2000; Lois et al., 2001). However, in contrast to other retroviruses lentiviruses are able to infect non-dividing cells as they can target the nucleus of the infected cells without the need of mitosis (Weinberg et al., 1991; Lewis et al., 1992; Trono, 2000; Ailles

and Naldini, 2002). Beside these advantageous properties the virus itself usually does not harm the host cells, and only minimal cytotoxic properties have been reported (Hong et al., 2007). The major drawback of this viral vector system is the possibility of insertional mutagenesis due to the random viral integration into the host cell's genome (Hacein-Bey-Abina et al., 2003; Bokhoven et al., 2009). For these reasons, lentiviruses are useful tools for the induction of long lasting expression of a transgenic protein, with the drawback of a long delay between infection and expression.

1.7 Semliki Forest virus

Semliki Forest virus (SFV) is a α-viral vector which was first isolated by Smithburn and Haddow in 1944. In nature it cycles predominantly between mosquitoes and small mammals and birds (Smithburn and Haddow, 1944; for review: Ehrengruber, 2002). In the mammalian CNS, wild-type SFV can induce apoptosis and in rodents it leads to lethal encephalitis (Griffin, 2001). It efficiently infects CNS neurons *in vitro* and *in vivo* (Schlesinger and Schlesinger, 2001; Ehrengruber et al., 2001; Olkkonen et al., 1993; Lundstrom, 1999). The (+)-stranded virus RNA has a 5'cap structure and a poly-A ending similar to mRNA (Kääriäinen et al., 1987) so that the first expression of the reporter gene is detectable after only four to six hours (Ehrengruber et al., 2001). However, strong cytotoxic effects occur rapidly, from within one to two days after infection (Lundstrom, 1999; Smerdou and Liljeström, 1999; Ehrengruber et al., 2001). *In vivo* studies in mice indicated that neurotropism and cytotoxicity of SFV infection are affected by the specific virus strain used and the age of the animal (Bradish et al., 1971; Pusztai et al., 1971; Atkins et al., 1990; Ehrengruber et al., 2001; for review: Griffin, 1998). In cell culture and organotypic slices it was even shown that the virus strains SFV A7 and SFV A7(74) infect neurons and glia cells in a temperature dependent manner (Ehrengruber et al.,

2003). At temperatures of 39 °C SFV infection was mainly restricted to glia cells, which is unfavourable for *in vivo* infection as the temperature during infection can not be controlled. This drawback might even be potentiated by the finding that neurons in contrast to oligodendrocytes, are capable of down-regulating SFV replication (Fragkoudis et al., 2009). SFV based vectors therefore allow for a short expression time after infection and promise high expression levels of the transgenic protein. Nevertheless, severe cytotoxicity in combination with a possible lack of neurospecificity may foil the application of SFV as a viral vector.

1.8 Pseudorabies virus as a transneuronal tracer

Pseudorabies virus (PRV) is a neuroinvasive DNA virus belonging to the family of α herpesviruses. Although its natural host are swine in which it causes Aujeszky's disease, PRV can infect a broad host range and was first isolated from oxen, dogs and cats (Aujeszky, 1902; Field and Hill, 1974; Kimman et al., 1991; for review: Pomeranz et al., 2005). In fact, PRV is able to infect most mammals aside from higher primates (Enquist, 1999; Pomeranz et al., 2005). Whereas in swine the clinical signs are latent, in other hosts the symptoms include rabies-like-symptoms, ataxia and severe pruritus which can lead to frantic self-mutilation. Therefore the induced disease is also called pseudorabies or "mad itch" (Shope, 1932; Yang et al., 1999; for review: Pomeranz et al., 2005). The clinical signs are suggested to mirror the abnormal inflammatory induced activity of PRV infected neurons (Shope, 1932; Dolivo et al., 1978; Liao et al., 1991; McCarthy et al., 2009).

PRV is pantropic and can infect a wide range of neural and non-neural cells (Card et al., 1990; Seiler et al., 2005). Wild type PRV spreads antero- and retrogradely between cells (Brittle et al., 2004). Once introduced into a neural circuit it spreads between functionally connected neurons (Card et al., 1993; Rinaman et al., 1993, 2000), but not intraaxonally to synaptically unconnected but physically adjacent

circuitry (Card et al., 1990). Restriction of PRV infection to neurons is achieved by the action of astrocytes which are susceptible to infection but not permissive to viral replication (Card et al., 1990, 1993; Rinaman et al., 1993; Tomishima and Enquist, 2002). Thereby the glia cells form a non-permissive barrier to the infected neurons and prevent spread of infection outside the functional circuitry (Card et al., 1993; Tomishima and Enquist, 2002; Seiler et al., 2005).

The mechanisms of this trans-neuronal spread and the induced morphological alterations in infected neurons are poorly understood. A recent study showed that virulent PRV strains, in contrast to avirulent strains, form fusion pores between infected neurons thereby allowing electrical coupling between connected neurons (McCarthy et al., 2009). It was suggested that these alterations are a neural base for the symptoms induced by PRV. However, the transneuronal spread turns PRV into a useful self-amplifying tool for neural tracing (Martin and Dolivo, 1983; Smith et al., 2000; for review: Ugolini, 2010).

Infection with wild type virus strains like PRV-Becker and PRV-Kaplan leads to the death of the hosts other than swine within 2-3 days (Brittle et al., 2004). The fast lethality thereby prevents an extensive infection of the neural circuit decreasing the use of wild type PRV in neural tracing. Attenuated virus strains such as PRV-Bartha induce a reduced inflammatory response to infection and the increased survival time allows for a deeper permeation of the neural circuit (Lomniczi et al., 1987; Tirabassi et al., 1997; Banfield et al., 1998; for review: Enquist, 2002). Another advantageous characteristic of PRV-Bartha is its exclusively retrograde spread (Card et al., 1990, 1998; Brittle et al., 2004; Smeraski et al., 2004). This property is caused by a deletion of three genes in the Bartha genome and facilitates further circuit analysis as the direction of viral spread is well defined (Mettenleiter et al., 1985; Petrovskis et al., 1986; Olsen et al., 2006). Although the natural course of infection happens via the peripheral nervous system PRV infection can be triggered by direct brain injection (Aston-Jones and Card, 2000). Due to virion size

(200 nm) and high affinity for extracellular matrix proteins PRV particles do not diffuse from the site of stereotactic injection so that the spread of initial infection is mainly restricted to the injection site (Card et al., 1993; for review:: Pomeranz et al., 2005.

1.9 Pseudorabies virus expressing fluorescent protein

Early PRV-Bartha tracing studies relied on subsequent immunohistochemical processing as virus infection was only revealed by antibody interactions (for review: Loewy, 1998). The development of PRV-strains expressing a fluorescent reporter protein rendered this additional procedure obsolete.

By homologous recombination, Smith et al. (2000) developed a PRV-Bartha based PRV expressing enhanced green fluorescent protein (eGFP). This new PRV virus was called PRV-152. In their study, Smith et al. showed that high expression of eGFP is achieved in PRV-152 infected neurons and that the characteristics of PRV-Bartha infection are conserved. Unlike the observed hyperexcitability in neurons infected with wild type PRV (Dolivo et al., 1978; Liao et al., 1991), electrophysiological properties of PRV-152 infected neurons seem to remain unaffected (Smith et al., 2000; Gao et al., 2009; Derbenev et al., 2010). Therefore they suggest that PRV-152 can be used to label connected neurons with eGFP and subsequently, visually identified connected neurons can be characterised electrophysiologically. Due to these properties PRV-152 is a promising potential tool for neural circuit analysis. In the following a PRV was constructed isogenic to PRV-152 but encoding a monomeric red fluorescent protein 1 (mRFP1). This construct was called PRV-614 (Banfield et al., 2003). These two different fluorescent proteins expressing PRVs suited for electrophysiological methods could be very useful for neuronal circuit analysis.

Although several *in vitro* and *in vivo* studies confirmed that the electrophysiological properties of PRV-152 infected neurons seem not to be infected (Smith et al., 2000; Davis et al., 2003; Glatzer et al., 2003; Gao et al., 2009; Derbenev et al., 2010) a recent *in vitro* study showed that PRV-152 infection induced severe changes in electrophysiological properties of infected cells 18 hours post injection (hpi; McCarthy et al., 2009).

1.10 Aim of the study

1.10.1 The integration of excitatory inputs in the DNLL network

This PhD thesis is divided into two parts. The first part focuses on the DNLL network and the mechanism generating PI. Here, we wanted to test the feasibility of the hypothesized integration based mechanism in the DNLL of Mongolian gerbils. Thus, the integration of excitatory inputs in DNLL neurons was analyzed. Briefly, the basic properties of synaptic transmission onto DNLL neurons were analysed and the strength of single excitatory inputs and the degree of convergence to DNLL neurons was determined. Of major interest for this question was the quantitative analysis of the synaptic input-output functions (IO-Fs) of DNLL neurons and how these can be modulated by single conductances. Finally, the GABAergic output of DNLL neurons was investigated to determine if modulation of the IO-Fs leads to changes in the neural output.

1.10.2 Suitable viral vectors for the use in Mongolian gerbils

In the second project we aimed to establish the application of viral vectors in neural circuit analysis in Mongolian gerbils. In the beginning the focus of the work lay on the MNTB function and its importance for the neural circuits of the

MSO and LSO. ChR2 and NpHR were to be expressed via a suitable viral vector preferably in the whole population of MNTB principal neurons. By activating and silencing the infected MNTB neurons by light exposure we wanted to gain further insight of the MNTB function modulating auditory stimulus processing in MSO and LSO. As a first step, this was attempted in brain slice patch clamp recordings with the goal to later adapt this technique for *in vivo* applications. We tested several lentiviral constructs coding for GFP, ChR2 or NpHR. The expression of the transgenic protein was driven either by CamKII or Synapsin I. Additionally, as lentiviral vectors require a relatively long expression time we also tested a Semliki Forest virus expressing ChR2 tagged with RFP. We aimed to determine if the proper function of the expressed transgenic protein was achieved, if the infection was neurospecific and how infected cells were affected by virus infection. However, although we tested several viral constructs the main focus of this study was still the physiological analysis of the MSO and LSO circuit following the preliminary work.

It soon became apparent that the task of finding a viral vector applicable in Mongolian gerbils was more difficult than expected as most viral vectors were designed and optimized for the use in other hosts. The focus of the study then became to find and characterise a suitable viral vector for the use in Mongolian gerbils. Based on the previous work by Smith et al. (2000), Gao et al. (2009), Derbenev et al. (2010) and others, who indicated that PRV-152 is a potential tool for neural circuit analysis we decided to test PRV-152 in the IC of Mongolian gerbils. The time course of infection, the infection rate and the neurospecificity of PRV-152 infection were analyzed. Due to the contradictory findings of McCarthy et al. (2009), the electrophysiological properties of PRV-152 infected cells were also of major interest.

In this thesis, the detailed characterization of PRV-152 in Mongolian gerbils appears to be more systematic compared to that involving the other potential viral vectors. This becomes especially apparent in the higher quality of immunohistochemical stainings in the PRV-152 experiments and the in some cases low number of

experimental trials in the preliminary virus work (e.g. electrophysiological recordings of ChR2 expressing cells). This reflects the early aims of this study where we focused primarily on the analysis of neural networks, and approaches using unsuitable viral vectors were swiftly discarded. Nevertheless, this preliminary data is presented here as an illustration of some of the potential pitfalls in the use of viral vectors.

2 Material and Methods

All experiments described in this thesis complied with institutional guidelines and national and regional laws.

2.1 Animals

In these experiments Mongolian gerbils (*Meriones unguiculatus*) of postnatal day (P)15-17 and P48-85 were used. Animals were raised in the institutional animal breeding facility, where they were kept on a 12 hour night-day rhythm in enriched housing. Both sexes were utilized for experiments.

2.2 Slice preparation

Animals were decapitated and brains were removed in ice cold dissection solution (in mM: 50 sucrose, 25 NaCl, 25 $NaHCO_3$, 2.5 KCl, 1.25 NaH_2PO_4, 3 $MgCl_2$, 0.1 $CaCl_2$, 25 glucose, 0.4 ascorbic acid, 3 myo-inositol and 2 Na-pyruvate; pH 7.4 when bubbled with 95% oxygen and 5% CO_2). 200 µm thick transverse brainstem slices containing DNLL (DNLL-project and virus-project) or IC (virus-project) were taken with a vibratome VT1200S (Leica, Wetzlar, Germany). Slices were subsequently incubated for 45 minutes at 36 °C in extracellular recording solution (in mM: 125 NaCl, 25 $NaHCO_3$, 2.5 KCl, 1.25 NaH_2PO_4, 3 $MgCl_2$, 0.1 $CaCl_2$, 25 glucose, 0.4 ascorbic acid, 3 myo-inositol and 2 Na-pyruvate; pH 7.4 when bubbled

with 95% oxygen and 5% CO_2)

2.3 Electrophysiology

After incubation the slices were transferred to a recording chamber and continuously perfused with extracellular solution. The experimental set-up consisted of an upright microscope (BX50WI, Olympus, Hamburg, Germany) with gradient contrast illumination (Luigs und Neumann, Ratingen, Germany). For visualisation of slices and cells a Poly-IV monochromator and a CCD camera were used (Till Photonics, Gräfelfing, Germany). To analyze the neural circuit of the DNLL electrophysiological recordings of DNLL neurons were obtained using an EPC10/2 amplifier (HEKA Elektronik, Lambrecht, Germany). All recordings were made at near physiological temperatures of 34-36 ℃.

For the characterization of virus infected cells brain slices were treated as before. Electrophysiological recordings of virus infected cells in the IC, DNLL or MNTB were obtained with the previously described set-up or under an upright microscope (BX50WI, Olympus, Hamburg, Germany) outfitted with a video camera (Till Photonics, Gräfelfing, Germany), gradient contrast illumination (Luigs und Neumann, Ratingen, Germany), a mercury lamp (X-cite 120, Lumen Dynamics, Mississauga, Canada) and an EPC10/2 amplifier (HEKA Elektronik, Göttingen, Germany). Electrophysiological recordings of infected cells were done at room temperature (RT) in current clamp-mode only. In both studies the bridge balance was adjusted to 100% when recordings were done in current-clamp mode. During voltage-clamp recordings the access resistance was compensated to a residual of 2.8 - 3 MΩ. The data was acquired at 20 kHz and filtered at 3 kHz.

Fibre stimulation of afferent fibres was used to evoke synaptic currents. For this purpose the stimulation electrode was filled with extracellular solution. For stimulation 200 µs voltage pulses were generated by an Isolated Pulse Stimulator

(Model 2100, A-M Systems, Science Products, Hofheim, Germany), which was triggered by the EPC10/2 amplifier. Between single fibre stimulation experiments there was a break of at least 7 s between stimulations to permit synaptic recovery.

Recordings of EPSCs and Ca^{2+} currents in voltage-clamp mode only were performed with the following solution (in mM): 130 Cs-gluconate, 10 Cs-HEPES, 20 tetraethylammonium chloride (TEA), 3.3 $MgCl_2$, 2 Na_2-ATP, 0.3 Na-GTP, 3 Na_2-phosphocreatine, 5 EGTA and 0.1 Alexa488 hydrazide or its 568 analogue. During experiments where both voltage- and current-clamp recordings were made in the same cell the standard current-clamp intracellular solution was used (in mM): 145 K-gluconate, 5 KCl, 10 HEPES, 2 K-ATP, 2 Mg-ATP, 0.3 Na-GTP, 10 Na_2-phosphocreatine, 5 EGTA and 0.1 Alexa488/568. When recording in virus infected cells the Alexa dye in the intracellular solution was selected for different fluorescence spectra than the expressed fluorescent protein. Intracellular solutions were adjusted to pH 7.2 with CsOH or KOH. AP generation was blocked intracellularly with QX314-bromide (5 mM, Tocris bioscience) or extracellularly with tetrodotoxin (TTX,1 µM, Alomone labs).

EPSCs were recorded at a holding potential of -60 mV. For pharmacological isolation, SR95531 hydrobromide (10 µM, Tocris bioscience) and strychnine hydrochloride (1 µM, Sigma Aldrich) were added to the extracellular solution. For the recordings of only AMPA receptor mediated EPSCs 3-(2-Carboxypiperazin-4-yl)propyl-1-phosphonic acid (CPP, 10 µM, Biotrend) or D-2-Amino-5-phosphonovalerate (D-AP5, 50 µM, Tocris bioscience) were added. In some experiments cell responses were evoked by injecting simulated EPSPs (simEPSPs) or EPSCs (simEPSCs) into the cells. Therefore previously recorded EPSPs and EPSCs were offset corrected for resting potential or leak current respectively and then scaled to different amplitudes (IGORpro, Wavematrics). The resulting simEPSPs and simEPSCs were then used as command templates for the EPC10/2 amplifier.

To isolate Ca^{2+} currents TEA (10 mM, Sigma Aldrich), 4-aminopyridine (4-AP,

2 mM, Sigma Aldrich), TTX (1 µM, Alomone), ZD7288 (50 µM, Biotrend), SR95531 hydrobromide (10 µM), strychnine (1 µM), DNQX (20 µM, Tocris, bioscience) and D-AP5 were applied extracellularly. Leak and capacitive current subtraction was carried out with a P/x protocol with corresponding -10 mV simEPSP command waveforms. Potassium currents were isolated with SR95531 hydrobromide, strychnine, TTX, DNQX and CPP. $K_{v1.1}$, $K_{v1.2}$ and $K_{v1.6}$ channels were blocked with 100 nM α-Dendrotoxin (Alomone Labs, disolved in 0.1 mg/ml cytochrome c) and $K_{v3.x}$ conductances were blocked with 0.5 mM TEA (Mathie et al., 1998). GABAergic inhibitory postsynaptic potentials (IPSPs) were isolated in the presence of strychnine, D-AP5 and DNQX.

To characterise the electrophysiology of virus infected cells current and voltage thresholds were determined by stepwise current injections (20 - 300 pA steps) of 1 ms duration, firing frequency was measured by current injections of 1000 ms duration (50-200 pA step size). Input resistance was tested by repetitive current injections of -5 pA (250 ms - 1000 ms duration, minimum 30 repetitions). No pharmacology was applied during the electrophysiological recording of those cells.

After recordings brain slices were routinely fixed in 4 % paraformaldehyde (PFA) and mounted. Dye loaded cells were then used to confirm the recording location. Due to the wash out of intracellular fluid no double staining in virus infected cells (eGFP, Alexa568) was apparent after recordings. Therefore, fluorescence images of cells were taken before patching, in on-cell mode and after the fill with Alexa568. By comparing those pictures it was confirmed that the patched cells were indeed infected with PRV-152. The data was analyzed and presented without correction for the liquid junction potential (∼15 mV).

2.4 Calcium imaging

For Ca^{2+} imaging cells were filled with fluo-4 (100 µM, invitrogen) via the recording pipette and Ca^{2+} transients were subsequently imaged with a Till-Photonics system (see 2.3). 488 nm wavelength light was used for excitation and the emission was band pass filtered between 505 and 545 nm. Images were taken with a sampling rate of 50 Hz, while the exposure time for each image was 18 ms. Ca^{2+} transients were off-line corrected for background fluorescence (ΔF). To do so, a region of interest (roi) was drawn around the soma of the recorded cells (F_1). An area of interest (aoi) of approximately the same size was placed next to the cell as a reference for background fluorescence (F_0). To prevent artefacts in background correction it was important that the aoi did not overlap with the Fluo-4 loaded neuron. ΔF was then calculated by subtracting F_0 from F_1. The calculated ΔF values were then normalized to the average intensity, which was estimated from the five images immediately preceding the current injection that triggered the Ca^{2+} influx. The normalized values are expressed as change in percentage.

2.5 Viral constructs

All viral constructs used in this study were constructed and harvested at other laboratories and then transported to our laboratory.

2.5.1 Lentivirus

Lentiviral expression systems are derived from retroviruses (e.g. HIV or SIV) that induce stable expression of the reporter gene and infect also non-dividing cells. Four different lentiviral vectors were used in this study. The expression of one lentiviral vector coding for ChR2 tagged with eGFP was under the control of the CamKII-α promoter. The mammalian codon-optimized plasmid for this lentivirus, FCK(1.3)-

ChR2-GFP-W (Boyden et al., 2005) was given to us by Dr. Edward Boyden (Stanford University, California, USA). The produced and harvested lentiviruses (CamKII-ChR2) were then kindly provided by the laboratory of Dr. Magdalena Götz (Helmholtzzentrum München, Germany).

In the other lentiviral vectors expression of the reporter genes was under the control of the rat synapsin I promoter (Dittgen et al., 2004). These lentiviruses coded for eGFP (SynGFP), ChR2 tagged with GFP (SynChR2) and NpHR tagged with eGFP (SynNpHR). The SynChR2 construct was obtained by digesting the previously used FCK(1.3)-ChR2-GFP-W lentiviral plasmid. The sequence coding for ChR2 fused with GFP was ligated to the rat synapsin I promoter and introduced into the backbone of the lentiviral LV-CMV-GFP plasmid (Mistrík et al., 2005; CMV-GFP sequence was cut out before ligation). SynNpHR was produced on the base of the FCK(1.3)-Halo-GFP-W (Zhang et al., 2007; Addgene Plasmid 14750). The Halorhodopsin-eGFP sequence was cut out and then treated as the ChR2-GFP coding sequence. To obtain SynGFP the CMV promoter of the LV-CMV-GFP lentiviral plasmid was substituted by synapsin I promoter. The lentiviruses SynGFP, SynChR2 and SynNpHR were produced and harvested as described by Pfeifer et al. (2001). The molecular work was carried out by Otto Albrecht under the supervision of Dr. Stylianos Michalakis in the laboratory of Dr. Biel (Ludwig-Maximilians-Universität, München, Germany). Dr. Michalakis also kindly provided the harvested lentiviruses.

2.5.2 Semliki Forest virus

Semliki Forest virus is an α-virus that is used as viral vector for its short expression time. The Semliki Forest virus expressing ChR2-RFP was produced using a protocol similar to that in Stein et al. (2003). A ChR2-RFP construct was cloned into the pSCA1 plasmid (DiCiommo and Bremner, 1998) and the resulting pSCA1-ChR2-

RFP plasmid and pHelper (1:1 molar ratio) were then transfected into human embryonic kidney 293 cells. 36-48 hours after transfection the supernatant was harvested and stored as viral stock solution at -80 ℃. Before virus injection the viral stock was activated by treatment with α-chymotrypsin for 45 minutes at RT (ratio virus : α-chymotrypsin 20:1). Subsequently α-chymotrypsin was deactivated by adding Aprotinin (1:15) and then the virus solution was aliquoted (5 µl) and stored again at -80 ℃. The viral stock solution used here was kindly provided by Dr. Valentin Stein (MPI for neurobiology, Martinsried, Germany).

2.5.3 Pseudorabies virus-152

PRV is an α-Herpesvirus that infects functionally connected neurons. Due to the high neurospecificity of the PRV induced infection this virus is widely used in neuroanatomical tracing studies. The eGFP expressing PRV strain (PRV-152) was produced as described in Smith et al. (2000). A plasmid containing the cytomegalovirus immediate early promoter (CMV), an eGFP expressing cassette and a simian virus 40 poly-A signal was digested and, for homologous recombination, co-transfected with purified PRV-Bartha DNA into the pig kidney cell line 15 (PK-15). The harvested virus was plated on PK-15 cells and plaques were analyzed for eGFP expression by fluorescence microscopy. Virus from eGFP-expressing plaques was isolated and re-plated again on PK-15 cells. This purification step was repeated 3 times, then isolated virus was frozen as crude virus stocks at -80 ℃. Crude virus stocks were kindly provided to us by Dr. Lynn Enquist (Princeton University, NJ, USA). Before experiments the crude stocks were thawed in a water bath (37 ℃) and sonicated to disperse aggregated virus particles. The vial with the stock solution was centrifuged (5 minutes, 2000 g, RT) and the supernatant was pipetted off and aliquoted (50 µl). Aliquots were frozen at -80 ℃. Virus concentration in the used aliquots was about $2x10^8$ pfu/ml.

2.6 Stereotactic injection

For anaesthesia a mixture of Medetomidin/Midazolam/Fentanyl (MMF) was used. Concentration of anaesthetics was as follows: Medetomidin (150 ng/kg, Domitor, Pfizer Inc.), Midazolam (7.5 mg/kg, Midazolam-ratiopharm, Ratiopharm GmbH) and Fentanyl (30 ng/kg, Fentanyl-Janssen, Janssen Pharmaceutica). After the initiation of anaesthesia, Meloxicam (10 mg/kg Metacam, Boehringer-Ingelheim Pharma), as additional analgetic, and ringer solution (1 ml, Ringer Infusionslösung, B.Braun Melsungen AG) were administered subcutaneously.

Fur was sheared from the top of the animal's head and the skin was desinfected with 70 % ethanol. To remove the scalp a 2 cm long incision was made along the midline. A threaded rod (⌀2 mm) was screwed into a nut (outside ⌀3.2 mm), which then was fixed on the skull rostral to bregma with two component dental cement (Harvard Cement, Harvard Dental International GmbH). The threaded rod was afterwards used to fix the animal in a custom-made stereotactic device (Schuller et al., 1986). After the animal's position was adjusted a craniotomy (⌀2 mm) was drilled and the *dura mater* was removed. A glass pipette attached to a Nanoinjector (World Precision Instruments Inc.) was tip filled with 1 µl viral solution and inserted into the brain. 40-500 nl of the virus solution was then injected step wise (step size of 9.2 nl). There was a 15 s pause between each injection step. The glass pipette was retracted slowly 1 minute after the last injection step. In P15-17 animals the craniotomy was placed 1.75 mm lateral from λ when virus was injected into the IC. The injection pipette was introduced with a rostral tilt of 20 °. The injection pipette was inserted 3.8 mm (relative to λ) deep into the brain. If virus injected animals were used in patch-clamp experiments a second dose of virus solution was administered at 3.65 mm. For injection into the MNTB the craniotomy was located 1.05 mm right and 0.95 mm rostral to λ. The angle of the Nanoinjector was reduced to 12 ° with an additional lateral angle of 3 °. In adult animals (P55-85) only virus

injections into the IC and DNLL were performed. In these experiments the injection location was controlled by cellular responses to auditory stimuli.

After virus injection the threaded rod was removed and the skin was sutured (USP 4/0, m1.5, 45 cm, Suprama Feuerstein GmbH). An additional dose of ringer solution was administered and the anaesthesia was antagonized with Atipamezol/Flumazenil/Naloxon (AFN). Anaesthesia antagonists were used as follows: Atipamezol (0.4 µg/kg, Antisedan, Orion Pharma), Flumazenil (0.4 µg/kg, Anexate, Roche Pharma AG) and Naloxon (0.5 µg/kg, Naloxon-hameln, Hameln Pharma Plus GmbH). For pain management Meloxicam was injected every 24 hours for up to 5 days.

2.7 Transcardial perfusion

Animals were anaesthetized with a lethal dose of sodium pentobarbital (Sigma-Aldrich). Independet of body weight 10 mg sodium pentobarbital (LD_{50} in mice: 0.14 mg/g) were administered intraperitoneally (Gruber et al., 1944). Deep anaesthesia was confirmed by the toe pinch reflex. When the animal did no longer react to the toe pinch a transverse incision right below the sternum was made. The diaphragm was cut open and the ventral thorax with ribs and sternum was removed by two lateral transsections. An injection needle connected to a peristaltic pump was introduced to the left ventricle and the right atrium was opened. First, the animals were perfused for about 5 minutes (P15-17, 2 ml/minute) or 10 minutes (P55-85, 3.5 ml/minute) with PBS containing 0.1 % heparin-sodium (B.Braun Meslungen AG). The perfusion was then switched to 4 % PFA, (25 minutes for juvenile, 35 minutes for adult animals). Brains were removed, post-fixed in 4 % PFA overnight and then washed twice in PBS. If not stated otherwise brains were embedded in 4 % agarose and transverse brain sections (40-60 µm) were taken with a vibratome VT1000S (Leica, Wetzlar, Germany). When no immunohistochemi-

cal staining was done slices were directly mounted in Vectashield medium (H-100, Vector Laboratories Inc., AXXORA, Lörach, Germany).

2.8 Immunohistochemistry

Immunohistochemical staining was performed on free floating slices. Virus infected brain slices were washed in PBS containing 2 % TritonX100 and 0.1 % Saponin (washing solution, at RT). For blocking unspecific antibody interactions slices were then treated at RT with washing solution containing an additional 1 % BSA. Primary antibody was applied for 72 hours at 4 ℃. Lentiviral and Semliki Forest virus infected slices were left just overnight in primary antibody. Primary antibodies were MAP2 (1:1000, polyclonal anti-chicken, Neuromics, Acris Antibodies, Hildesheim, Germany) and S100β (1:2000, polyclonal anti-rabbit, Swant, Marly, Switzerland). Hereafter brain sections were washed again in washing solution (RT) and Cy3 conjugated secondary antibody was applied overnight at 4 ℃ (secondary antibodies used: Cy3 anti-chicken, 1:300, polyclonal, dianova, Hamburg, Germany and Cy3 anti-rabbgit, 1:200, polyclonal, Invitrogen, Karlsruhe, Germany). Brain slices were washed again in washing solution and PBS (RT). After immunohistochemical staining slices were mounted in Vectashield medium. Images were taken using a confocal microscope (Leica SP5 system, Leica, Wetzlar Germany) or a fluorescence microscope (AxioImager M.1, Carl Zeiss AG, Jena, Germany).

2.9 Data analysis

Electrophysiological data was analyzed in IGORpro (WaveMetrics Inc, Lake Oswego, OR, USA). Miniature EPSCs were extracted using a custom written template matching routine (Taschenberger et al., 2005; Couchman et al., 2010). Ca^{2+} imaging data was extracted from TILL Photonics software and analyzed in Excel

(Microsoft corporation, Redmond, WA, USA). Single images of stacks taken at the confocal microscope were processed with the ImageJ plug-in StackGroom (open source software). No z-shift correction was made. Stitching of images was done with the ImageJ distribution Fiji (open source software). Images were further processed in Adobe Photoshop (Adobe Systems Inc., San Jose, CA, USA). For figures only contrast and brightness were linearly adjustet. For counting cells in some rare cases non-linear alterations were applied to the image, to simplify the distinction between fluorescent and non-fluorescent cells. All alterations were performed over the entire images. Results are presented as mean ± standard error of the mean. Significance was tested using a two sided student's t-test. Significance level was set at 0.05.

Contribution to this work: DNLL

Part of the following results (3 Results: DNLL) has already been published. Figures 3.1 to 3.10 were slightly modified from Porres et al. (2011). Permission for reprint of those figures was received from the Journal of Neuroscience. The experimental concept of this work was mainly designed by F. Felmy and B. Grothe. Data aquisition and analysis were done by F. Felmy, E. M. M. Meyer and C. P. Porres. As far as possible this thesis presents only data obtained and analysed by C. P. Porres. In the following figures which were created by other authors or obtain data aquired and analysed by other authors are lined out:

Figure 3.1: 9 out of 11 neurons were recorded and analysed by E. M. M. Meyer and F. Felmy.

Figure 3.4: Data aquisition and analysis were done by F. Felmy.

Figure 3.5: Experiments and data analysis were mainly done by F. Felmy. Only experiments were simulated EPSCs were injected into patched cells were done by C. P. Porres.

Figure 3.6: Data aquisition and analysis were done by F. Felmy.

3 Results: DNLL

In this study we wanted to test the feasibility of the previously hypothesized integration based mechanism in DNLL neurons (Kelly and Kidd (2000); see section 1.4 page 18). Thus, we started by analyzing the basic properties of excitatory synaptic transmission to those neurons. Also the generation of action potentials (APs) was characterized by determining the neurons' synaptic input-output functions (IO-Fs) and it was further assessed whether single conductances as NMDAR, calcium or potassium mediated currents are able to modulate those IO-Fs in respect to the above stated hypothesis. Of special interest was the question of whether multiple APs could be generated upon a single presynaptic fibre shock. Finally, the impact of temporally extended postsynaptic activity in DNLL neurons on the cells' GABAergic output was investigated.

3.1 Basic excitatory synaptic transmission to DNLL neurons

In a first step, the basic excitatory synaptic transmission to DNLL neurons was characterized. Excitatory postsynaptic currents (EPSCs) underlie all generated excitatory postsynaptic potentials (EPSPs) and therefore AP generation. Thus, first the EPSCs in DNLL neurons were characterized. As miniature EPSCs (mEPSCs) are the quantal events underlying EPSCs, the investigation therefore began with

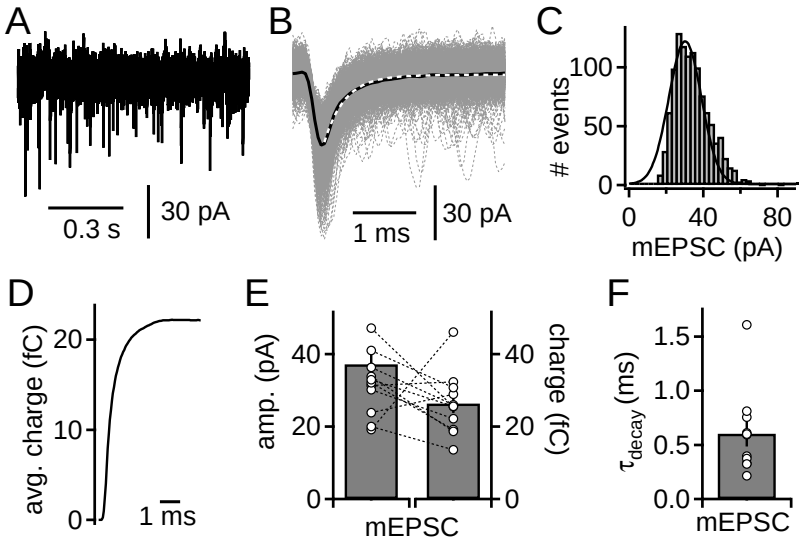

Figure 3.1: Miniature EPSC analysis in DNLL neurons, A Raw data trace with recorded mEPSCs **B** For each recorded cell (n=11) mEPSCs were extracted off-line and aligned using a threshold template matching routine. An average mEPSC (black line) was generated to determine the charge and the decay time constant (white dotted line, exponential fit). **C** Frequency histogram of the mEPSC peak amplitudes from the example recording. A gaussian fit (black line) was used to determine the mEPSC amplitude. **D** Charge of the averaged mEPSC in (B). B-D same cell as in A. **E** mEPSC amplitude and the corresponding charge of all analyzed average mEPSCs. **F** Decay time constants of the average mEPSCs. Figure modified from Porres et al., 2011.

an analysis of these currents in DNLL neurons.

3.1.1 Miniature EPSC analysis

For recordings of mEPSCs sodium and potassium channel blockers were added to the bath solution. Sodium blockers were applied to avoid recording of AP induced spontaneous EPSCs. The exogenously applied block of low-voltage activated potassium conductances is thought to enhance the occurrence of mEPSCs by depolarizing presynaptic terminals. Recordings of mEPSCs were performed at -60 mV (see fig. 3.1 A). After the recording mEPSCs were extracted by a threshold template matching routine (Taschenberger et al., 2005; Couchman et al., 2010). The isolated

mEPSCs were aligned and for each cell (n=11) an average mEPSC was calculated (see fig. 3.1 B, black line). This average mEPSC was used to determine the decay time constant (white dotted line) and the mEPSCs' charge (see fig. 3.1 D, F). The mean amplitude of the cells' average mEPSC was determined by a Gaussian fit (see fig. 3.1 C, black line) to each cell's peak amplitude frequency histogram (see fig. 3.1 C, E). Overall, the mean amplitude of the average mEPSC was 37.2 ± 3 pA. This value differed about 20 % from the mean value extracted from the generated average mEPSCs (compare see fig. 3.1 B, C) in agreement with a skewed amplitude distribution of mEPSCs. The corresponding mEPSC charge was on average 26.3 ± 2.6 fC. The average mEPSCs decay time constant was 0.60 ± 0.12 ms (figure 3.1 E,F).

3.1.2 Minimal stimulation

After the analysis of mEPSCs the next aim was to characterize the EPSCs generated in DNLL neurons by an average single excitatory fibre. This was done using electrical fibre stimulation of excitatory projections to the DNLL neurons. Excitatory currents were pharmacologically isolated. To ensure that only single excitatory fibres were stimulated, two different minimal stimulation paradigms were used.

First, the strength of the fibre stimulation was set close to threshold of inducing an EPSC. This evoked both EPSCs and failures (see fig. 3.2 A, n=13). During the second minimal stimulation paradigm the stimulation strength was increased step-wise in small voltage increments from 0 V on. In the beginning this treatment evoked no currents and then EPSCs of step-wise increasing size (see fig. 3.2 B; n=13, but 14 independent fibres). As no differences were detected between the data of both experimental paradigms, results were pooled. The average EPSC generated by a single excitatory fibre had a peak amplitude of 0.59 ± 0.07 nA and

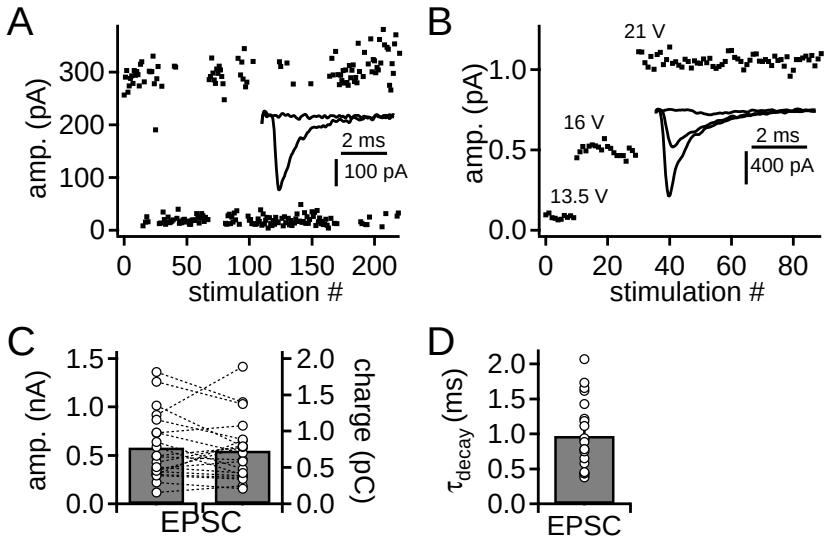

Figure 3.2: Minimal stimulation analysis of excitatory input fibres to DNLL neurons, A Minimal stimulation paradigm: strength of fibre stimulation was set close to threshold evoking failures and EPSCs (n=13). Inset shows overlaid example recordings of EPSC and failure. **B** Minimal stimulation paradigm: by increasing the stimulation strength in sub voltage increments from 0 V on, first failures and than EPSCs of step-wise increasing size were induced (n=13, but 14 independent inputs). Inset shows overlaid example recordings of different sized EPSCs and failure. **C** The minimal evoked EPSC was analyzed for average peak amplitude, the corresponding charge and (**D**) the decay time constant. Figure modified from Porres et al., 2011.

a corresponding charge of 0.73 ± 0.08 pC (see fig. 3.2 C). Decay time constants were determined by an exponetnial fit (not shown) and ranged between 0.37 ms and 2.06 ms. The mean decay time constant of EPSCs induced by the average single excitatory fibre was 0.97 ± 0.1 ms (see fig. 3.2 D).

In combination with the results of the mEPSC analysis (see fig. 3.1) the quantal content of the average single excitatory fibre can now be calculated. Dividing the average EPSC amplitude induced by a single excitatory fibre with the peak amplitude of the average mEPSC gives an estimate of the number of released vesicles. Estimated on the basis of the measured amplitudes (mEPSCs: 37.2 pA, minimal stimulation 0.59 nA), the quantal content of the average excitatory fibre was ∼16 vesicles. This calculation can also be done on the basis of the charges determined

in both experiments, mEPSC analysis and minimal stimulation (mEPSCs: 26.3 fC, minimal stimulation 0.73 pC). This led to an estimate of ∼20 released vesicles by the average single excitatory fibre. Importantly, this second calculation would reduce the potential influence of dendritic filtering on the EPSC amplitude.

3.2 The baseline membrane potential modulates the amount of synaptically evoked action potentials

So far we characterized the basic properties of synaptic transmission to DNLL neurons. The aim of the next experiment was to investigate AP generation and possible influences from postsynaptic changes. Previous work (Wu and Kelly, 1995) indicates that strong activation of excitatory DNLL inputs leads to the generation of multiple APs. Here we wanted to see how AP generation in DNLL neurons is affected by de- or hyperpolarisation of the postsynaptic membrane potential.

To investigate this question, we stimulated excitatory synaptic inputs and recorded postsynaptic responses in current-clamp mode. Stimulation strength of fibre stimulation was calibrated to reliably evoke 2 APs (in two experiments it was 3 APs) in the postsynaptic cell at rest (no current injection into the patched neuron). Then the membrane baseline potential of the postsynaptic cell was modulated by injecting a holding current (see fig. 3.3 A). During all experiments (n=9) depolarisation of the membrane potential with a positive current injection increased the number of APs generated in response to fibre stimulation (see fig. 3.3 A, B). Conversely, when hyperpolarizing the baseline membrane potential the number of evoked APs decreased (see fig. 3.3 A, B; n=9). The increase in AP number produces a temporal extension of postsynaptic activity (see fig. 3.3 C, D), which is of major interest for the DNLL circuit in general and the hypothesized integration based mechanism in particular. The duration of postsynaptic activity will now be referred to as “ac-

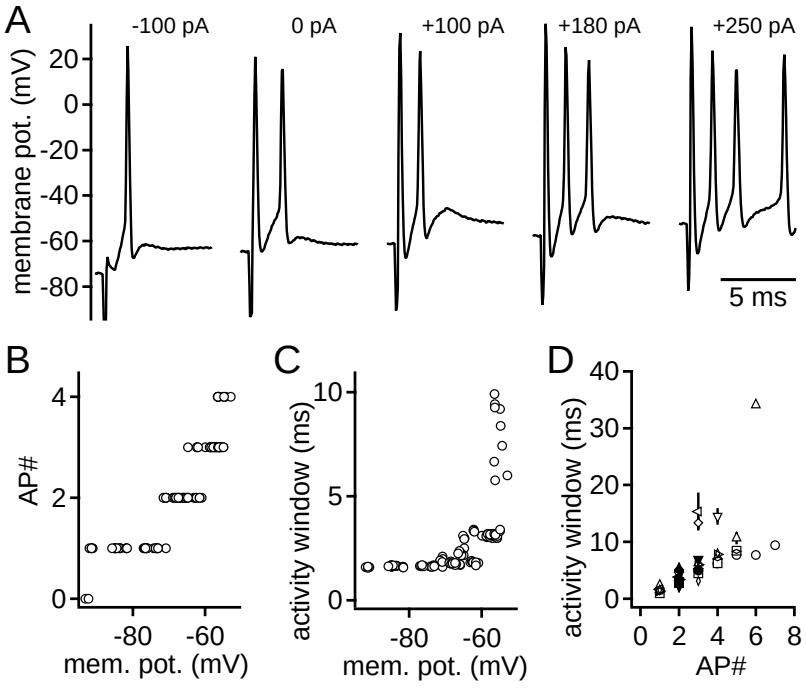

Figure 3.3: The baseline membrane potential modulates the amount of synaptically evoked action potentials, A Example recordings of synaptically evoked APs. The baseline membrane potential was modulated by the injection of holding currents ranging from -100 to 250 pA. **B** The number of synaptically evoked APs is plotted as a function of the baseline membrane potential. **C** Additional APs prolong the time window of postsynaptic activity. The postsynaptic activity window is plotted as a function of the baseline membrane potential. B and C same cell as in A. **D** The postsynaptic activity window of all cells recorded (n=9) is plotted as a function of the number of evoked APs. Each cell is illustrated with a different symbol. Solid symbols represent trials recorded without changing the baseline membrane potential by current injections. Figure modified from Porres et al., 2011.

tivity window". It is defined as the period between the time point of stimulation and the peak of the last postsynaptically evoked AP. The activity window of the cell in figure 3.3 increased from 2 - 10 ms (see fig. 3.3 C). This membrane potential dependent extension of the activity window could be observed in all cells tested (n=9). The average activity window was 1.5 $\pm$ 0.2 ms when 1 AP was elicited and 8.2 $\pm$ 1.1 ms when 4 APs were elicited. The average change of activity window in a cell from shortest (1 AP) to longest duration of activity window (maximal AP number) was 16.9 $\pm$ 4.6 ms (see fig. 3.3 D). Hence, the membrane resting potential influences the number of evoked APs and thereby the time window of postsynaptic

activity.

3.3 Synaptically transferred charge, not postsynaptic spiking properties, determines the number of evoked action potentials

We showed that changing the baseline membrane potential of DNLL neurons during fibre stimulation experiments can modulate the number of postsynaptically evoked APs and temporally extend the postsynaptic activity. As a next step the reaction of DNLL neurons to higher synaptically transferred charges was investigated. Therefore again a fibre stimulation experiment was performed. This time the stimulation paradigm consisted of a train stimulation (10 pulses, 333 Hz). As the experimental focus was on the impact of the synaptically transferred charge, no holding currents were injected to the DNLL neurons. Due to the relatively high input resistance of DNLL neurons (Porres et al., 2011), it is possible to establish well controlled voltage-clamp conditions in DNLL neurons using a standard potassium-gluconate based current-clamp internal solution. Thus, it was possible to perform those fibre stimulation experiments in current-clamp mode to record the synaptically evoked potentials and then change in each cell to voltage-clamp conditions to record the underlying currents.

The train fibre stimulation evoked considerably different responses in DNLL neurons. In some neurons responses to the stimulation train consisted only of an onset spike, others were able to generate multiple APs (see fig. 3.4 A, B). To test whether these differences in response behaviour were due to postsynaptic spiking properties hair comb currents (1 ms, 500 Hz) were injected into the cells (see fig. 3.4 C). As each recorded neuron was able to follow those stimulations, it is likely that differences in postsynaptic cell properties are not the reason for the varying response

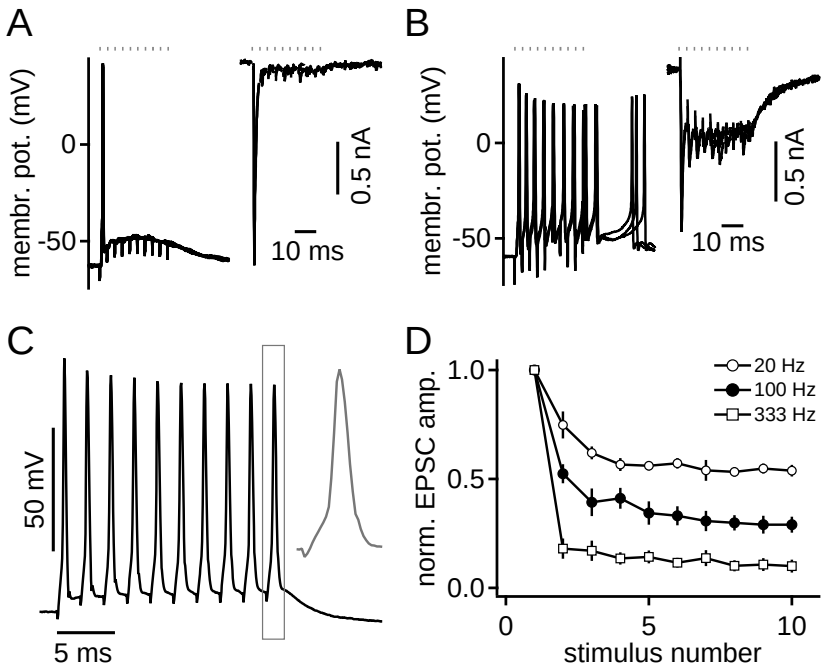

Figure 3.4: The synaptically transferred charge seems to be more important to AP generation than postsynaptic spiking properties, A and **B** Upon fibre stimulation train (10 pulses, 333 Hz) different DNLL neurons respond with a variable number of APs. In (A) the synaptic current did not evoke ongoing spiking behaviour as seen in (B). Strikingly, when multiple APs were elicited, a strong background current was also observable. Black dots above graphs indicate stimulation time points. **C** All cells recorded were able to follow hair comb current injections of 1 ms duration up to 500 Hz. Inset depicts the last AP of the train. **D** There was a marked depression of EPSC amplitudes during 10 pulse fibre stimulation trains. Figure modified from Porres et al., 2011.

behaviour. The AP number modulation due to different membrane potentials does not seem to account for this difference either, as both neurons shown in figure 3.4 displayed a similar resting potential. However, there is a striking distinction in the synaptically evoked underlying currents (see fig. 3.4 A, B; right panel). When multiple APs were elicited a strong background current built up beneath the underlying postsynaptic current (see fig. 3.4 B, right panel). In neurons that responded with an onset AP only, no such background current was detectable (see fig. 3.4 A, right panel). Irrespective of the neuron's spiking behaviour, all recorded EPSCs showed a marked depression in amplitude (see fig. 3.4 D).

From the results in figure 3.4 it is apparent that the neurons response is most

probably determined by the synaptically transferred charge. Modulation induced by changes in the membrane potential may execute additional influence on the neurons' behaviour. This outcome, in combination with the large variation in the resting membrane potential found in DNLL neurons (Porres et al., 2011; data is not shown here) led to the decision not to clamp DNLL neurons to a defined resting potential during experiments.

3.4 NMDA receptors amplify EPSP summation and the generation of action potentials

So far we have shown that the number of postsynaptically evoked APs can be modulated by a cell's baseline membrane potential (see fig. 3.3). At the same time the synaptically transferred charge seems to be of similar or even greater importance for determining the amount of postsynaptically elicited APs (see fig. 3.4). In the next experiment we wanted to focus on the synaptic charge transfer to DNLL neurons. mEPSCs (see fig. 3.1) recorded at -60 mV are mainly AMPAR mediated (Mayer et al., 1984; Nowak et al., 1984; Forsythe and Westbrook, 1988). Earlier *in vitro* studies showed that in DNLL neurons NMDA receptor (NMDAR) mediated currents are also present (Wu and Kelly, 1996; Fu et al., 1997). Furthermore, *in vivo* experiments suggested that these NMDAR mediated currents have a major impact on the DNLL network's function (Kelly and Kidd, 2000). Thus, to analyze the relationship between transferred charge and number and timing of elicited APs, we characterized the IO-Fs of DNLL neurons putting a special focus on the influence of NMDAR mediated currents.

Fibre stimulation experiments were done in both voltage- and current-clamp mode in the same cell. In both patch-clamp modes the same stimulation site was used and stimulation intensities were increased step-wise from 0 to 80 mV, evoking a step-like

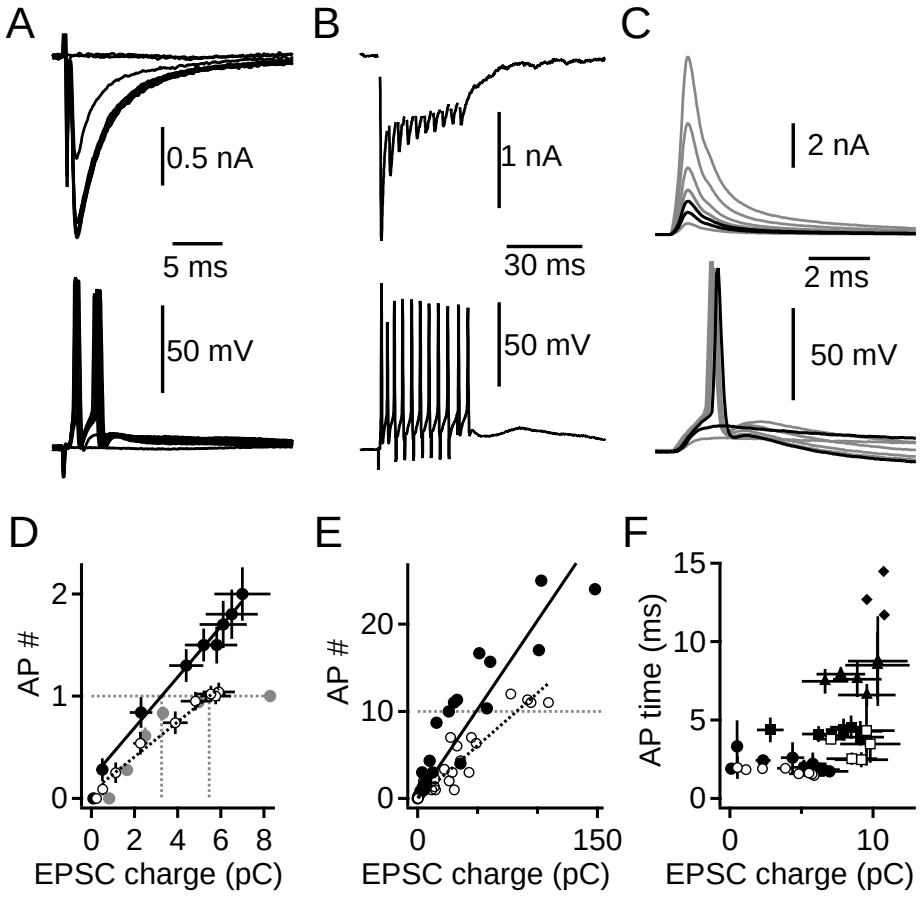

Figure 3.5: The NMDAR mediated currents enhance the synaptic IO-F of DNLL neurons, A EPSCs evoked by fibre stimulation were recorded at -60 mV (top panel). Stimulation intensities were step-wise changed between 80 and 0 V. By switching between voltage and current-clamp mode in a given cell it was possible to record also the corresponding voltage responses of the same cell (bottom panel). **B** The same experiment was repeated with a 10 pulse train stimulus at 333 HZ. Same cell as in (A). **C** Simulated EPSCs (simEPSCs, top panel) were injected in DNLL neurons as current-clamp commands. simEPSCs were previously recorded, background corrected and scaled to different amplitudes. The evoked corresponding voltage deflections are shown below. Black traces in both graphs mark sub- and supra threshold current injections. **D** Synaptic IO-Fs of recorded DNLL neurons from experiments A (solid and open circles) and C (gray circles). Solid circles display control population (n = 16), open circles (n = 19) and gray circles (n=5) show data obtained at the presence of CPP or D-AP5. Black lines (solid and dotted) represent linear regression fits. Gray dotted lines indicate the needed EPSC charge to reach AP threshold. **E** Synaptic IO-Fs determined in experiments (A) and (B). Same symbol legend as in (D). Regressions were fit with a fixed zero x-y crossing. **F** Temporal extension of AP response to a single fibre stimulation event plotted against the synaptically transferred charge. Circles represent first, squares second, triangles third and diamonds fourth evoked AP. Controls are displayed as solid symbols, open symbols represent data recorded in the presence of D-AP5. Figure modified from Porres et al., 2011.

increase in the EPSC amplitude (n=18, figure 3.5 A). In 10 recordings the increase in stimulation strength also provoked an increase in AP number (figure 3.5 A, D, solid circles). The same experiment was repeated with high frequency stimulation trains (10 pulses, 333 Hz, n=16) to evaluate if this relationship between synaptically transferred charge and the number of elicited APs also holds true for higher synaptic charges (figure 3.5 B). Similar to the single stimulus experiment the increase in stimulation strength was correlated with an increase in AP number (figures 3.5 D and E, solid circles). From this data the correlation between synaptically transferred charge and the number of elicited APs could be deduced. To elicit one AP in the postsynaptic neuron an average synaptic charge of 3.25 pC was necessary (see fig. 3.5 D, left vertical dotted line). The overall relationship between synaptically transferred charge and number of evoked APs can be assessed from the slope of the regression fit to the data points (see fig. 3.5 D, black solid line). The AP number increased at a rate of 2.4 AP per 10 pC synaptically transferred charge. If the data for the train stimulation experiment is also taken into account this relationship is changed to 2 AP per 10 pC synaptically transferred charge (see fig. 3.5 E, black solid line, regression fit is fixed to x-y crossing).

After analyzing the DNLL neurons' IO-Fs two results are notable. First, the number of postsynaptically evoked APs does indeed depend on the synaptically transferred charge. Second, and this is most important to the hypothesized integration based mechanism, DNLL neurons are capable of integrating a strong single fibre shock into several postsynaptic APs. To assess the influence of NMDAR mediated currents on the synaptic IO-Fs of DNLL neurons both experiments were repeated after the addition of a NMDAR antagonist (CPP or D-AP5). This data would allow us to determine if the observed relationship between synaptic charge and AP number is mainly mediated by AMPAR mediated currents or if NMDAR mediated currents do have a major influence on the DNLL neurons' IO-Fs.

The results of these experiments are displayed in figure 3.5 D and E (open circles, n=19). In these cells the resting membrane potential was not significantly different ($p > 0.05$) from the control group, meaning that modulatrory effects of the membrane potential can be disregarded. In only four out of 19 cells more than a single AP could be elicited (see fig. 3.5 D). The change in IO-F led to a higher synaptically transferred charge threshold for AP activation (5.45 pC, right vertical dotted line). This change is also illustrated in the shallower slope of the linear regression fit of 1.7 AP per 10 pC synaptically transferred charge (see fig. 3.5 D, black dotted line). A similar result is seen for the 10 pulse train stimulation experiment (333 Hz). When NMDARs were blocked, the number of postsynaptically evoked APs barely reached 10 (see fig. 3.5 E). The overall relationship between EPSC charge and AP number decreases also when the train stimulus experiment is taken into account (1.2 AP per 10 pC synaptically transferred charge, black dotted line, fit fixed at 0 y-intercept).

To confirm the importance of NMDAR mediated currents to AP generation in DNLL neurons we stimulated neurons via the injection of simulated EPSCs (simEPSCs). These simEPSCs were created from previously recorded AMPA mediated EPSCs, which were background corrected and scaled to different amplitudes ranging from 0.5 to 8 nA (charge: 0.82 to 13.2 pC, see fig. 3.5 C, upper panel). An example for the evoked voltage responses is shown in figure 3.5 C (bottom panel). When blocking NMDAR mediated currents simEPSCs were not able to induce more than one AP, irrespective of the amount of the injected charge (see fig. 3.5 D, gray circles). Together this shows that a single AMPA mediated EPSC is capable of evoking only a single AP. However, multiple high frequency AMPAR mediated inputs might induce as many APs as stimulation pulses are applied.

So far we showed that NMDAR mediated currents are able to amplify the postsynaptic activity of DNLL neurons. For the hypothesized integration based mecha-

nism, the temporal extension of this amplified activity is of major interest. The timing of the postsynaptically generated APs was therefore analyzed (see fig. 3.5 F). The first AP occurred within 2 ms after the fibre stimulation pulse (circles). There was no significant difference in timing seen between control conditions (open circles) and neurons recorded during NMDAR block (solid circles). A second AP was elicited in 10 out of 18 control cells and in only 4 out of 19 cells recorded in the presence of D-AP5. Second APs appeared within 5 ms after the stimulation pulse (squares). No third AP was generated when NMDAR were blocked. In 7 cells under control conditions a third AP was generated, which appeared on average 8.5 ± 2.1 ms after the stimulation pulse (triangles). Fourth APs were elicited in two recorded neurons and occurred ∼13 ms after the stimulation (diamonds). This means that each additional AP can prolong postsynaptic activity by ∼3 ms, resulting in a prolonged postsynaptic activity of 10-12 ms when four APs are elicited.

In section 3.1.2 we calculated the quantal content of the average afferent excitatory fibre. With the previously determined relationship between synaptically transferred charge and number of elicited APs (see fig. 3.5), it is now possible to calculate the necessary number of activated fibres to evoke one AP. Based on the mEPSC analysis and the minimal stimulation experiments the average single excitatory fibre released ∼18 vesicles transferring a charge of 0.74 pC on a postsynaptic cell (see fig. 3.1 and 3.2). Under control conditions a charge of ∼3.25 pC was sufficient to elicit an AP (see fig. 3.5 D). This would require the simultaneous activation of 4-5 fibres terminating on a DNLL neuron to elicit one AP. These fibres would liberate 72-90 vesicles transferring a charge of 2.96 to 3.7 pC. When blocking NMDAR mediated currents the necessary amount of converging fibres to drive one postsynaptic AP increases. In this case a charge of 5.45 pC is required to elicit a single AP (see fig. 3.5 D). To reach this synaptic charge 7-8 fibres must be simultaneously active, resulting in a release of 126-144 vesicles (5.18 to 5.92 pC). This second estimate can be confirmed by the experiment using simEPSCs for stimulation (see fig. 3.5 D,

gray circles), where a similar amount of synaptically transferred charge was needed to elicit a postsynaptic AP. Based on the maximal evoked currents (see fig. 3.5 D, black solid circles) under control conditions, the minimal number of fibres converging on a single DNLL neuron can be estimated. The average maximal synaptically transferred charge was ∼7.1 pC. This would correlate with 9-10 simultaneously activated excitatory fibres (162-180 vesicles, 6.66 to 7.4 pC). It is important to note all of those estimates hold true only in the case, that no inhibitory background activity is present. Hence, *in vivo* more fibres may need to be activated to elicit APs.

3.5 NMDA dependent amplification of postsynaptic responses is still present in adult animals

So far we showed that NMDAR mediated currents in juvenile Mongolian gerbils can amplify AP generation in postsynaptic DNLL neurons and thereby prolong their activity. If this phenomenon really is of functional importance to the DNLL network as stated in the hypothesized integration based mechanism (Fu et al., 1997; Kelly and Kidd, 2000), then this effect should be also detectable in adult animals. Therefore, fibre stimulation experiments (n=9) were done in adult Mongolian gerbils (P48-60).

In five out of nine cells a single pulse fibre stimulation evoked more than one AP in the postsynaptic cell. In four of these cells the number of synaptically induced APs could be reduced by blocking the NMDAR mediated currents with CPP or D-AP5 (data not shown). As demonstrated before in juvenile animals, NMDAR mediated currents in adult animals are also capable of amplifying the postsynaptic response in DNLL neurons. A similar effect was seen when those cells were stimulated with a train fibre stimulation paradigm. A 15 pulse stimulation train was applied at

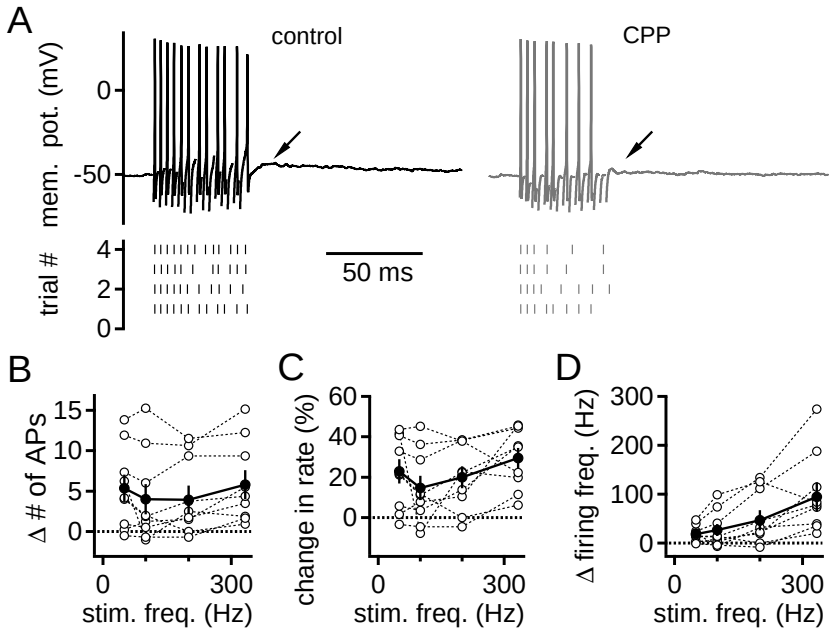

Figure 3.6: NMDAR mediated currents also enhance the synaptic IO-Fs of DNLL neurons in adult animals, A Train fibre stimulation paradigm (15 pulses, 333 Hz) applied to a DNLL neuron of an adult Mongolian gerbil. Voltage responses are depicted for control (left panel) and after the bath application of CPP (right panel). Bottom panels depict the timing of evoked APs in four successively recorded trials. In some cells, block of NMDARs eliminated a slow sub threshold depolarization (arrows). **B** Change in AP number between control conditions and NMDAR block plotted against stimulation frequency. **C** Change in firing frequency between control conditions and NMDAR block plotted against stimulation frequency. **D** Percent change in firing frequency plotted against stimulation frequency. Figure modified from Porres et al., 2011.

frequencies of 50, 100, 200 and 333 Hz. After at least 3 trials in control conditions NMDAR currents were blocked with D-AP5 or CPP (n=4, n=5; see fig. 3.6 A to D). During train stimulations blocking NMDARs also reduced the frequency of synaptically evoked APs (figure 3.6 A). In some cells, as in the shown example cell, a slow sub threshold depolarization was eliminated (arrows). By blocking NMDARs, on average ∼5 APs were lost (figure 3.6 B). In firing frequency this would result in a reduction of between 17.8 ± 5.6 and 94.5 ± 29.6 Hz depending on the stimulation frequency (figure 3.6 C). Thus, the loss of NMDAR mediated currents lead to a reduction in firing frequency of 20% at 100 Hz stimulation frequency and 25% at 333 Hz stimulation frequency (figure 3.6 D). Together, this demonstrates that an

NMDAR dependent amplification of synaptic inputs allows DNLL cells of mature gerbils to maintain high firing frequencies.

3.6 NMDA dependent integration effects GABAergic output in the DNLL circuitry

We could show that NMDAR mediated currents amplify postsynaptic responses in DNLL neurons of adult Mongolian gerbils. The appearance of this effect in adult animals indeed indicates that it serves a ongoing functional operation in the DNLL circuitry. However, in order to demonstrate that the hypothesized integration based mechanism is really feasible, it still has to be shown that the NMDAR mediated amplification of postsynaptic activity is indeed transformed into a longer lasting GABAergic output in DNLL neurons.

The DNLL provides GABAergic projections to its contralateral counterpart Adams and Mugnaini (1984); Kelly et al. (2009). Therefore the GABAergic output of DNLL neurons can be characterized as GABAergic input to the neurons of the contralateral DNLL using the same experimental presynaptic stimulation design as before. Fibre stimulation experiments were performed in P16 gerbils while all but syanptic GABAergic currents were blocked. GABAergic IPSPs were evoked using two different stimulation frequencies for control conditions (15 pulses at 100 and 333 Hz). To emulate the NMDAR-block induced drop in firing frequency, stimulation frequencies were reduced by the previously determined values (15 and 12 pulses at 80 and 250 Hz; see fig. 3.6).

Figure 3.7 A shows two fibre stimulation evoked summed GABAergic IPSPs. Under control conditions (15 pulses, 333 Hz, black trace) the summed IPSP decayed with a time constant of ∼41 ms. When NMDAR block was emulated by reducing fre-

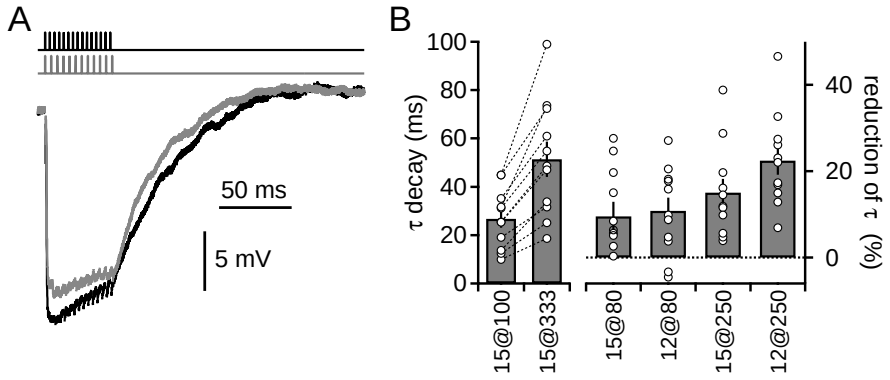

Figure 3.7: NMDA dependent integration effects GABAergic output I, A Summed GABAergic IPSPs in DNLL neurons from a P16 gerbil evoked by fibre stimulation. After recording under control conditions (black trace, 15 pulses 333 Hz) stimulation frequency was reduced (gray trace, 12 pulses 250 Hz) to emulate the block of NMDARs. Stimulation artefacts have been removed and time points of stimulation are displayed above. **B** Left graph depicts the absolute (circles) and average (bars) decay time constants of the summed GABAergic IPSPs upon fibre stimulation of 100 and 333 Hz (15 pulses, control conditions). Right graph displays the relative reduction of decay time constant of the GABAergic IPSPs when reduced stimulation frequencies were used to emulate the block of NMDAR (15 and 12 pulses at 80 Hz vs. 15 pulses at 100 Hz; 15 and 12 pulses at 250 Hz vs. 15 pulses at 333 Hz). Symbols as in left graph. Figure modified from Porres et al., 2011.

quency and pulse number of the stimulation train (12 pulses, 250 Hz, gray line) the decay time constant of the GABAergic IPSP was decreased to 36 ms. Noteworthy in this example is the similar duration of the activity window for both stimulation conditions. Differences in decay time constant are therefore conditioned by the different stimulation frequencies and pulse numbers only. The observable difference in decay time constant suggests that the NMDA dependent amplification is indeed transformed into changes in the DNLL neurons' GABAergic output. Figure 3.7 B shows the results for all stimulation frequencies tested. Under control conditions (fit. 3.7 B, left panel) GABAergic IPSPs decayed on average with a time constant 26.7 ± 3.7 ms when stimulated with 15 pulses at 100 Hz and with 51.4 ± 7.3 ms stimulated at 333 Hz (n=9). Overall, the absolute time constants ranged from a minimum of 8.7 ms at 100 Hz stimulation to a maximum of 99.03 ms at 333 Hz stimulation (open circles). In each recorded cell the higher stimulation frequency always induced a longer decay time (dotted lines link corresponding decay time constants).

The right panel of figure 3.7 B plots the relative reduction of decay time constants depending on the used stimulation frequency and pulse number. When comparing the control values obtained with the 100 Hz stimulation paradigm to the decay time constants obtained with 80 Hz stimulation of 15 pulses, an average reduction of 9.6 ± 3.4% was evident (figure 3.7 B). When additionally the pulse number was also reduced from 15 to 12 the decay time constant was further decreased (10.8 ± 3%). For higher stimulation frequencies the reduction in decay time constants was even more apparent. On average, decay time constants were reduced by 15 ± 3.2% when pulse number was maintained and only the stimulation frequency was decreased from 333 to 250 Hz. Reducing also the number of stimulation pulses lead to a further decrease in decay time constant of 22.5 ± 3.3% in total.

We could show that, at least for train fibre stimulation, the NMDAR mediated current dependent amplification of postsynaptic activity influences the time course of the DNLL neurons' GABAergic output. However, when single shock fibre stimulation evoked multiple APs it was in the range of up to 3 additional APs occurring at a frequency of ∼333 Hz (see fig. 3.5 F). Therefore we repeated the previous experiment (see fig. 3.7) with fibre stimulation of 1-5 pulses at 333 Hz (figure 3.8, n=11). Additionally, 10 and 15 pulse train stimulations were applied.

Example recordings of GABAergic IPSPs evoked by 1, 3 and 5 pulse fibre stimulation are shown in figure 3.8 A. Stimulation times are given above the recorded traces and match the corresponding elicited response in colour. In the three recordings, decay time constants increase from 13.25 ms for single shock fibre stimulation to 20.67 ms when five pulses were applied. A single stimulation pulse hyperpolarized the membrane potential from on average 62.7 ± 1.25 to 70.6 ± 0.7 mV (see fig. 3.8 B, bottom panel). Each additional stimulation pulse decreased the membrane potential further until after 4 pulses saturation is achieved at ∼ -76 mV. The membrane resting potentials of DNLL neurons kept stable during the experiments so

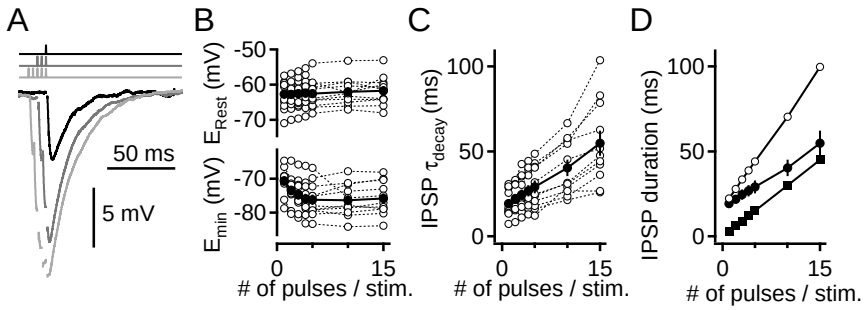

Figure 3.8: NMDA dependent integration effects GABAergic output II, A GABAergic IPSPs evoked by single pulse, three pulse and five pulse fibre stimulation (333 Hz). Time points of stimulations are displayed above. Corresponding stimulation and response match in colour. **B** Resting membrane potential (top) and minimal potential (bottom) reached during fibre stimulations (1-5, 10 and 15 pulses at 333 Hz). **C** Decay time constants of the GABAergic IPSPs (last stimulation pulse only) plotted against the stimulation pulse number. **D** Duration of the evoked GABAergic inhibition as a function of stimulation pulse number. Open circles depict the average decay time constants of IPSPs. Open squares show the duration of activity windows induced by stimulus trains (measured from Stimulus onset to last stimulation pulse). Solid circles show the sum of both IPSP components. Figure modified from Porres et al., 2011.

that alterations in decay time constants cannot be caused by fluctuations of membrane resting potential (see fig. 3.8 B, upper panel). Decay time constants of the evoked GABAergic IPSPs slow down with increasing stimulation pulse number (see fig. 3.8 C). On average the decay time constant of the GABAergic IPSPs rises from 19.17 ± 2.49 ms (1 stimulation pulse) by ∼10 ms to 29.08 ± 3.75 ms at 5 stimulation pulses (see fig. 3.8 C, black circles). At stimulations with 15 pulses decay time constant is increased to 54.73 ± 7.45 ms. The stimulation pulse dependent increase in decay time constant appears to be nearly linear. This data shows that additional stimulation pulses lead to a larger hyperpolarisation and a longer decay time constant of the summed GABAergic IPSPs. Thus, also for single and few stimulation pulses, the NMDA dependent amplification of postsynaptic activity in DNLL neurons provokes a prolongation of the neurons' GABAergic output.

The entire time course of inhibition induced by a summed GABAergic IPSP in the DNLL consists not only of the decay time constant but also of the time window between first stimulation pulse and the onset of repolarisation. Therefore, this

time window must be added to the decay time constant to illustrate the entire inhibitory time span (see fig. 3.8 D). At a stimulation frequency of 333 Hz the time window before the decay onset ranges from ∼3 ms at 1 stimulation pulse to ∼45 ms at 15 stimulation pulses (black squares). The average decay time constant was determined before (see fig. 3.8 C) and rises from 19.17 ± 2.49 ms (1 stimulation pulse) to 54.73 ± 7.45 ms (15 stimulation pulses, black circles). Added together this leads to an inhibitory time course of ∼22 ms for single pulse stimulation and ∼100 ms for 15 pulse stimulation (open circles).

This illustrates that each stimulation pulse and therefore each AP generated in a DNLL neuron prolongs the neuron's GABAergic output in two ways: first, it prolongs the activity window between first stimulation pulse and decay time onset. Second, it extends the decay time constant itself. This shows that the NMDAR mediated current dependent amplification of postsynaptic activity in DNLL neurons indeed influences the time course of the DNLL neurons' GABAergic inhibition.

3.7 Calcium currents do not effect EPSP summation

So far we showed that NMDAR mediated currents amplify postsynaptic AP generation in DNLL neurons and thereby prolong their GABAergic output. It was reported that NMDAR currents mediate this amplification of postsynaptic activity by enhancing the spatial summation of excitatory inputs to DNLL neurons (Porres et al., 2011; data not shown here). This conclusion was drawn from the finding that NMDAR mediated currents counteract the voltage-dependent speeding of the EPSPs. It would be interesting, if other conductances than NMDAR mediated currents also effect EPSP summation and therefore influence AP generation. Promising candidates for such an effect on EPSP summation would be sodium, calcium and potassium currents. Sodium and calcium conductances would be expected to

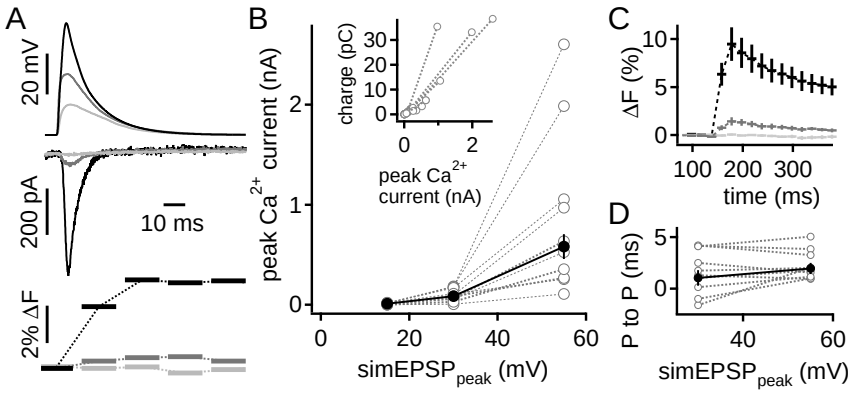

Figure 3.9: Ca^{2+} currents do not enhance spatial EPSP amplification I, A EPSP-like waveforms (simEPSP, top) were injected into DNLL neurons to evoke pharmacologically isolated and P/x corrected Ca^{2+} currents (middle). Additionally, fluo-4 Ca^{2+} imaging was performed (bottom) to confirm that elicited currents were Ca^{2+} mediated. **B** Peak amplitude of Ca^{2+} current plotted against the size of the injected simEPSP. Inset shows charge of elicited Ca^{2+} currents as a function of their corresponding peak amplitude. **C** Average increase in fluorescence evoked by simEPSPs of 55 mV (black), 30 mV (gray) and 15 mV (light gray) amplitude. **D** Latency between peak amplitude of Ca^{2+} current and the underlying simEPSP (P to P). Graph depicts only data for simEPSPs of 30 and 55 mV amplitude. Figure modified from Porres et al., 2011.

increase EPSP amplitude and half width and thereby enhance EPSP summation. Potassium currents in contrast would rather counteract EPSP summation by decreasing EPSP amplitude and half width. As sodium channels are directly involved in AP and EPSP generation and therefore cannot be unambiguously dissected, we first aimed to determine the potential contribution of Ca^{2+} channels in shaping the EPSP.

To investigate if Ca^{2+} currents contribute to the shape of the EPSP, Ca^{2+} conductances had to be blocked to compare the resulting EPSPs with the EPSPs recorded under control conditions. As a result of the block of Ca^{2+} channels, fibre stimulation could not be used to evoke the EPSPs. We therefore decided to use simEPSCs (see fig. 3.5 C) to elicit EPSP-like voltage deflections. However, prior to this, it had to be verified that Ca^{2+} currents in DNLL neurons could be elicited with simulated voltage commands.

Therefore, previously recorded EPSPs were background corrected and then injected as simulated EPSPs (simEPSPs) from a holding potential of -60 mV (n=9, see fig. 3.9 A). For the generation of simEPSPs EPSPs were selected for amplitudes (15, 30, 55 mV) and corresponding half widths, that fitted the reported voltage-dependent speeding of EPSPs (Porres et al., 2011; data not shown here). For later off-line analysis (P/x protocols) these simEPSPs were inverted and scaled to an amplitude of -10 mV. For additionally monitoring the Ca^{2+} influx, neurons were loaded with fluo-4 via the recording pipette (see fig. 3.9 A). The smallest simEPSPs, depolarizing the cell to a membrane potential of -45 mV, did not elicit a detectable Ca^{2+} influx (figure 3.9 B, C). In contrast, intermediate and large simEPSPs activated Ca^{2+} conductances, which could be monitored by the fluo-4 fluorescence transient (figure 3.9 B, C). The size of induced Ca^{2+} currents was correlated with the amplitude of the underlying simEPSPs (see fig. 3.9 B). The increase in the Ca^{2+} currents' amplitude was also mirrored by the increase in fluorescence (see fig. 3.9 C), indicating a close relationship between Ca^{2+} current amplitude and charge (see fig. 3.9 B, inset). The latencies between peaks of Ca^{2+} currents and underlying simEPSPs (1.03 $\pm$ 0.76 ms for 30 mV simEPSP and 1.96 $\pm$ 0.54 ms for 55 mV simEPSP) showed that Ca^{2+} currents are activated with a short delay. The evoked Ca^{2+} current could be blocked by the application of 0.2 mM Cd^{2+} and 1 mM Ni^{2+} (n=3, data not shown).

After it was shown that Ca^{2+} currents could be triggered by simEPSPs we reverted the experiment and used simEPSCs to evoke EPSP-like voltage deflections. SimEPSCs were scaled to amplitudes ranging from 0.5 to 8 nA (see fig. 3.10 A, for generation of simEPSCs see section 3.4, page 54). As in the previous experiment Ca^{2+} currents were monitored with fluo-4 (see fig. 3.10 A, middle and bottom inset). First EPSP-like voltage deflections induced by simEPSCs were recorded under control conditions (see fig. 3.10 A, middle). Then Ca^{2+} currents were blocked with 0.2 mM Cd^{2+} and 1 mM Ni^{2+} (see fig. 3.10 A, bottom). If Ca^{2+} currents contribute to

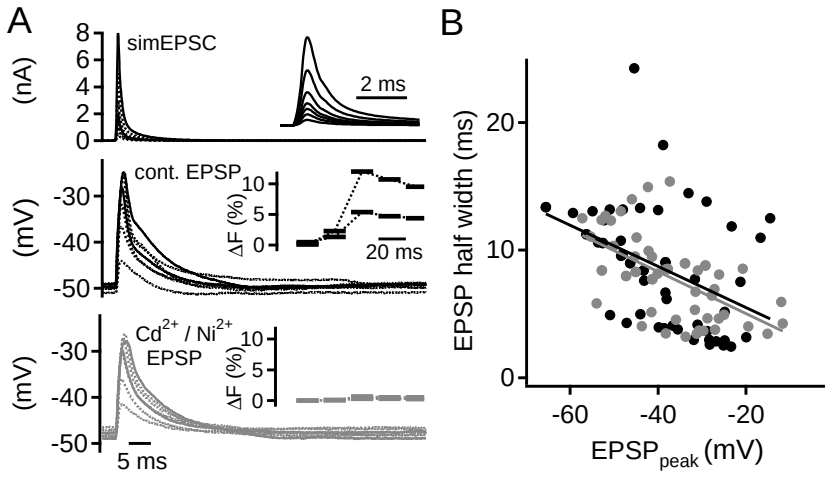

Figure 3.10: Ca^{2+} currents do not enhance spatial EPSP amplification II. A EPSC-like waveforms (simEPSCs, top) of different sizes evoked EPSP-like deflections in patched neurons. Graphs show recordings from control conditions (middle) and during blockade of Ca^{2+} channels (bottom) by Ni^{2+} and Cd^{2+}. Insets show the simEPSCs in detail (top), and the change in fluorescence (middle, bottom) corresponding to the displayed recordings **B** EPSP half width plotted against the absolute EPSP amplitude. Black circles depict data of recordings during control conditions, gray circles during the blockade of Ca^{2+} channels. Linear regression fits to both data populations match in colour. Figure modified from Porres et al., 2011.

the shape of the EPSP-like deflections, then a difference between the EPSP shapes of both data populations should be apparent. The EPSP half width was therefore plotted against the EPSP's absolute peak amplitude (see fig. 3.10 B). Control data is depicted as black circles, data recorded when Ca^{2+} conductances were blocked is represented by gray circles. Linear regression fits to both data populations match in colour. When comparing the slopes of both linear regression fits (-0.16 ms/mV for control, -0.16 ms/mV for block of Ca^{2+} currents), it becomes obvious that the relation between half width and peak amplitude of EPSP-like voltage deflection is not affected by block of Ca^{2+} conductances. This shows that Ca^{2+} currents do not interfere with the voltage-dependent speeding of EPSP-like voltage deflections.

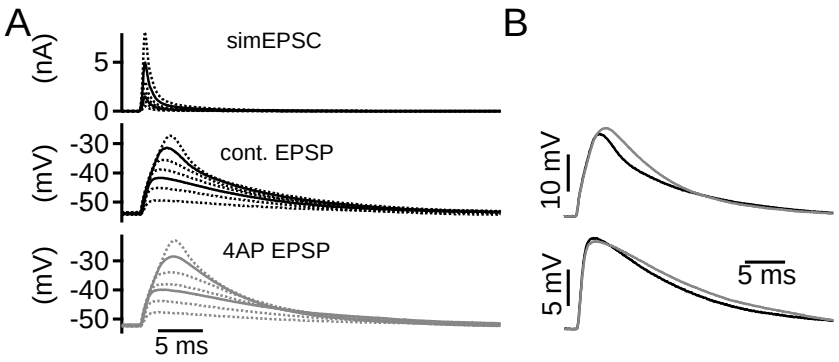

Figure 3.11: Voltage activated potassium conductances affect EPSP shaping I, A EPSC-like waveforms (top, simEPSCs) scaled to different sizes were injected to evoke EPSP-like deflections (middle) in control conditions and when voltage dependent potassium currents were blocked by 2 mM 4AP (bottom). Solid lines display EPSP-like deflections and underlying simEPSCs shown in B. **B** Magnified view of two EPSP-like voltage deflections from A (solid lines) under control conditions (black line) and in the presence of 2 mM 4AP (n=7).

3.8 Blocking voltage activated potassium channels unspecifically does affect EPSP summation

We could show that Ca^{2+} influx in DNLL neurons can be triggered by EPSCs of middle and high amplitudes but does not contribute to the EPSP shape. In the next experiment we wanted to focus on the influence of voltage activated postassium conductances and their potential contribution to EPSP shape. Therefore we repeated the previous experiment and injected simEPSCs (ranging from 0.5 to 8 nA) in patched neurons (see fig. 3.11 A, top, n=7). Potassium currents were pharmacologically isolated. The resulting EPSP-like voltage deflections were first recorded under control conditions (see fig. 3.11 A, middle). Then voltage activated potassium conductances were blocked with 2 mM 4AP (see fig. 3.11 A, bottom). If voltage activated potassium currents influence EPSP summation a difference in the deflections' shape should be apparent.

Figure 3.11 B displays two traces of the example recording (see fig. 3.11 A, solid lines) in greater detail, comparing control condition (black traces) to the block of

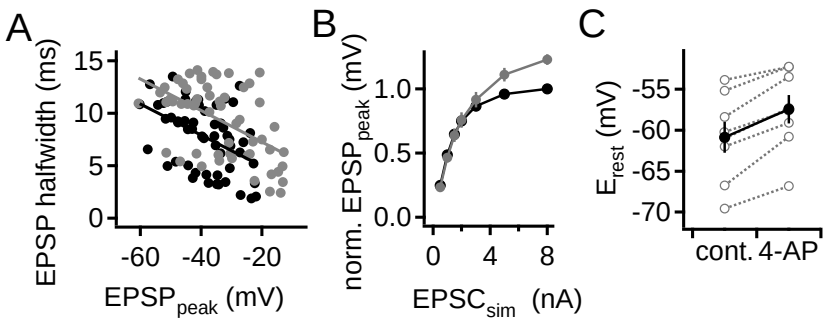

Figure 3.12: Voltage activated potassium conductances affect EPSP shaping II, A EPSP half width plotted against the absolute EPSP amplitude. Black circles depict data of recordings during control conditions, gray circles during the blockade of voltage activated potassium channels. Linear regression fits to both data populations match in colour. **B** Normalized EPSP peak amplitude plotted against the underlying simEPSC for control data (black) and in the presence of 2 mM 4AP (gray). **C** Change in resting membrane potential, when voltage activated potassium conductances are blocked.

voltage activated potassium conductances (gray traces). This comparison shows that blocking the voltage activated potassium conductances with 4AP leads to an increase in EPSP halfwidth. When plotting the EPSP half width against the EPSP's absolute peak amplitude the change becomes more obvious (see fig. 3.12 A). The data population recorded in the presence of 4AP (gray circles) is right and up shifted compared to the control data (black circles). The linear regression fits to both data populations (same colour code) display this relationship by a right shift for 4AP data, while their slopes stay the same (-0.148 ms/mV for control, -0.15 ms/mV for 4AP data). This change in half width is statistically significant ($p < 0.05$). Beside the increased half widths also the absolute peak amplitude of EPSP-like voltage defelctions is affected when voltage activated potassium conductances are blocked (see fig. 3.12 B). This change does not affect EPSPs elicited by smaller simEPSCs, but when greater charges are transferred (from 5 nA on) the block of potassium channels results in EPSPs of higher peak amplitudes. The response to the largest simEPSC was increased on average by 22 % when voltage activated potassium channels were blocked. To allow for comparison of results of different cells EPSP peak amplitudes were normalized to the response evoked by the largest

simEPSC of each cell under control conditions. To confirm that this change in EPSP peak amplitude is not caused by a change in membrane resting potential resting potentials before and after the wash in of 4AP are displayed in figur 3.12 C. On average the membrane resting potential changes from -60.87 mV to -57.44 mV. This is a change of 5.6 % and cannot account alone for the change in EPSP peak amplitude. Taken together, these results show that voltage activated potassium channels contribute to EPSP summation. In contrast to NMDAR mediated currents potassium conductances lead to EPSP with smaller amplitudes and half widths and thereby counteract the amplification of postsynaptic integration in DNLL neurons.

3.8.1 $K_{v1.x}$ and $K_{v3.x}$ conductances seem not to contribute to the modulatory effect of voltage activated potassium conductances

We showed that voltage activated potassium conductances contribute to the EPSP summation in DNLL neurons. In a next step we aimed to test if the subfamily of voltage activated potassium channels responsible for this modulatory effect can be specified. Therefore, we repeated the previous experiment but instead of blocking voltage activated potassium channels unspecifically with 2 mM 4AP different subfamilies of potassium conductances were blocked pharmacologically.

First, we wanted to determine the influence of DTX sensitive potassium conductances on EPSP summation and blocked therefore $K_{v1.1}$, $K_{v1.2}$ and $K_{v1.6}$ conductances with 100 nM α-DTX (n=5; Mathie et al., 1998). To analyze if EPSP summation is effected by the block of DTX sensitive conductances we again plotted the half width of the evoked EPSPs against the corresponding EPSP absolute peak amplitudes (see fig. 3.13 A). Although the slopes of the linear regression fits to both data populations (black for control, gray for DTX block) are different, the populations display no significant shift ($p > 0.05$) as seen before when conductances were

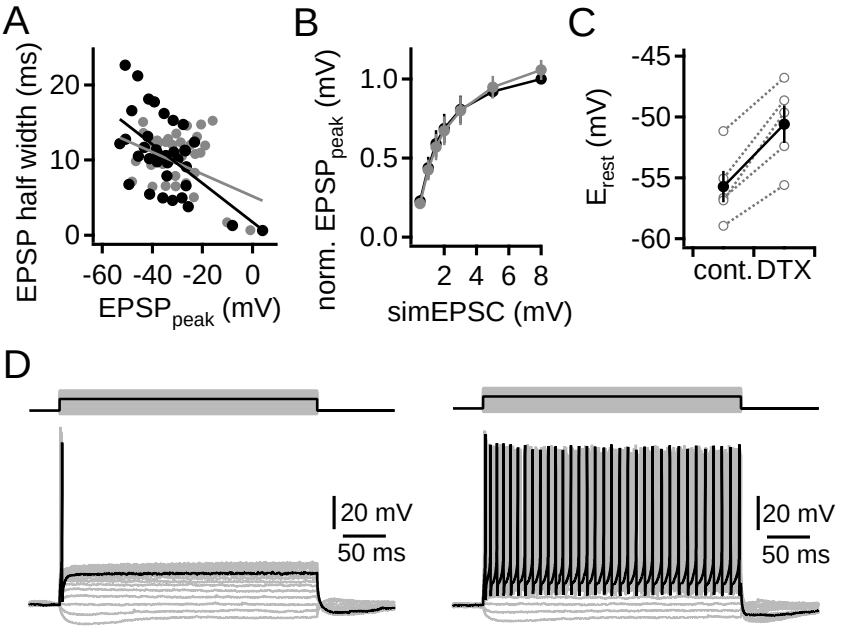

Figure 3.13: $K_{v1.1}$, $K_{v1.2}$ and $K_{v1.6}$ conductances seem not to effect EPSP shaping, A EPSP half width plotted against the absolute EPSP amplitude. Black circles depict data of recordings during control conditions, gray circles in the presence of 100 nM α-DTX. Linear regression fits match data populations in colour. **B** EPSP peak amplitude as a function of the underlying simEPSC's charge. EPSP amplitudes were normalized to EPSP peak evoked by largest simEPSC under control condition. Colour code as in A. **C** Membrane resting potential before and after the wash in of α-DTX. **D** IV-curve of an MNTB neuron before (left panel) and after (right panel) the application of α-DTX.

blocked with 4AP (see fig. 3.12 A). Also the normalized EPSP peak amplitudes shown as a function of the underlying simEPSCs' charge did not depict no differences between the two data populations (see fig. 3.13 B, colour code as before). Only the membrane resting potential is slightly depolarized from on average -55.73 $\pm$ 1.3 mV before to -50.61 $\pm$ 1.54 mV after the wash in of α-DTX (see fig. 3.13 C). To confirm that the used concentration of α-DTX was high enough to block $K_{v1.x}$ conductances we recorded IV-curves of MNTB neurons without and in the presence of 100 nM α-DTX (see fig. 3.13 D). As reported by Brew and Forsythe (1995) the application of α-DTX leads to an ongoing spiking in MNTB neurons. This showed that the used DTX concentration was sufficient to block $K_{v1.x}$ conductances. These results show that $K_{v1.1}$, $K_{v1.2}$ and $K_{v1.6}$ conductances do not contribute to EPSP

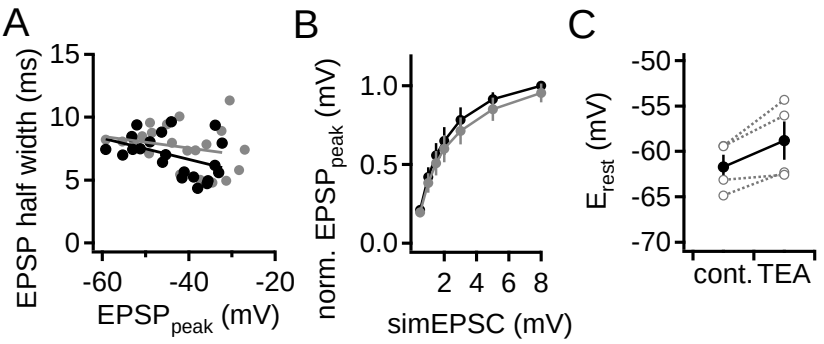

Figure 3.14: $K_{v3.x}$ conductances seem not to effect EPSP shaping, A EPSP half width plotted against the absolute EPSP amplitude. Black circles depict data of recordings during control conditions, gray circles during the blockade of $K_{v3.x}$ conductances with 0.5 mM TEA. Linear regression fits to both data populations match in colour. **B** EPSP peak amplitude as a function of the underlying simEPSCs' charge. EPSP amplitudes were normalized to EPSP peak evoked by largest simEPSC under control condition. Colour code as in A. **C** Membrane resting potential before and after the wash in of TEA.

summation in DNLL neurons.

In a second set of experiments we wanted to test the effect of $K_{v3.x}$ potassium conductances on the EPSP summation in DNLL neurons. We therefore repeated the previous experiments once more and used 0.5 mM TEA to block $K_{v3.x}$ conductances (n=4; Mathie et al., 1998). To analyze if EPSP summation is effected by the block of $K_{v3.x}$ conductances we again plotted the half width of the evoked EPSPs against the corresponding EPSP absolute peak amplitudes (see fig. 3.14 A). Data recorded in the presence of 0.5 mM TEA (gray circles) is not significantly shifted ($p > 0.05$) compared to data recorded under control conditions (black circles). The normalized EPSP peak amplitudes plotted against the charge of the underlying simEPSCs did not change significantly either (see fig. 3.14 B, same colour code as in A). As seen before in the presence of 4AP and DTX the membrane resting potential was slightly depolarized after the wash in of TEA. The resting potential changed on average from -61.71 $\pm$ 1.36 mV to -58.8 $\pm$ 2.12 mV in the presence of TEA (see fig. 3.14 C). These results suggest that $K_{v3.x}$ conductances neither contribute to EPSP summation in DNLL neurons.

Here we showed that NMDAR mediated currents amplify AP generation in DNLL neurons of juvenile Mongolian gerbils and that this NMDA dependent modulation is still present in adult animals. NMDAR mediated currents thereby influence the GABAergic output of the DNLL neurons. It was shown that this NMDA dependent amplification of AP generation is mediated by an NMDA induced enhancement of EPSP summation (Porres et al., 2011). Further, we showed that calcium conductances do not influence EPSP summation and that potassium conductances in general counteract the EPSP summation in DNLL neurons. In the preliminary work on potassium conductances we were not able to further specify pharmacologically the potassium conductances contributing to the effect on EPSP summation.

Contribution to this work: viral vectors

Experimental conception of the work presented in section 4.1 Preliminary virus experiments was mainly done by B. Grothe, A. Klug and F. Felmy.

Design of experiments shown from section 4.2 PRV-152 infection on was done by B. Grothe, F. Felmy and C. P. Porres.

All data presented in the following (4 Results: viral vectors) was aquired and analysed by C. P. Porres. Stereotactical injections in adult animals were done with the help of I. Siveke.

4 Results: viral vectors

To increase the number of tools to analyze neural circuits in Mongolian gerbils, we aimed to find a viral vector capable of introducing genetic information in neurons of the gerbil's ascending auditory pathway. A suitable viral vector would have to fulfil the following characteristics defined under 1.5 on page 19. Therefore, we tested several viral constructs for their ability of infection in Mongolian gerbils, their neurospecificity, the proper function of the transgenic protein and, if those criteria were matched, the overall condition of the infected cells.

4.1 Preliminary virus experiments

In the beginning this project did not focus on the characterisation of different viral vectors for the use in Mongolian gerbils (see page 26). The idea was to use viral vectors for introducing ChR2 and NpHR into neurons of different nuclei (e.g. MNTB) of the auditory brainstem allowing to control those neurons by light exposure. The combination of electrophysiological recordings with the light induced manipulation of the infected neurons or if possible a complete infected nucleus was thought to increase the understanding of auditory processing. After testing several viral constructs it became apparent that the selection of an suitable viral vector was more difficult than expected. The aim of the study changed to a systematic characterisation of a viral vector to find a usefool tool for gene transfer in Mongolian

gerbils. In this section the data of the first virus experiments is summarized. Due to the different aim of this first experiments the data is not sufficient in quality nor in quantity to fulfill the requirements of a systematic characterisation of a viral vector. Nevertheless, the results are presented in the following to point out the problems which are accompanied with the use of viral vectors.

4.1.1 Lentiviral induced infection

Lentiviruses introduce stable expression of transgenic protein in dividing and non-dividing cells without extense damage of the host cells. Therefore lentiviral constructs are widely used in gene therapy and general gene trasnfer to cells in other systems than Mongolian gerbils (Blömer et al., 1997; Lois et al., 2001). Here, we wanted to test if the useful characteristics of lentiviruses are also apparent in Mongolian gerbils. Therefore the IC and MNTB in Mongolain gerbils were infected by stereotactic injections with different lentiviral vectors. All viral vectors used coded for a fluorescent protein so that the success of gene transfer could be monitored by fluorescent microscopy of fixed brain slices. Subsequently the neurospecificity of the different lentiviral constructs was analyzed by immunohistocemical stainings. In the intermediate-term the aim of our studies was to do patch-clamp recordings in infected brain sections. Substantial myelination in adult animals deteriorates the effective visualisation of brain sections, complicating patch clamp recordings. For this reason, juvenile animals (P15) were utilised for infections so that even after the expression time of up to one week myelination was not expected to be extensive.

In the first lentiviral construct tested, expression was controlled by the calmodulin dependent kinase II alpha promoter (CamKII-α). This viral vector (derived from the virus used by Boyden et al., 2005) coded for a ChR2 protein tagged with GFP (CamKII-ChR2). CamKII-ChR2 was stereotactically injected into the IC of

juvenile Mongolian gerbils. After an expression time of five days, animals were transcardially perfused and fixed brain sections (50 µm) were scanned for GFP expressing cells to control for the succesful gene transfer. No GFP expression was detectable (n=5, data not shown). The extension of expression time to seven days post injection (dpi) did not change this negative result (data not shown) indicating that the used lentiviral vector was not able to induce infection or expression in Mongolian gerbils. As previous studies reported that CamKII-α is expressed mainly in the cortex and only weakly in other parts of the brain and is therefore most suitable for genetic manipulations of cortical neurons (Burgin et al., 1990; Dittgen et al., 2004), it was decided to use a different promoter to control the expression of the lentiviral vector. Therefore, the CamKII-α promoter was exchanged for the rat synapsin I promoter, which was shown to be expressed throughout the rat brain (Melloni et al., 1993).

Three different lentiviral constructs under the control of the synapsin I promoter were tested. One of these lentiviruses coded for eGFP (SynGFP), the second and third construct induced the expression of GFP tagged ChR2 (SynChR2) and eGFP tagged NpHR (SynNpHR, see 2.5.1). Experiments were done as described above with a expression time of seven days. Figure 4.1 A (upper panels) shows SynGFP induced infection in the IC at 7 dpi under 10x and 40x magnification (n=2, scale bars 100 µm and 20 µm, respectively). In the 10x magnification image the infected area covers up to five hundred micrometers (see fig. 4.1 A, left upper panel). The infected cells show an homogeneous somatic fluorescence (see fig. 4.1 A, right upper panel). SynNpHR induced infections displayed a fluorescent pattern similar to SynGFP induced infections (n=4, data not shown).

The lower panels of figure 4.1 A show SynChR2 induced infection at 7 dpi in the IC (n=4, 10x and 40x magnification, scale bars 100 µm and 20 µm). Again, small fluorescent spots are spread over an area of several hundred micrometers.

However, only in a few cells is fluorescent protein spread over the whole cell body (see fig. 4.1 A, left bottom panel, white arrow). The 40x magnification image of SynChR2 induced infections clearly shows that fluorescence is not evenly spread over cell somata as in SynGFP induced infections (see fig. 4.1 A, right bottom panel). Nonetheless, the data presented so far shows that SynGFP and SynNpHR are equally capable of infecting cells in the IC and that GFP and NpHR-GFP are expressed. The data further suggests, that SynChR2 is also able to infect cells in the IC, but it seems that either the extent of infection or expression induced by SynChR2 is stunted.

Therefore, in the next set of experiments only SynNpHR was used. First, the neurospecificity of SynNpHR infection in the IC was analyzed with an immunohistochemical MAP2 staining. In a second experiment it was tested whether SynNpHR is able to infect cells in the auditory brain stem. Neurospecificity of this infections were again analyzed with a MAP2 staining. SynNpHR was stereotactically injected into the IC (n=2) and MNTB (n=2) of P15 Mongolian gerbils. Animals were perfused seven dpi and 50 µm thick brain sections were obtained. Figure 4.1 B shows SynNpHR infected neurons in the IC (left panel). Corresponding MAP2 staining is seen in middle panel and overlay is displayed on the right (100x magnification, scale bars 10 µm). Two out of the four SynNpHR infected IC cells are co-stained for MAP2 (white arrows indicate cells, which express eGFP only). Figure 4.1 C left

Figure 4.1 *(following page)*: Lentivirus induced infection in the IC and the MNTB, A SynGFP construct: lentivirus with a synapsin I promoter coding for eGFP. IC cells of P15 gerbils show marked expression of eGFP, 7 days post injection (dpi). SynChR2 construct: lentivirus with a synapsin I promoter coding for ChR2 tagged with GFP. Infected IC neurons of P15 gerbils show only weak expression of eGFP, 7 dpi. Scale bars: 100 µm for 10x magnification, 20 µm for 40x magnification. **B** SynNpHR construct: lentivirus with a synapsin I promoter coding for NpHR tagged with eGFP. Several IC cells are infected (left panel). Neurospecificity of infection was tested by immunohistochemical MAP2 staining (middle panel). White arrows mark cells which show eGFP expression, but no MAP2 staining. Scale bars: 10 µm, 100x magnification **C** SynNpHR induced expression in the MNTB of P15 gerbil, 7 dpi. No MNTB principal cells are infected (left panel). MAP2 staining reveals clearly MNTB principal cells (middle panel). Scale bars: 10 µm, 100x magnification

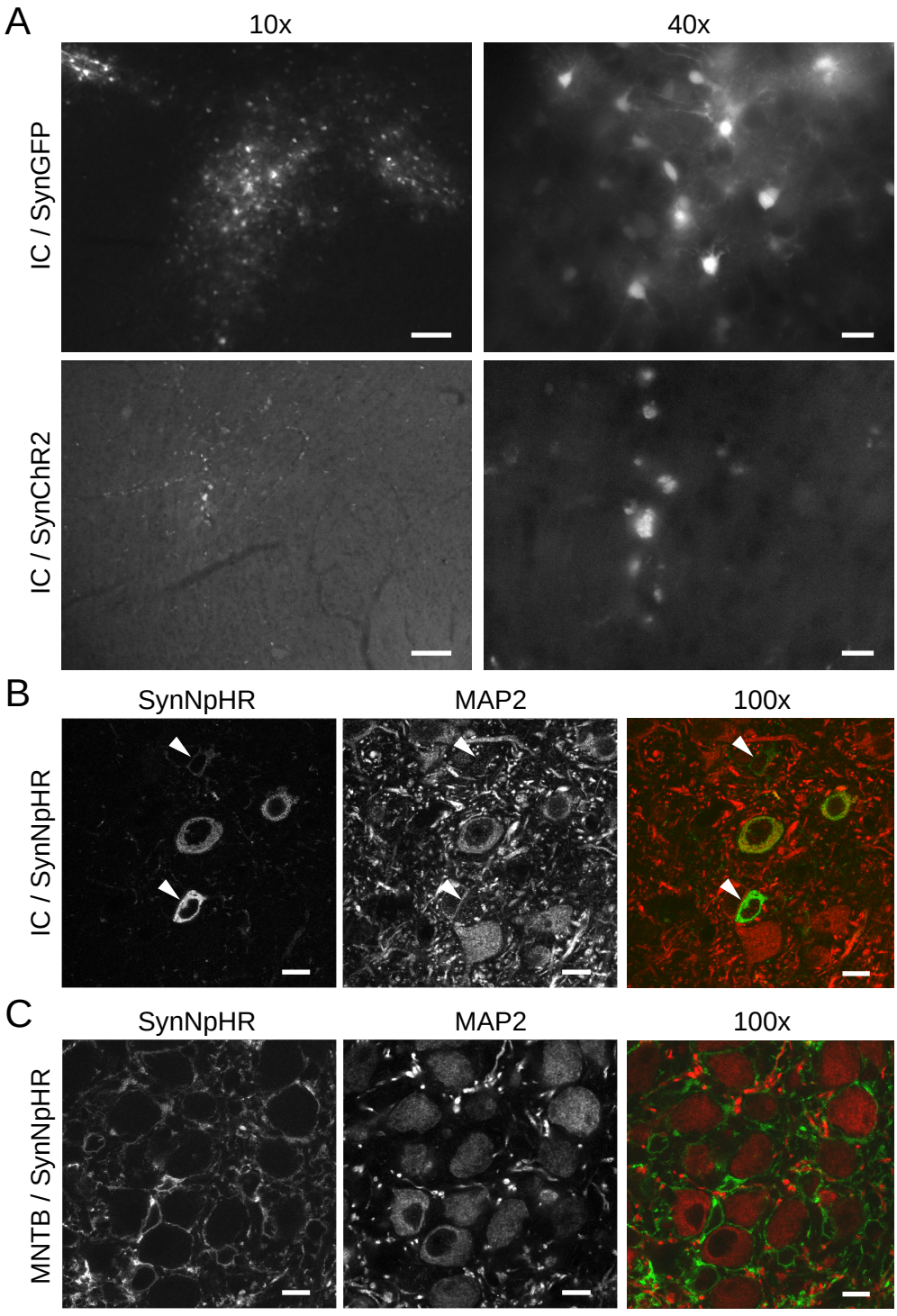
A
10x
40x
IC / SynGFP
IC / SynChR2
B
SynNpHR
MAP2
100x
IC / SynNpHR
C
SynNpHR
MAP2
100x
MNTB / SynNpHR

panel shows SynNpHR induced infection in the MNTB (P15, 7 dpi). Also MNTB principal neurons are clearly detectable in the MAP2 staining (see fig. 4.1 C, middle panel, 100x magnification, scale bar 10 µm). However, in the MNTB SynNpHR infection is restricted to presynaptic terminals or glia cells (see fig. 4.1 C, left and right panel).

The lentiviral vector under the control of the CamKII-α promoter was not able to induce infection in the IC. In this experimental approach it did not fulfill any of the four required properties for a viral vector (0/4) and is therefore not suitable for gene transfer into neurons in the IC of Mongolian gerbils. Also SynGFP seemed to induce only a minor infection in IC cells and thus failed similar to CamKII-ChR2 all of the previously defined requirements of a viral vector (0/4). SynGFP could infect IC cells in Mongolian gerbils and the fluorescence proved the funcitonality of the reporter gene. The vector fulfilled at least two out of four conditions (2/4). Neurospecificity and cytotoxicity of this virus were not tested as SynNpHR was more interesting for the planned experimental design. SynNpHR was able to induce infection cells in the IC and MNTB. In the IC neurons and glia cells were, while in the MNTB the infection was restricted to presynaptic terminal or glia cells. MNTB principal neurons seemed not to be infected at all by SynNpHR. Due to the malfunction of infection or neurospecifity (1-2/4) neither the function of NpHR nor cytotoxic effects of the lentiviral infection were analyzed.

4.1.2 Semliki Forest viral induced infection

Next, a Semliki Forest virus (SFV) was tested for its properties as viral vector in Mongolian gerbils. The advantage of SFV based expression systems compared to lentiviral vectors is the fast expression of the induced transgenic proteins (Lundstrom, 1999). However, as SFVs are also highly cytotoxic, the time window for

experiments was limited to a maximum of ∼14 hpi (Lundstrom, 1999). The SFV construct used here encoded a ChR2 tagged with RFP. It was stereotactically injected (100 to 1500 nl virus solution) into the IC and MNTB of P15 Mongolian gerbils. 8 hpi brain slices (200 µm) were obtained for patch clamp recordings or animals were transcardially perfused to obtain brain sections for immunohistochemical MAP2 staining (60 µm). In Figure 4.2 A the infection site of a SFV induced infection in the IC is shown. The 10x magnification image (left panel) shows that the infection is spread over several hundred micrometers. Cell somata and neurites are clearly visible due to RFP expression (see fig. 4.2 A, left and right panel).

It was reported that in some SFV strains the neurospecificity of infection was temperature dependent (Ehrengruber et al., 2003). Specifically, higher temperatures lead to an increase in infected glia. Given that during *in vivo* stereotactic injections the temperature during expression time is relatively high and not modifiable we aimed to test if the SFV construct is able to infect neurons under this conditions. To analyze the neurospecificity of SFV infection we obtained 40 µm thick brain sections 8 hpi and stained them with MAP2 (n=2, see fig. 4.2 B, 63x magnification, scale bars 10 µm). Two SFV infected IC neurons are visible (white arrows, left panel). Both infected cells show weak MAP2 staining (white arrows, middle panel).

After the confirmation that neurons could be infected by the SFV construct, the next step was to determine if the introduced transgenic ChR2 protein was functional. SFV was injected into the IC of P15 gerbils and brain sections for patch clamp experiments were obtained 8 hpi. Cells were patched in current clamp mode and then exposed to 480 nm wavelength light. In IC neurons we were not able to evoke APs or depolarize the membrane potential by light exposure (n=7, data not shown). Nevertheless, in voltage-clamp mode, while clamping the neuron to different holding potentials (-90 mV to +40 mV with 10 mV increments, duration

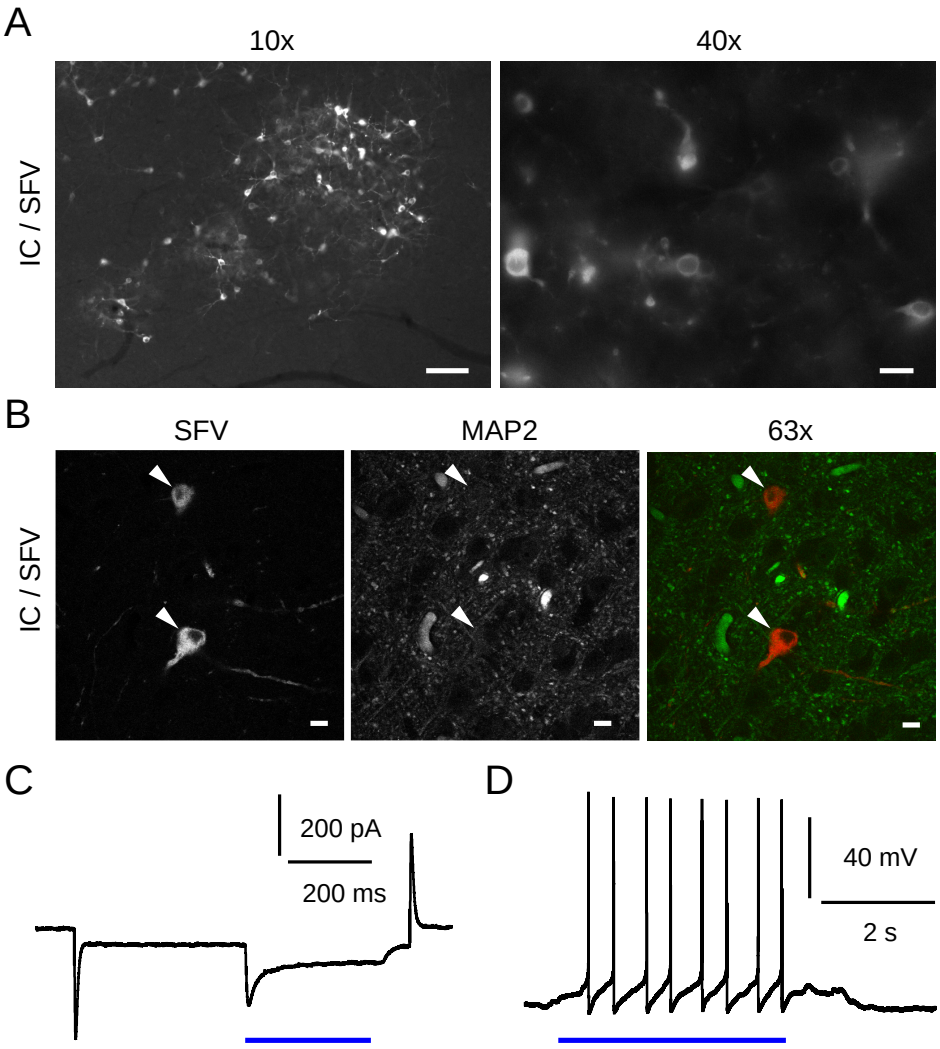

Figure 4.2: Semliki Forest virus induced infection the IC, A SFV construct codes for RFP tagged Channelrhodopsin 2. RFP expression in the IC 12 hours after virus injection. Scale bars: 100 µm for 10x magnification, 20 µm for 40x magnification. **B** 63x magnification of infected IC cells. Neurospecificity of infection was tested by immunohistochemical MAP2 staining. White arrows mark cells which show both, eGFP expression and MAP2 staining. Scale bar: 10 µm **C** Light induced modulation of current in infected IC neuron during a 800 ms voltage step. The infected neuron was exposed to 480 nm wavelength light (duration 300 ms) **D** Light induced APs in an infected neuron medial to the MNTB. Neurons were exposed to 480 nm wavelength light for 4 s.

800 ms), a light modulated current became apparent (exposure to light of 475 nm wavelength, 300 ms) in one cell (see fig. 4.2 C). During those patch-clamp experiments, several observations beside the general functionality of ChR2 could be made. First, although we showed that the SFV construct was capable of infecting neurons, the amount of infected glia was high (data not shown, no quantitative analysis was done). Second, most of the infected cells were in bad condition. While patching it was difficult to break through the cell membrane without destroying the cell. When whole-cell mode was achieved, the cells often displayed a strongly depolarized resting potential (∼-45 mV, no quantitative analysis was done).

In the following the expression of ChR2 protein was also assessed in the MNTB. It was of major interest if SFV infected MNTB cells would also show the alterations observed in SFV infected IC cells. Therefore, SFV was stereotactically injected into the MNTB. Cells were succesfully infected both in and around the MNTB (data not shown). All stereotactic virus injections were performed without recording responses evoked by auditory stimuli. This procedure was successful for injections into the IC, but it was not suitable for MNTB injections. Only 60% of the stereotactic injections into the MNTB were successful (SFV: n=14, Lentiviruses: n=4). In none of the performed stereotactic injection into the MNTB was the virus injection restricted to the MNTB only.

Nevertheless, as in the previous experiment, brain slices from SFV infected animals were obtained 8 hpi and RFP fluorescent cells in the MNTB were patch-clamped. Similar to the SFV infected IC cells, no APs could be evoked by exposure to 480 nm light in current-clamp mode. Additionally, when infected MNTB cells were patched in voltage clamp mode and exposed to light during hyper- and depolarizing voltage steps no modulation of the induced currents was detectable (n=7). Interestingly, in some larger shaped neurons outside the MNTB, it was possible to reproducibly induce light-evoked APs (n=3, see fig. 4.2 D). These neurons showed light-induced

firing frequencies of around 4-5 Hz, with a latency from light exposure-onset to AP peak beyond 100 µs(no quantitative analysis was done). As observed during the previous experiments in the IC, the general condition of SFV infected cells was poor. Cells were extremely fragile and exhibited a strongly depolarized resting membrane potential.

We could show that SFV was able to infect cells in the IC and MNTB of Mongolian gerbils and that the introduced ChR2 was funcitonal at least in some cells. Nevertheless, the neurospecificity of the viral vector is at least questionable and cytotoxicity induced by SFV was severe. Therefore only two to three out of four requirements for a viral vector were accomplished (2-3/4). We dediced not to follow this approach due to the apparent cytotoxicity, the resulting short experimental time window and the malfunction of ChR2, especially in the MNTB which was of major interest to us.

4.2 PRV-152 infection

PRV-152 was described as a tool for neural circuit analysis as it labels connected neurons retrogradely and hardly (if at all) affects their electrophysiological properties (Smith et al., 2000; Gao et al., 2009; Derbenev et al., 2010). However, a more recent publication challenges the non-invasiveness of PRV-152, at least for cell cultures (McCarthy et al., 2009). Here we wanted to assess if PRV-152 infects neurons in the gerbil's auditory brain stem, and if this is the case, we wanted to analyze how the infected cells are affected by PRV-152.

PRV-152 was stereotactically injected into the IC of juvenile Mongolian gerbils (P15). 50 hpi 60 µm thick brain sections containing the CN, SOC, LL and IC were cut, mounted and scanned for eGFP expression under a fluorescence microscope

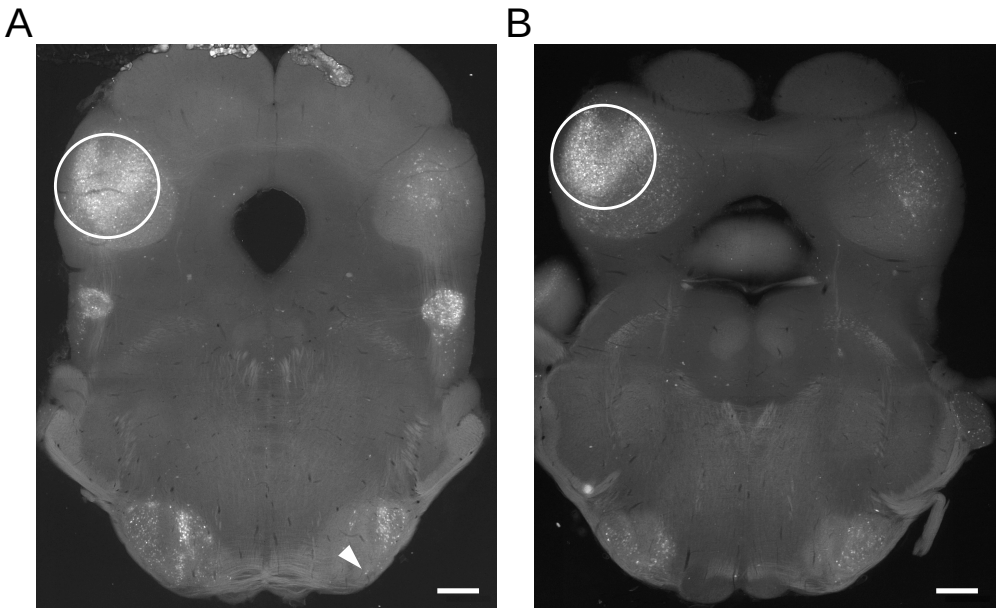

Figure 4.3: Pseudorabies virus-152 induced infection in the auditory pathway, A 50 hours after PRV-152 injection into the IC, eGFP expression is detectable in ipsi- and contralateral IC, DNLL and SOC cells. The IC at the injection site shows a higher level of fluorescence than the contralateral IC. At the level of the DNLL this relationship appears to be reversed. In the SOC ipsilateral to the injection site fluorescent cells are seen in the LSO, MSO, MNTB and SPN, while in the contralateral SOC mainly LSO and single MSO (white arrow) neurons are infected. **B** A more caudally situated brain section obtained from same animal as in (A). Pattern of fluorescence in the IC is similar to A. Fluorescent cells are detectable in the SOC where mainly LSO cells are infected. Additionally, eGFP expressing cells are visible in the CN contralateral to the injection site. In both brain sections eGFP expression seems to be highly restricted to the auditory pathway. Scale bars: 500 µm, 2.5x magnification, white circles mark injection sites.

(n=2). Figure 4.3 displays two overview screens of those brain stem slices (2.5x magnification, scale bars 500 µm). Both images were taken from brain sections obtained from the same animal. Figure 4.3 A shows a more rostral section than figure 4.3 B. eGFP expressing cells in both ICs, DNLL and SOCs are clearly detectable. At the injection site (white circles) the number of infected cells appears to be considerably higher than in the IC contralateral to the injection site (see fig. 4.3 A,B). At the level of the DNLL this result seems to be inverted; it seems that the contralateral DNLL contains a higher number of eGFP expressing cells (see fig. 4.3 A). However, the right DNLL also appears to be bigger than the ipsilateral

DNLL, suggesting that both DNLL are not cut at the same rostro-caudal level. This difference in section plane may contribute to the impression that infection rates at both DNLL are unequal. Ventral to both DNLL, possibly located in the INLL, several eGFP expressing cells are visible. Ipsilateral to the injection site, fluorescent cells are detectable in the LSO, the MSO and the SPN (see fig. 4.3 A). Few eGFP expressing cells are located in the ipsilateral MNTB (see fig. 4.3 A). In the contralateral SOC, infected cells are mainly seen in the LSO. Only a few fluorescent cells are located in the contralateral SPN and MSO (see fig. 4.3 A, white arrow). In the more caudal brain section (see fig. 4.3 B) the fluorescent pattern seen in the IC is similar to the pattern described in figure 4.3 A. Both LSOs also show eGFP expressing cells, though in the LSO ipsilateral to the injection site the infection is spread over a wider area than in the contralateral LSO (see fig. 4.3 B). Infection of cells in the contralateral CN is detectable. In both brain section only few fluorescent cells are located outside the auditory nuclei.

4.2.1 Time course of PRV-152 infection

So far we showed, that after stereotactic injection into the IC, PRV-152 is able to infect cells in the auditory brain stem of juvenile Mongolian gerbils. The fact that the infection seems to be restricted to the auditory pathway suggests that the PRV-152 infection is, as reported previously, generally spread through connected neurons (Card et al., 1990) and hence at least to some degree neurospecific. By the spread of the infection from the injection site to several auditory nuclei we know that by 50 hpi definitely 2nd order neurons are infected. Single eGFP expressing cells in the contralateral MSO and INLL and the ipsilateral MNTB (see fig. 4.3 A) indicate that 50 hpi the infection is already spread to 3rd order infected neurons (Coleman and Clerici, 1987; Kelly et al., 2009). Therefore, to specify the time point of the first synaptic crossing, the time course of the PRV-152 infection was of major

interest.

Again, PRV-152 was stereotactically injected into the IC of P15 Mongolian gerbils. After expression times, ranging from 12-50 hours, animals were transcardially perfused and 60 µm thick brain sections were sliced and mounted. Figure 4.4 shows brain section obtained ∼23, 26 and 36 hpi (injection sites are marked by white circles, n=2 for each expression time). ∼23 hpi the expression of eGFP was restricted to the injection area only (see fig. 4.4 A, scale bars 500 µm, 2.5x magnification). eGFP expressing cells were not detectable in either the contralateral IC (top panel) or in other nuclei of the auditory pathway (bottom panel). 26 hpi infection at the injection site is still restricted to a small area (see fig. 4.4 B, upper left panel, scale bar 500 µm, 2.5x magnification). But in several other nuclei of the auditory pathway some eGFP expressing cells are visible. The infection is spread to the contralateral IC (see fig. 4.4 B, upper right panel, scale bar 100 µm, 10x magnification) and to ipsi- and contralateral DNLL and SOCs (bottom panels, contralateral nuclei not shown, scale bars 100 µm, 10x magnification). After another ten hours of expression intense fluorescence is seen throughout the nuclei of the auditory pathway (see fig. 4.4 C, scale bars 500 µm, 10x magnification). The left panels of figure 4.4 C show overviews of brain sections containing fluorescent cells in both ICs, SOCs and CNs. The middle and right panels give detailed pictures of ipsi- and contralateral DNLL and SOCs. Infection is widely spread at the injection site (white circle), and in the contralateral IC many cells show eGFP expression (upper left panel). Both DNLL contain fluorescent cells, and eGFP expressing cells are also present ventral to the DNLL, especially ipsilateral to the injection site (upper middle and right panel, scale bars 500 µm, 2.5x magnification). In the ipsilateral SOC, cells of the LSO, MSO and SPN are infected, but no fluorescent MNTB cells are apparent (middle bottom panel). In the contralateral SOC, infection is restricted to the LSO (right bottom panel, scale bars 500 µm, 10x magnification). Aside from the SOC, fluorescent cells are apparent in ipsi- and contralateral CNs (see fig. 4.4 C, left

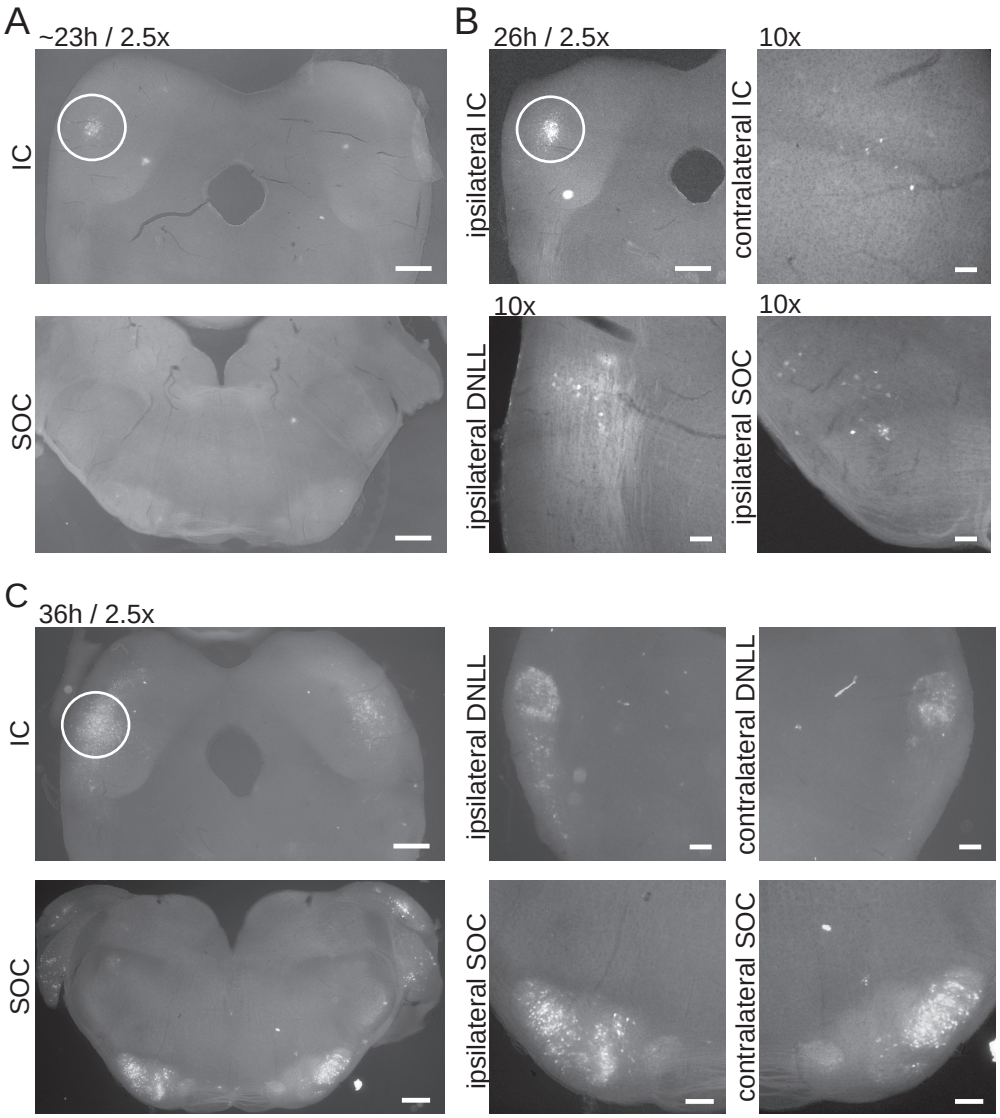

Figure 4.4: Time course of Pseudorabies virus-152 induced infection, A ∼23 hpi PRV-152 infection is still restricted to the injection site (white circle). Scale bars: 500 µm, 2.5x magnification. **B** 26 hpi eGFP expression is detectable in areas of the auditory pathway outside of the injection site (white circle). Individual cells in the contralateral IC, ipsi- and contralateral DNLL and SOCs show eGFP expression. Data for contralateral DNLL and SOC is not shown. Scale bars: 500 µm for 2.5x magnification; 100 µm for 10x magnification **C** 36 hours post injection eGFP expression in the complete ascending auditory pathway is intense. Overview images show eGFP expressing cells in both ICs, SOCs and CNs (left panels). Middle and left panels show ipsi- and contralateral DNLL and SOCs in more detail. Left panels: scale bars 500 µm, 2.5x magnification, white circle marks injection site. Middle and right panels: scale bars 200 µm, 2.5x magnification; n=2 for each expression time.

bottom panel). Similar to experiments where animals were perfused 50 hpi (see fig. 4.3), eGFP expression is mainly restricted to cells located in the ascending auditory pathway.

Taken together, this data shows that fluorescence in 2nd order infected neurons is apparent ∼26 hpi, suggesting that the synaptic cross happens a few hours earlier. The number of eGFP expressing cells increases in the hours following. Taking into consideration that the first synaptic spread happened after ∼20 hpi, this increase in number of fluorescent cells is most probably due to a delay in infection of 2nd order neurons and not to infection of 3rd order neurons. This interpretation is confirmed by the lack of fluorescent neurons, which are unambiguously 3rd order infected, e.g. MNTB neurons. Thus, it seems that the synaptic spread does not happen at a defined point of time in all infected neurons, but in fact occurs over a certain time range.

4.2.2 PRV-152 infects juvenile and adult Mongolian gerbils

The above experiments showed that PRV-152 is able to infect neurons in juvenile Mongolian gerbils. The first 2nd order infected neurons of a PRV-152 infection in juvenile Mongolian gerbils are detectable ∼26 hpi. At 50 hpi, the first 3rd order infected neurons are seen. In the following experiments we wanted to determine if adult Mongolian gerbils are also receptive to PRV-152 infection and if so, two further questions would be of interest: first, can the infection also be started in different nuclei of the auditory pathway? Second, is the time course of PRV-152 infection in adult animals similar to the time course in juvenile animals?

To answer this, we stereotactically injected PRV-152 in the IC and DNLL of P55-80 Mongolian gerbils and perfused the animals 36 hpi. Figure 4.5 A shows 60 µm thick brain sections obtained after stereotactic injection into the IC (n=2). Left panels

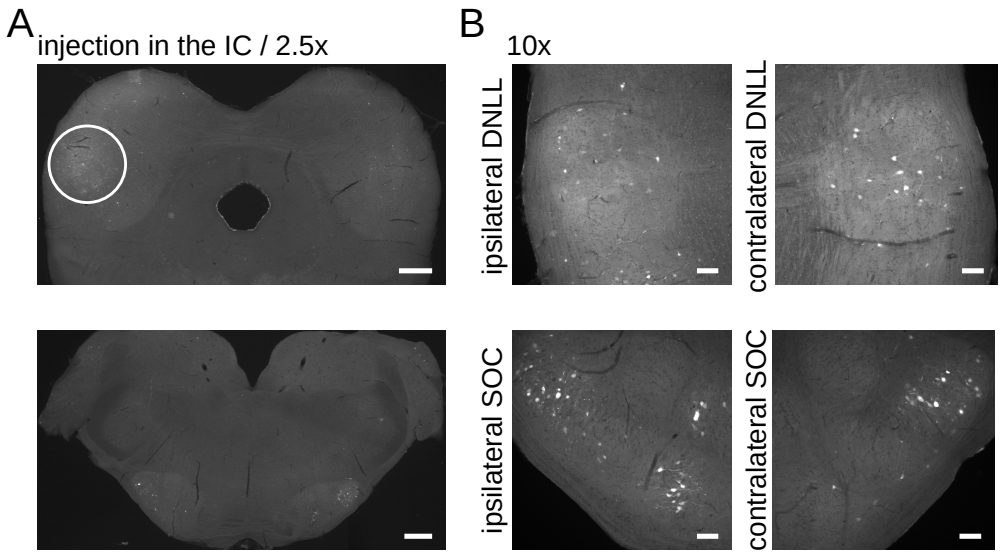

Figure 4.5: Pseudorabies virus-152 induced infection in adult animals, A PRV-152 infection induced by virus injection into the IC of an P65 animal, 36 hpi. Injection site is marked by white circle. eGFP expression is detectable in cells of both ICs, ipsi- and contralateral DNLL, SOCs and CNs. **B** Detailed views of brain sections containing ipsi- and contralteral DNLL (upper panels) and both SOCs (bottom panels) show a similar fluorescent pattern as observed in juvenile gerbils. Scale bars 500 µm for 2.5x magnification; 100 µm for 10x magnification.

show an overview of two sections containing ipsi- and contralateral ICs (upper panel) and SOCs (lower panel, scale bars: 500 µm, 2.5x magnification). In both ICs fluorescent cells are detectable, but as in juvenile gerbils the infection's spread is broader at the injection site (white circle) compared to the contralateral IC (see fig. 4.5 A, left upper panel). The overview section of the auditory brain stem clearly shows fluorescent cells in both SOCs and ipsi- and contralateral CNs (see fig. 4.5 A, left bottom panel). Middle and right panel of figure 4.5 A show both DNLL (upper panels) and SOCs (bottom panels) in more detail (scale bars: 100 µm, 10x magnification). eGFP expressing cells are located in both DNLL. As seen in juvenile animals, fluorescent cells are also seen ventral to the DNLL ipsilateral to the injection site. Equally, the expression pattern in both SOCs exhibits similarities to the one seen in P15 Mongolian gerbils. In the ipsilateral SOC infection is seen in the LSO, MSO and SPN, while at the contralateral side infection is mainly

restricted to the LSO (compare fig. 4.5 A, right bottom panels with figs. 4.3 and 4.4).

As in previous experiments, fluorescent cells were mostly located in nuclei of the auditory brain stem. While the fluorescence pattern looks similar to that in previous experiments, the number of infected cells appears to be slightly reduced in adult animals when PRV-152 is injected into the IC (n=2). This difference could be caused by a different time course of infection. If PRV-152 infection spreads more slowly in adult animals, the number of infected cells would still increase over the next hours. It might also be possible that adult animals are less vulnerable to PRV-152 infection, due to differences in the immune system or different expression of cell membrane proteins necessary for virus interaction.

4.2.3 PRV-152 infection can be started in different nuclei of the auditory system

Having established that PRV-152 is able to induce infection in adult Mongolian gerbils, we now wanted to test if PRV-152 infection can also be initiated in nuclei other than the IC. Therefore, PRV-152 was injected into the DNLL of two adult Mongolian gerbils. Animals were perfused 36 hpi and 60 µm thick brain sections were mounted.

Figure 4.6 A shows the fluorescence pattern of a PRV-152 infection initiated in the DNLL of an adult Mongolian gerbil (36 hpi). Both panels give an overview of two brain sections, showing both DNLL (upper panel), SOCs and CNs (lower panel, scale bars: 500 µm, 2.5x magnification). Fluorescent cells are seen in both DNLL, the INLL and VNLL ipsilateral to the injection site and both SOCs and CNs. Figure 4.6 B shows both DNLL (upper panel) and SOCs (lower panel) in more detail (10x magnification, scale bars 100 µm). At the injection site eGFP expressing cells are

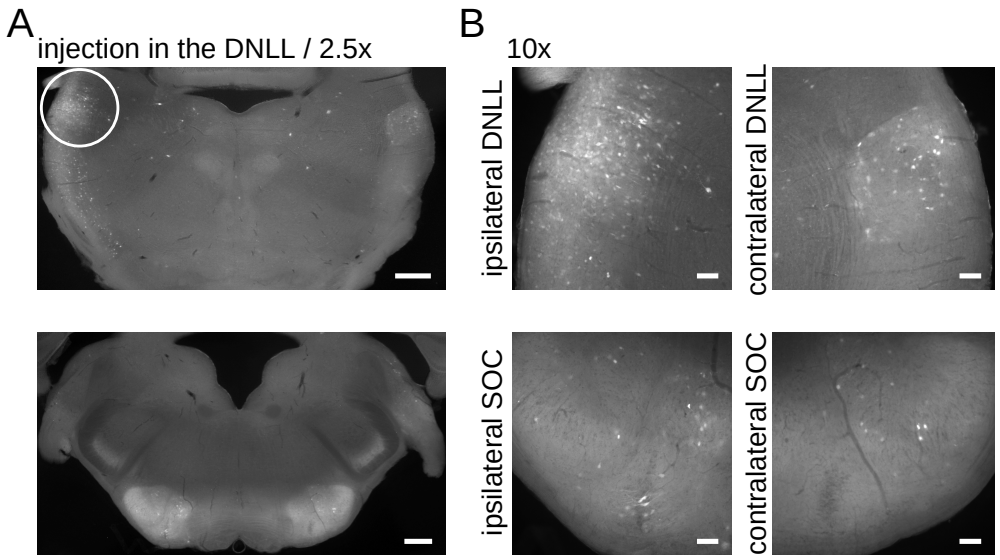

Figure 4.6: Pseudorabies virus-152 infection induced by stereotactical injection into the DNLL, A PRV-152 infection induced by virus injection into the DNLL of a P80 animal, 36 hpi. Injection site is marked by white circle. PRV-152 infection can be initiated in different nuclei. eGFP expressing cells are located in ipsi and contralateral DNLL, SOCs and CNs. **B** Detailed views of brain sections containing ipsi- and contralateral DNLL (upper panels) and SOCs (bottom panels). Infection in the contralateral SOC is restricted to the LSO, while ipsilaterally LSO, MSO and SPN cells are infected. Scale bars 500 µm for 2.5x magnification; 100 µm for 10x magnification.

clearly detectable in the DNLL and ventral to it (upper left panel). Additionally fluorescent cells are located all around the DNLL (upper middle panel). Due to the small size of the DNLL, it is easily possible that during the injection virus solution leaks out of the nucleus' boundaries and causes infection of cells outside the DNLL. This might happen, depending on the amount of injected virus solution, even when the injection pipette is placed properly inside the DNLL. The contralateral DNLL contains eGFP expressing cells (upper right panel), as does the contralateral LSO (lower right panel). The ipsilateral SOC contains fluorescent cells, specifically in the LSO, MSO and SPN (middle bottom panel).

This data shows that PRV-152 can infect neurons in adult Mongolian gerbils. Furthermore it proves that PRV-infection can be initiated in different nuclei of the auditory pathway. As observed before spread of PRV-152 infection in adult ani-

mals seems to be slower or weaker compared to juvenile animals.

4.3 PRV-152 infection is mainly neurospecific

From the data presented so far, it is apparent, that PRV-152 infects juvenile and adult Mongolian gerbils. The infection is spread retrogradely through connected neurons and first 2nd order infected cells show fluorescence ∼26 hpi. To determine if PRV-152 is indeed a suitable viral vector in Mongolian gerbils the next aim was to analyze the neurospecificity of PRV-152 infection.

PRV-152 (200 µl virus solution) was stereotactically injected into the IC of P15 Mongolian gerbils. Animals were perfused 36 hpi, 40 µm thick brain sections were taken and immunohistochemically stained for MAP2 or S100β. Image stacks were taken with a confocal microscope. Figure 4.7 A displays eGFP expressing cells (green channel) in the ipsilateral IC and DNLL (left panels, scale bars: 20 µm, 63x magnification). Corresponding MAP2 staining (red channel) and overlay are presented in middle and right panels (scale bars: 20 µm, 63x magnification). White arrows in each image show cells which express eGFP but not MAP2. Figure 4.7 B shows example images of a S100β staining. As in 4.7 A, left panels show eGFP expressing cells (green channel) in the ipsilateral IC and DNLL, middle panels

Figure 4.7 *(following page)*: Neurospecificity of PRV-152 induced infection I, A Immunohistochemical MAP2 staining in brain slices of PRV-152 infected animals. Virus was injected into the IC of P15 gerbils (n=3, brain sections of two of these animals were also used for S100β staining). Animals were perfused 36 hpi. Left panels show eGFP expressing cells, middle panels display MAP2 staining and right panels depict overlay. White arrows mark cells, which show eGFP expression, but no MAP2 staining. Scale bars: 20 µm, 63x magnification. **B** Immunohistochemical S100β staining in brain slices of PRV-152 infected animals. Virus was injected into the IC of P15 gerbils (n=3, brain sections of two of these animals were also used for MAP2 staining). Animals were perfused 36 hpi. Left panels show eGFP expressing cells, middle panels display S100β staining and right panels depict overlay. White arrows mark cells, which show eGFP expression and S100β staining. Scale bars: 20 µm, 63x magnification.

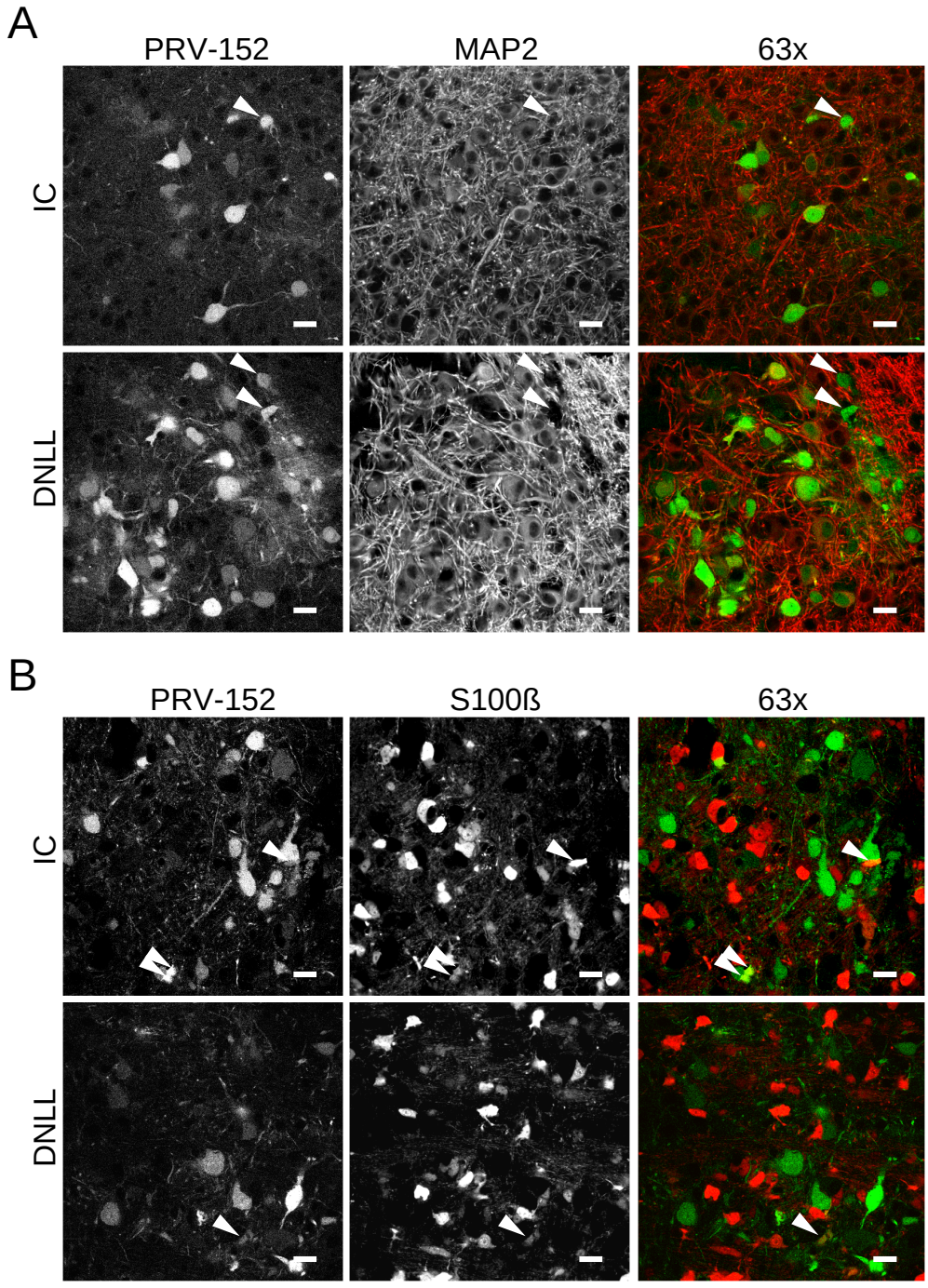
A
PRV-152
MAP2
63x
IC
DNLL
B
PRV-152
S100ß
63x
IC
DNLL

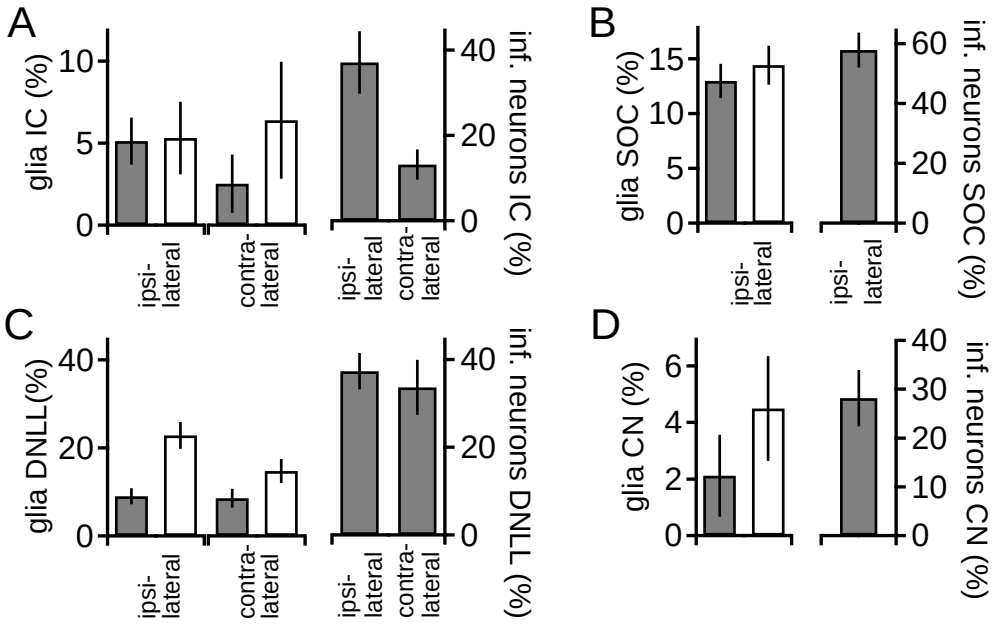

Figure 4.8: Neurospecificity of PRV-152 induced infection II, A Quantitative analysis of PRV-152 infection in ipsi- and contralateral IC. Left panel shows percentage of infected glia cells (ratio of infected glia cells to all infected cells, in percent). Gray bars show percentage of eGFP expressing, MAP2 negative cells in both ICs. White bars show percentage of cells which show both eGFP expression and S100β staining. Right panel: PRV-152 infected neurons in the IC (ratio of infected neurons to all MAP2 stained cells in the IC, in percent). **B** Quantitative analysis of PRV-152 infection in the SOC ipsilateral to the virus injection site. Left panel shows percentage of infected glia cells, right panel shows percentage of infected neurons (same analysis and colour code as in A). **C** Quantitative analysis of PRV-152 infection in ipsi- and contralateral DNLL. Left panel shows percentage of infected glia cells, right panel shows percentage of infected neurons (same analysis and colour code as in A). **D** Quantitative analysis of PRV-152 infection in the CN. No diistinction was made between ipsi- and contralateral CNs. Left panel shows percentage of infected glia cells, right panel shows percentage of infected neurons (same analysis and colour code as in A).

show S100β staining (red channel) and right panels display overlays (scale bars 20 µm, 63x magnification). White arrows indicate cells that express both eGFP and S100β. These example images already indicate that many PRV-152 infected cells are neurons.

Further image analysis was used to quantify the ratio of infected neurons to non-neural cells (see fig. 4.8). In MAP2 stainings the number of double stained cells (eGFP expressing and marked by MAP2) was determined. Additionally, the num-

ber of all MAP2 stained and all only eGFP expressing cells was counted. The number of all GFP expressing cells and the number of cells which did show eGFP but no MAP2 staining was used to determine the ratio of infected glia cells to all infected cells. The number of all MAP2 stained cells and the number of double stained cells was used to calculate the ratio of infected neurons to all neurons (infection rate). In S100β stainings eGFP expressing cells and double fluorescent cells (eGFP expressing and marked by S100β) were counted. These numbers were used to calculate the ratio of infected glia cells to all infected cells. For this quantitative assay two images from each confocal stack were analyzed. Care was taken that the distance between both images was large enough to ensure that no cell was counted twice (>25 µm). Data was acquired for ipsi- and contralateral IC and DNLL and ipsilateral SOC. In case of the CN no distinction was made between data collected ipsi- or contralaterally. In three animals per immunohistochemical staining, one to six (two on average) confocal stacks were taken for each nucleus. In the following section "n" gives the number of images analyzed per nucleus.

The left panel of figure 4.8 A shows the percentage of glia cells from all PRV-152 infected cells in the ipsi- and contralateral IC (left panel). Throughout the figure gray bar graphs display data based on MAP2 stainings , white bar graphs show data based on S100β stainings. Ipsilaterally, the percentage of glia cells is 5.13 ± 1.43 % based on the analysis of the MAP2 stainings (n=10). Using S100β stainings the percentage of glia is 5.31 ± 2.21 %(n=10). In the IC contralateral to the injection site, the percentage of glia is 2.52 ± 1.78 % in MAP2 staining (n=9) and 6.41 ± 3.57 % in S100β staining (n=11). The infection rate, the ratio of infected neurons to all MAP2 stained neurons, is 37.09 ± 7.28 % ipsilaterally (n=10) and 13.12 ± 3.57 % in the contralateral IC (n=9, see fig. 4.8 A, right panel). This difference in infection rate can be explained by the different expression times in the ipsi- and contralateral IC. An expression time of 36 hpi is acurate only for the cells in the ipsilateral IC where the injections were initially made. The expression time in

all other infected neurons is far less than 36 hours, given that the viruses needed ∼20 hours to spread to connected neurons in the contralateral IC and other nuclei. Therefore the expression time in all other infected neurons is far below 36 hours, which results in less infected neurons. In the DNLL the percentage of infected glia is slightly smaller than in the IC (see fig. 4.8 C, left panel). From the MAP2 staining (n=12), glia represent 8.96 ± 1.81 % of the infected population ipsilaterally and 8.56 ± 2.14 % contralaterally (n=10). From S100β stainings (n=10) these numbers are 22.78 ± 3.04 % ipsilaterally and 14.69 ± 2.75 % contralaterally. The infection rate in both DNLL is similar: 37.32 ± 4.12 % ipsilaterally and 33.68 ± 6.27 % contralaterally (n=10). The ipsilateral SOC has a higher percentage of infected glia cells with 12.96 ± 1.57 % for MAP2 (n=26) and 14.4 ± 1.79 % for S100β (n=24) stainings (see fig. 4.8 B, left panel). The infection rate is also increased (56.25 ± 3.13 %, n=26, right panel). In the CN only few glia cells are infected with 2.12 ± 1.45 % in MAP2 stainings (n=10) and 4.49 ± 1.86 % in S100β stainings (n=9). The infection rate in the CN is 28.15 ± 5.79 % (n=10, see fig. 4.8 D). On average, the percentage of infected glia is about 8.12 ± 0.87 % for MAP2 stainings and 11.94 ± 1.21 % in S100β stainings and infection rate varies between the nuclei from 13.12 ± 3.57 % in the contralateral IC to 56.25 ± 3.13 % in the ipsilateral IC. This results show that, as previously reported for other PRV strains, PRV-152 infection is highly neurospecific.

4.4 GFP expression induced by PRV-152 infection allows for detailed morphological analysis of infected neurons

So far it was shown that PRV-152 can infect neurons in different nuclei of the auditory pathway. The infection is highly neurospecific and therefore PRV-152

fulfils several of the prerequisites we previously defined for a suitable viral vector. As a next step we wanted to determine if PRV-152 can be used as a tool for morphological analysis of neurons.

PRV-152 induced eGFP expression in brain sections from previous experiments was analysed to determine the detail with which infected neurons could be visualised. Figure 4.9 shows several images taken of PRV-152 infected brain sections. Figure A shows images taken from brain sections of an PRV-152 infected animal perfused 50 hpi. Two overview maximal projections were stitched together from 26 confocal microscope stacks (scale bars: 200 µm, 20x magnification). The injection site (black circle) is located in the left IC (see fig. 4.9 A). The number of infected cells in the ipsilateral IC is far greater than the number of infected neurons in the contralateral IC. Both DNLL show strong eGFP expression and infected neurons are also visible ventral to these nuclei. Due to the large number of infected cells in the ipsilateral IC, few details in cell structure can be determined, though cell somata are visible. In contrast, in the contralateral IC, the neurites of several cells are visible. At the level of the DNLL on both sides, the fibres composing the Commissure of Probst are apparent (see fig. 4.9 A), as well as fibres projecting to the ICs. Fibres of the Commissure of Probst (contralateral to the injection site) are also shown in greater detail in (see fig. 4.9 B, scale bar 100 µm)). In some stacks it was possible to follow those projection far beyond the midline of the brain section. Figure 4.9 C shows a 63x magnification of a 2nd order infected MSO neuron (36 hpi, scale bar: 20 µm). Both dendrites are visible extending from the apical ends of the soma. The branch points of the dendrites are located ∼10-20 µm away from the soma. Two dendrites stay visible in the image, the other two exit the sectioning plane. On the left side, the axon can be seen leaving the soma. In figure 4.9 D a eGFP expressing fusiform cell located in the dorsal cochlear nucleus is displayed (left panel, scale bar: 20 µm, 63x magnification). A cutout (black square) of its prominent dendritic tree is shown in greater detail in the right panel (scale bar: 5 µm, 63x magnification, 8x zoom).

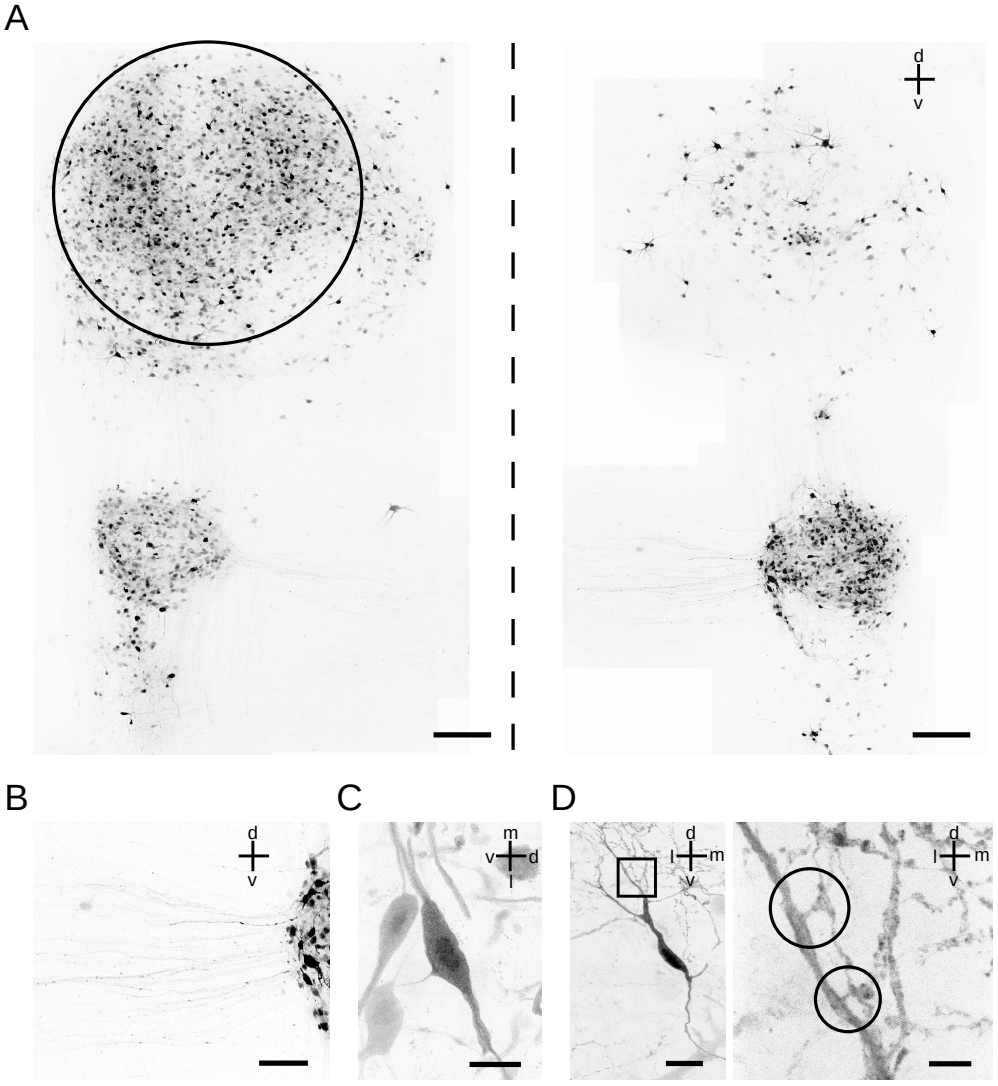

Figure 4.9: PRV-152 as a neural tracer, A eGFP expression of PRV-152 infected IC and DNLL neurons, 50 hpi. Virus was injected into the left IC (black circle). 26 confocal stacks taken with 20x magnification were stitched and then a z-projection was produced. eGFP expressing cells are seen in ipsi- and contralateral IC and DNLL. Despite the relatively small magnification several cells, especially in the IC contralateral to the injection site, are seen in great detail. Fibres are visible in the Commissure of Probst and the Lateral Lemniscus projecting from the DNLL to the IC. Scale bar 200 µm **B** Commissure of Probst from contralateral DNLL in A. Scale bar: 100 µm. **C** Z-projection an eGFP expressing neuron in the MSO after virus injection into the IC, 36 hpi. Both dendrites are clearly detectable as well as the axon leaving the neuron's soma. Scale bar: 20 µm, 63x magnification, 2x zoom. **D** Z-projection of an eGFP expressing fusiform cell in the dorsal cochlear nucleus (left panel, scale bar: 20 µm, 63x magnification, 2x zoom). The dendritic tree (black square) is shown in greater detail on the right. Black circles highlight two dendritic branches, which might be confunded with dendritic spines. Scale bar: 5 µm, 63x magnification, 8x zoom. For better visibility of fibres gray scale in all images was inverted.

In this cutout two structures (black circles) are apparent branching from the most prominent dendritic shaft. In the z-projection this two dendritic branch points may be confunded with dendritic spines, but when going through the confocal stack it becomes obvious that those structures are only dendritic branches. In general we were not able to detect spines in the proximity to the fusiform cell's soma. This coincides with early studies on the cytoarchitecture of DCN cells in mice (Browner and Baruch, 1982).

Here we showed that the eGFP expression induced by PRV-152 infection is sufficient to visualize 1st and 2nd order infected neurons in great detail. Axons and dendrites are visible without further anitbody amplification of the fluorescence. Therefore PRV-152 turns out to be an useful tool for anatomical studies in general and due to its retrograde spread analysis of neural circuits in special. The possibility to combine PRV-152 with a GFP-antibody to amplify the fluorescence or combination with PRVs expressing other fluorescent proteins like RFP (Banfield et al., 2003) may potentize its benefit.

4.5 Electrophysiology of PRV-152 infected neurons

We have shown that PRV-152 infects cells in juvenile and adult Mongolian gerbils. The infection can be initiated at different nuclei and spreads retrogradely through connected neurons. PRV-152 infection is highly neurospecific and induced eGFP expression is strong. Thus, it can be used to analyse neuronal morphology in great detail. These factors would likely allow for the proposed application of PRV-152 in the electrophysiological analysis of neural circuits (Smith et al., 2000). Therefore we analyzed the electrophysiological properties of 1st (IC, 12 hpi) and 2nd (DNLL, 36 hpi) order infected neurons.

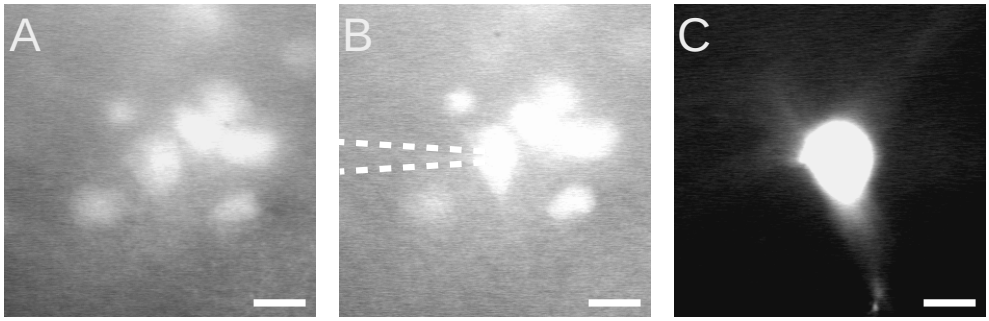

Figure 4.10: Patch-clamp in a PRV-152 infected neuron A eGFP expressing cells in the IC of a P16 gerbil, 12 hpi. **B** eGFP expressing neuron patched in on-cell mode. White dotted lines show the position of the patch-clamp electrode. **C** Image of the PRV-152 infected neuron after the recording (recordings of this neuron are shown in see fig. 4.11 A-C). All recorded cells were filled with Alexa568 hydrazide by the recording pipette to afterwards confirm their position in the IC or the DNLL. Scale bars: 20 µm, 40x magnification.

4.5.1 Electrophysiology of 1st order infected neurons

Here, we wanted to test if PRV-152 infection alters the electrophysiological properties of infected neurons. We stereotactically injected 400 µl of virus solution into the IC of P15 Mongolian gerbils. Brain slices for patch clamp recordings were obtained 12 hpi to ensure only 1st order infected neurons were recorded. Patch-clamp recordings were taken from cells with different intesities of eGFP expression. Images of recorded cells were taken before patching, during on-cell mode and after whole-cell recording when the cell was filled with Alexa568 hydrazide (see fig. 4.10). Due to the exchange of intracellular solution no double fluorescence was detectable after the recording. Therefore, the comparison of the three afore mentioned images was used to confirm that recorded cells were PRV-152 infected.

All recordings were done in current-clamp mode with no pharmacological interaction. AP thresholds were probed using stepwise increases (50-150 pA) of an 1 ms current injection (see fig. 4.11 A, same cell as in fig 4.10). To determine the firing rate currents of 500 to 1000 ms duration were injected, which were increased in steps of 50, 100 or 200 pA (see fig. 4.11 B, same cell as in A). The input resistance was

analyzed using small current injections of 5 pA with a duration of 250 to 1000 ms (see fig. 4.11 C, same cell as in A). The responses were averaged for each cell (black trace) and exponential functions were fitted to on- and offset phases (white lines) to determine the membrane time constant. Cell capacitance was then calculated on the basis of both experimentally determined values.

While all control cells recorded in the IC were excitable, in some 1st order infected cells in the IC no APs could be evoked by using the relevant test current (see fig. 4.11 D). Most of these non-excitable cells showed an atypical, not exclusively passive response pattern to current injections (see fig. 4.11 D-F, n=5). In the example recording, the AP threshold test protocol could not elicit an AP. However, higher amplitude current injections activated a conductance that prolonged the repolarisation phase (see fig. 4.11 D). The IV-curve of this example shows a small and fast onset response (see fig. 4.11 E) with an articulated kink in the rising phase (see fig. 4.11 F). This indicates that this response to longer current injections is actually an AP, although previously, using the AP-threshold tester, no APs could be induced in this cell. One of the 1st order infected non excitable cells showed a totally passive repsonse behaviour as illustrated in figure 4.13 A and B for a 2nd order infected cell.

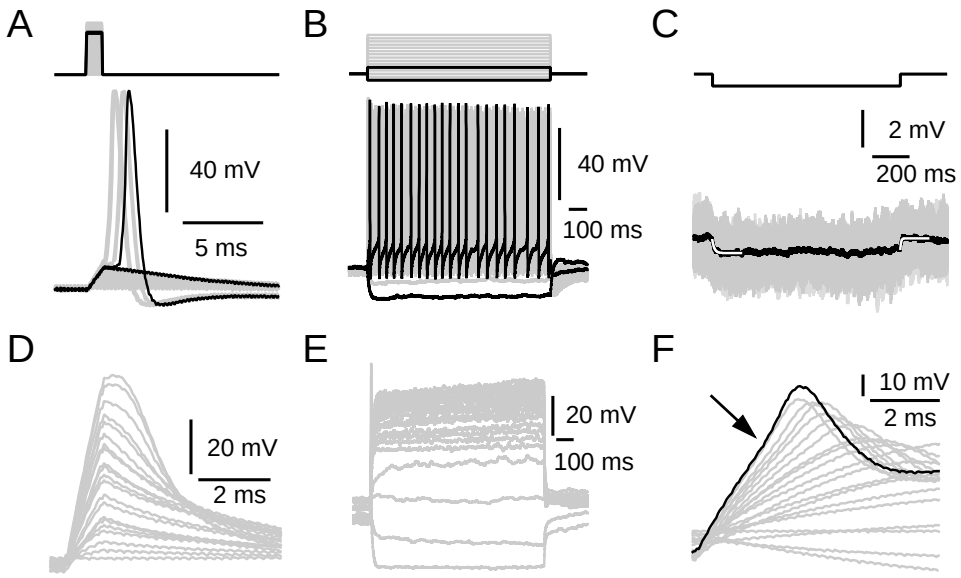

Figure 4.11: Basic membrane and firing properties in 1st order PRV-152 infected IC cells I, A AP threshold test in PRV-152 infected neurons was performed using 50-150 pA stepwise increases of a 1 ms current injection. Sub- and suprathreshold traces are depicted in black. Same cell as shown in figure 4.10 **B** Firing rate in PRV-152 infected neurons was determined by a 500-1000 ms current injection increased in steps of 50, 100 or 200 pA. First and suprathreshold traces are depicted in black. Same cell as in A **C** To determine the input resistance small current injections of 5 pA and 250-1000 ms duration were applied. Responses were averaged for each cell (black trace) and exponential functions were fitted to on- and offset phases (white lines) to determine the membrane time constant. Same cell as in A **D** AP threshold test in eGFP expressing cell which did not fire APs. **E** Current injections of 1000 ms duration lead in the same cell to an onset AP. **F** Extension of onset AP in E. Arrow marks the inflection in the upstroke, which indicates that this event is actually an AP. Slices for recordings were taken 12 hpi.

Figure 4.12 A shows that 64.71 % of infected neurons (n=17) were excitable while 35.29 % of 1st order PRV-152 infected cells in the IC responded only passively to current injections (n=1) or showed responses similar to the one depicted in figure 4.11 D-F (n=5). Non eGFP expressing IC cells in the infected brain slices were recorded as control and showed an excitability of 100 %. Care was taken to choose control cells, which were located close to infected cells. To see if there are any differences in the basic membrane properties of excitable and non-excitable 1st order infected cells both cell populations were displayed separately and compared to the control population (see fig. 4.12 B-E). The average membrane resting potential was

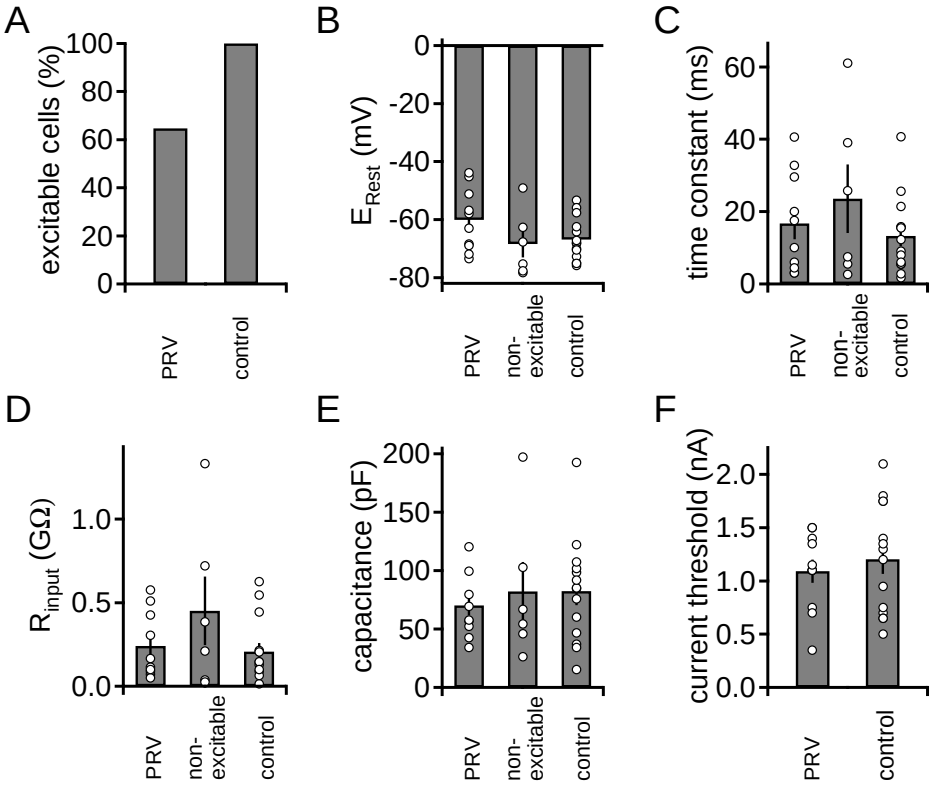

Figure 4.12: Basic membrane and firing properties in 1st order PRV-152 infected IC cells II, A Excitability in percent of 1st order infected cells (n=17). Non fluorescent neurons located close to PRV-152 infected cells were recorded as a control population (n=14). **B** Resting potential, **C** membrane time constant, **D** input resistance and **E** cell capacitance are shown for excitable infected cells (PRV, n=11), non-excitable infected cells (n=6) and control (n=14). **F** Current threshold is plotted for excitable infected cells and control. Bar graphs show average and SEM. None of the differences seen in basic membrane and firing properties (B-C) was significant ($p > 0.05$).

similar for all three cell groups. In excitable infected neurons the average membrane potential was -60.08 ± 3.43 mV (see fig. 4.12 B). It was slightly depolarized compared to non-excitable (-68.74 ± 4.61 mV) and control cells (-66.89 ± 1.95 mV). The membrane time constant showed also only minor differences between the cell populations. It was 16.71 ± 4.34 ms in excitable, 23.6 ± 9.44 ms in non-excitable and 13.24 ± 2.83 ms in control cells (see fig. 4.12 C). Cells' average input resistance ranged between 0.21 ± 0.05 GΩ for control and 0.45 ± 0.21 GΩ for non-excitable cells (see fig. 4.12 D). Negligible changes in cell capacitance (70.27 ± 8.54 pF to

82.4 ± 11.9 pF) indicated that cell size (see fig. 4.12 E) and AP threshold (see fig. 4.12 F) were also unaffected in PRV-152 infected neurons 12 hpi. None of these minor differences depicted in figure 4.12 B-F were significant ($p > 0.05$). The only significant change in infected IC cells apparent 12 hpi was the high number of non-excitable cells (35.29 %).

4.5.2 Electrophysiology of 2nd order infected neurons

We have shown that the basic membrane properties of 1st order infected neurons were unaffected. Nevertheless, 35.29 % of the infected cells which were recorded showed only an extremely reduced excitability or no excitability at all. As we determined the percentage of infected glia was only ∼12 % (see fig. 4.8), it is highly probable that at least some of the recorded non-excitable cells are neurons. In the following we repeated the previous set of experiments 36 hpi to characterize the basic membrane and firing properties of 2nd order infected neurons. Patch-clamp recordings were done in the ipsi- and contralateral DNLL to make sure that only 2nd order infected neurons were analyzed. As the number of non eGFP expressing DNLL cells in the infected brain sections was not sufficient DNLL neurons of non PRV-152 infected brain sections were also recorded and analyzed for additional control data (labelled in figure 4.13 as "no infection").

Figure 4.13 A and B shows the response of a 2nd order infected non-excitable DNLL cell. Using current injections of 1 ms duration only passive responses were evoked (see fig. 4.13 A). This response behaviour was independent of the amplitude of the current injection (here up to 2.5 nA). In no case could this passive response behaviour be changed by longer current injections (see fig. 4.13 B, duration 1000 ms, current injection up to 2 nA). This was in contrast to several 1st order infected non-excitable neurons, which responded with small APs to current injections of 1000 ms

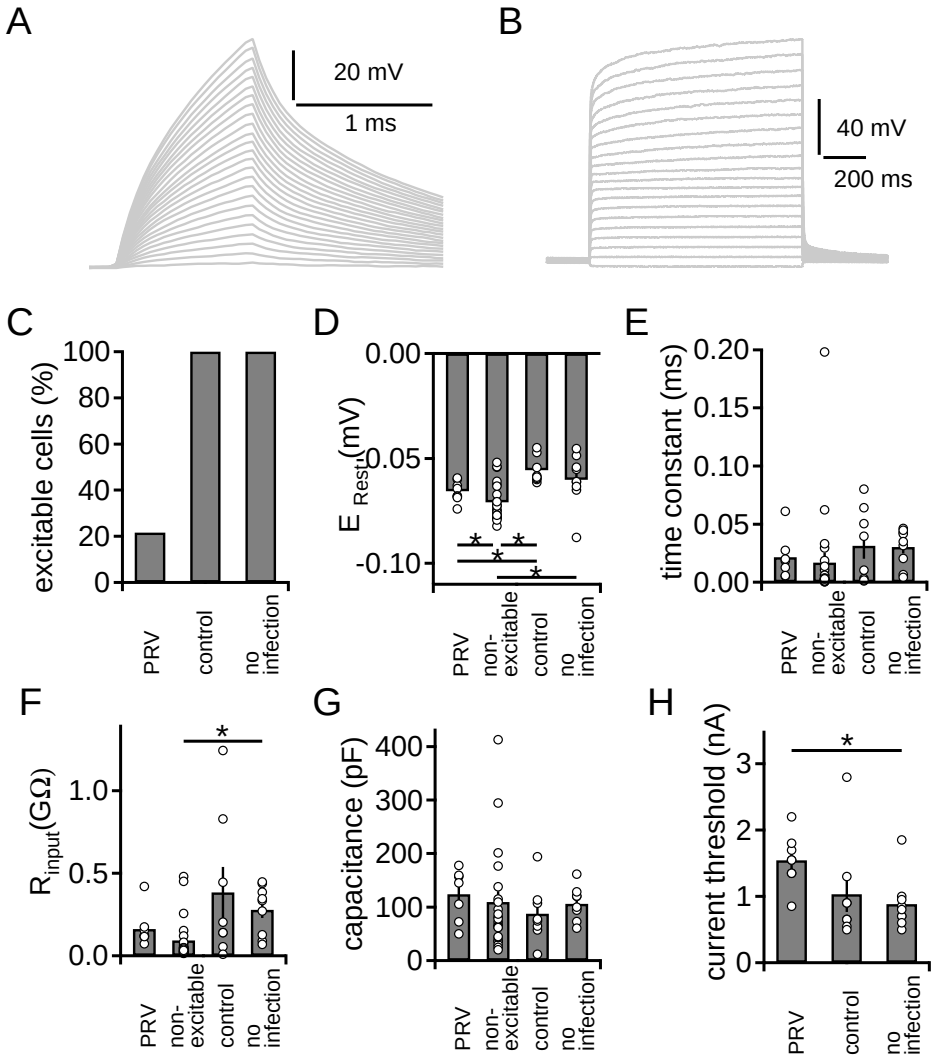

Figure 4.13: Basic membrane and firing properties in 2nd order PRV-152 infected DNLL cells, A Passive response of 2nd order infected cell to step-wise increased current injections of 1 ms duration (Step size: 100 pA, ranging from 0-2.5 nA). **B** In contrast to several 1st order infected neurons, the response remains passive even when the duration of current injections is extended to 1000 ms (Step size: 100 pA, ranging from 0-2 nA). Same cell as in A. **C** Excitability in percent of 2nd order infected cells (n=39). Non fluorescent neurons in PRV-152 infected brain sections were recorded as a control population (n=8). DNLL neurons of non PRV-152 infected brain sections were recorded as additional control (labeled as "no infection", n=9) **D** Resting potential, **E** membrane time constant, **F** input resistance and **E** cell capacitance are shown for excitable infected cells (n=8), non-excitable infected cells (n=31), control (n=8) and no infection control (n=9). **G** Current threshold is plotted for excitable infected cells, control and no infection control. Bar graphs show average and SEM.

duration. Input resistance, membrane time constant and cell capacitance were determined as previously described (see section 4.5.1).

The most obvious change in electrophysiological properties of 2nd order infected neurons is again the excitability of infected neurons (see fig. 4.13 C). Only 21.62 % percent of the recorded eGFP expressing DNLL cells (n=39) were excitable. Control cells recorded in PRV-152 infected brain sections (n=8, labelled as "control") and non infected brain sections (n=9, labelled as "no infection") show a excitability of 100 %. In the basic membrane properties some changes between cell groups are more obvious than for 1st order infected neurons. Excitable and non-excitable PRV-152 infected neurons show a slightly hyperpolarized average membrane resting potential (-65.68 ± 1.76 mV and -70.95 ± 1.78 mV, respectively) compared to both control groups (55.64 ± 2.21 mV for control and 60.19 ± 4.09 mV for no infection (see fig. 4.13 D). The difference in membrane resting potential between infected excitable, infected non excitable and control cells are significant ($p < 0.05$). Membrane resting potential of infected non-excitable cells is significantly changed compared to both control groups ($p < 0.05$). Control cells in infected and non infected brain section show an average membrane time constant of 31.26 ± 11.1 ms bzw. 30.35 ± 5.42 ms (see fig. 4.13 E). In both infected cell groups the membrane time constant is faster with 21.48 ± 7.24 mV for excitable and 16.92 ± 8.41 mV for non-excitable cells. This corresponds to an increase in the input resistance of excitable and non-excitable cells (162.49 ± 38.35 MΩ, 91.91 ± 25.92 MΩ) compared to the control in infected and non infected brain sections (383.37 ± 154.65 GΩ, 278.83 ± 49.49 GΩ, see fig. 4.13 F). The change in input resistance between infected non excitable cells and cells recorded in non infected brain sections is significant ($p < 0.05$). Cell capacitance show no significant changes between all four cell groups ranging from 87.3 ± 18.79 pF in control cells and 123.77 ± 18.35 pF in excitable infected neurons (see fig. 4.13 G). This shows that changes through the four cell populations in membrane time constant and input resistance are not caused by differences in cell

size. The AP current threshold in excitable infected neurons 1.54 ± 0.14 nA is significantly increased compared to the control group in non infected brain sections (0.88 ± 0.13 nA, $p < 0.05$, see fig. 4.13 H). Without the outlier value in the second control group (1.99 nA) difference in current threshold between infected neurons and control would also be significant.

The changes in basic membrane properties in 2nd order infected neurons are small, but more apparent than they were in 1st order infected neurons. However, stunning is the high percentage of non-excitable cells. (79.38 %) non-excitable cells cannot be explained with erroneously patched glia cells. This amount of non-firing cells rather suggests that, although basic membrane properties in infected neurons are only slightly affected, PRV-152 infection inhibit the normal firing behaviour of PRV-152 infected neurons.

We could show that PRV-152 can infect cells in juvenile and adult Mongolian gerbils. The infection is mainly neurospecific and eGFP expression in first 2nd order infected neurons is seen 26 hpi. Expression of the fluorescent protein is strong and therefore suitable for anatomical analysis. Although basic membrane properties as resting potential, membrane time constant, input resistance and cell capacitance do not show greater changes between infected and non infected cells, the change in excitability of infected neurons already apparent 12 hpi disqualifies PRV-152 as a tool for electrophysiological analysis of neural circuits in Mongolian gerbils. Thus, PRV-152 fulfills three out of four requirements for a suitable viral vector.

5 Discussion

The first part of this PhD thesis describes the excitatory IO-Fs of DNLL neurons from P15 - 17 and P48 - 60 Mongolian gerbils. Analysis of miniature EPSCs in combination with minimal fibre stimulation showed that the single average excitatory fibre released $\sim$ 18 quanta and that at least 10 excitatory fibres converge on a single DNLL neuron. A single postsynaptic AP is evoked by the simultaneous activation of 4-5 excitatory fibres. The characterized IO-Fs were strongly dependent on NMDAR currents. These NMDAR conductances amplified the EPSP summation significantly and lead to the generation of multiple APs upon a single presynaptic stimulation event. When the EPSP was mediated by AMPAR mediated currents only, it was not possible to elicit more than a single postsynaptic AP, irrespective of the synaptically transferred charge. Thus, integration of excitatory inputs in DNLL neurons depends strongly on the contribution of NMDAR mediated currents. Furthermore, the appearance of this NMDAR mediated amplification in DNLL neurons of adult animals suggests that this mechanism is of importance not only developmentally, but in an ongoing physiological context. This NMDAR dependent amplification accounts for some 25 % of the resulting extension of the time course of the DNLL's GABAergic output. Other depolarizing conductances, such as Ca^{2+} currents, did not show a similar effect on the spatial summation of EPSPs. Voltage activated potassium conductances, in contrast, clearly shortened the time window of EPSP summation in DNLL neurons. Unfortunately it was not possible

to pharmacologically identify the subfamily of potassium channels underlying this effect.

5.1 Implications for basic synaptic transmission in DNLL neurons

We characterized the basic synaptic transmission in DNLL neurons. The results from mEPSC recordings and minimal fibre stimulation lead to an estimation of $\sim$ 18 released quanta per single excitatory fibre. These data, in combination with data from anatomical studies, allows for an estimation of the number of contact sites required to provide this amount of vesicles. It was suggested that SOC fibres projecting to DNLL neurons contain several contact sites outfitted with a large synaptic bouton (Iwahori, 1986; Henkel, 1997). Fibres originating from the MSO make up to 4 large contacts onto a single DNLL neuron (Henkel, 1997). Oliver and Shneiderman (1989) showed single ultra structural sections of boutons containing two active zones. This finding suggests that a complete bouton most likely harbours more than two active zones, of which each may contain several release sites. On the basis of these estimates a total of 4 contacts per MSO fibre with each bouton containing $\sim$ 5 release sites would contain $\sim$ 20 docked vesicles, which would fit to the observed quantal content of 16 - 20 vesicles per fibre. This scenario, which does not provide for a quantal storage, would also explain the observed severe synaptic depression. Therefore, the large quantal content and the short-term plasticity profile of excitatory fibres reported here fit well with previous anatomical data.

To elicit a postsynaptic AP in juvenile DNLL neurons 72 - 90 vesicles must be released by 4-5 simultaneously activated fibres. The calculated number of fibres involved in AP generation is a lower estimate of converging fibres. Taking into account the fact that the release probability in these fibres seems to be high and synaptic

depression severe, more converging fibres would be required to counteract these two effects to enable ongoing high frequency firing in DNLL neurons (Yang and Pollak, 1994; Siveke et al., 2006). From the maximal synaptically evoked currents presented here, it is likely that a minimum of 10 fibres converges on a single DNLL neuron. Therefore excitatory synaptic integration and AP generation in DNLL neurons depends significantly on the convergence of excitatory inputs projecting to the DNLL from the MSO and/or LSO (Iwahori, 1986; Shneiderman et al., 1988; Oliver and Shneiderman, 1989; Huffman and Covey, 1995; Henkel, 1997; Siveke et al., 2006). The high convergence of excitatory fibres may have an additional physiological network function besides simply counteracting the severe synaptic depression caused by a high release probability. As this study focused only on an *in vitro* analysis of the excitatory synaptic integration to DNLL neurons, we do not know if a substantial inhibitory background activity is present *in vivo* in the DNLL network. If this is the case, an even higher number of simultaneously activated converging fibres would be required to compensate for this inhibitory activity. Aside from this compensatory effect in the DNLL network a substantial convergence of excitatory inputs could also be partially responsible for the increase in information content from the MSO to the DNLL discussed by Pecka et al. (2010).

5.2 Influence of the NMDAR mediated amplification on AP generation

The number of postsynaptically generated APs in DNLL neurons was only partially determined by the number of presynaptically applied stimulation pulses. The AP number correlated with the synaptic charge and could exceed the number of the underlying fibre shocks. The generation of additional postsynaptic APs was most obvious during higher stimulation frequencies. Logically, by generating additional

APs the activity of the postsynaptic DNLL neurons is temporally extended. This modulation of the synaptic IO-F is highly dependent on NMDAR mediated currents. When blocking those currents, the number of postsynaptic APs evoked did not outnumber the stimulation pulses applied, and was independent of the amount of the synaptically transferred charge. The injection of simulated AMPAR currents into DNLL neurons resulted in similar IO-Fs, so that more excitatory fibres have to be activated simultaneously to elicit a postsynaptic AP. Based on our analysis, when blocking the NMDA component, 126 - 144 quanta released by 7 - 8 excitatory fibres are necessary to generate an AP.

AMPA receptors are well suited to reliably transfer higher frequency signals with high temporal precision. The slow kinetics of NMDAR mediated EPSCs in contrast facilitate the integration of synaptic inputs even at low frequency transmission (for review McBain and Mayer, 1994). Therefore the NMDAR mediated current in DNLL neurons would allow for the temporal integration of single or multiple excitatory inputs firing with a short interstimulus interval. Due to the Mg^{2+} block of NMDARs higher presynaptic activity like a burst discharge or high frequency AP firing is necessary to relieve the receptor block and trigger the NMDAR mediated current (Collingridge et al., 1988). Thus, the hypothesised NMDAR dependent mechanism would become more prominent with increasing loudness of the underlying sound stimulus.

5.3 Influence of other conductances on integration in DNLL neurons

We did not observe that other depolarizing conductances such as calcium affect EPSP summation. This might be explained by the possible activation of calcium activated potassium channels, which would counteract the depolarizing calcium

effect.

Potassium in contrast did modulate the EPSP summation. When blocking potassium conductances non-specifically, EPSPs increased in width. Thus, potassium conductances sharpen the EPSP and restrict the integration time window. However, we were not able to identify the subfamily of potassium conductances responsible for this EPSP shaping. By applying 100 nM α-DTX we tested for $K_{v1.1}$, $K_{v1.2}$ and $K_{v1.6}$ conductances. 0,5 mM TEA were used to block $K_{v3.x}$ conductances (Mathie et al., 1998). Under both conditions we saw no homogeneous effect on the EPSP shape. A possible explanation would be that DNLL neurons are not homogenously equipped with potassium conductances. Indeed, it has been shown that DNLL neurons in the big brown bat strongly express $K_{v1.1}$ and in rat $K_{v3.1}$ and $K_{v3.3}$ conductances, but that not every single DNLL neuron shows positive immunohistochemical staining for those subfamilies of voltage-gated potassium channels (Rosenberger et al., 2003; Li et al., 2001).

5.4 Influence on the DNLL network

Taken together our *in vitro* study shows that the ion channel population of DNLL neurons enable the previously hypothesized integration based mechanism (Fu et al., 1997; Kelly and Kidd, 2000) and that this mechanism is highly dependent on the electrogenic signal generated by synaptically activated NMDARs. Furthermore, the existence of this NMDA dependent amplification in DNLL neurons of adult Mongolian gerbils provides strong evidence that this integration mechanism indeed influences the function of the DNLL network.

We could show further that this NMDA dependent amplification directly affects the GABAergic output of the DNLL neurons. This effect is mediated by the extension

of the postsynaptic activity of DNLL neurons through the generation of multiple postsynaptic APs upon single fibre shock events. In juvenile animals this leads to an temporal extension of the postsynaptic activity window in DNLL neurons and thereby prolongs their GABAergic output. In adult animals the NMDA component enables the DNLL neuron to maintain high firing frequencies. Thus, the NMDAR based amplification contributes to the PI generated in the DNLL.

We showed in acute brain slice experiments the existence of the integration based mechanism and its influence on the neural circuit of the DNLL. Nevertheless, in most *in vivo* experiments this integration based mechanism has proved elusive (Siveke et al., 2006; Pecka et al., 2007). Only Kelly et al. (1998) reported a multiple spike discharge upon a contralaterally presented 50 µs click in the rat DNLL and discussed its possible dependence on NMDAR mediated currents. One explanation for the lack of further observations of this phenomenon may originate in the experimental design. Many of the anaesthetics used in *in vivo* experiments affect ion conductances. Siveke et al. (2006) and Pecka et al. (2007) used a combination of ketamine and xylazine. Ketamine is a known non-competitive NMDAR antagonist (Anis et al., 1983; Harrison and Simmonds, 1985; Thomson et al., 1985; Kurumaji et al., 1989; Zeilhofer et al., 1992). Recently it was shown that ketamine significantly decreases firing rates in neurons of the superior paraolivary nucleus of the mouse (Felix et al., 2012). Indeed, recent results by Dr. Ida Siveke illustrate the modulatory effect of NMDAR mediated currents on the IO-Fs of DNLL neurons in *in vivo* experiments (personal communication). Although a ketamine based anaesthetic was used, the spiking rate in 9 out of 12 recorded DNLL neurons decreased upon the application of a specific NMDAR antagonist. Furthermore, Dr. Ida Siveke reported a broadening of ITD function in DNLL neurons when NMDAR mediated currents were blocked. It is known that ITD tuning sharpens at higher centres of the auditory system (Stanford et al., 1992; Fujita and Konishi, 1991; Fitzpatrick et al., 1997). This sharpening is thought to enhance coding accuracy and improve

the energy efficiency of ITD coding (Fitzpatrick et al., 1997; Zhang and Sejnowski, 1999). D'Angelo et al. (2005) showed a GABA mediated mechanism for sharpening ITD functions in the IC, but postulated that the GABAergic mechanism is not wholly responsible for this effect. Kuwada et al. (2006) interpreted their data as a narrowing of ITD functions in DNLL neurons and discussed the possible contribution of converging inputs from binaural nuclei like MSO and SOC to this effect. Further experiments have to show whether the observed NMDAR mediated effect could also add to an increasing narrowness of ITD functions and thereby to ITD processing in the auditory pathway.

Aside from the strong argument for the existence of the integration based mechanism (Fu et al., 1997; Kelly and Kidd, 2000) our results also provide evidence for the presence of the second hypothesized output based mechanism (Wu and Kelly, 1996; Pecka et al., 2007). This is apparent in the dependence of the time course of the GABAergic inhibition on the number of stimulation pulses. That is, although the postsynaptic activity window in the DNLL neurons was of similar duration the application of additional stimulation pulses due to a higher stimulation frequency extended the time course of the GABAergic inhibition (see fig. 3.7). In fact, this effect was seen even though the neuron's activity window was slightly shorter than during the lower frequency stimulation trial. This frequency dependence of the GABAergic output is coherent with results of previous studies (Yang and Pollak, 1998; Burger and Pollak, 2001; Pecka et al., 2007). Those *in vivo* studies showed that PI is extended by an increase of stimulus intensity and to some degree also by stimulus length.

Pecka et al. (2007) reported that they achieved a time course of PI in brain slice experiments similar to those in their *in vivo* experiments. As they stimulated the GABAergic inhibition in the commissure of Probst they argue that an output based mechanism alone would be sufficient to generate the required time course of

PI. Unfortunately, the fibre stimulation paradigm used consisted of a train stimulus which already implemented the here investigated integration based mechanism in their experimental design. Hence, the results of Pecka et al. do not exclude the contribution of the integration based mechanism to PI. Nevertheless, further work is necessary to identify and analyse in detail the underlying synaptic mechanism responsible for the output based effect (two candidates for this effect would be asynchronous release and GABA spill over) and the possible cooperation of the integration and the output based mechanism.

5.5 Conclusion I

The integration based mechanism temporally extends the activity in DNLL neurons. Subsequently, by providing an extension of the underlying activity for any output based mechanism, the GABAergic inhibition mediated by DNLL neurons is prolonged. These two serial network processes are not mutually exclusive but are perfectly suited to operate together synergistically and thereby contribute to the generation of PI in the DNLL neural network. Additional experiments are required to investigate the output based mechanism. Furthermore, a detailed characterization of the potassium conductances would be of interest. We could show in this study that potassium conductances indeed contribute to the shaping of EPSPs and thereby modulate their summation. Unfortunately, it was not possible to isolate the responsible conductances pharmacologically. Further experiments, including an analysis of the activation and inactivation of those potassium channels, are necessary to determine how these conductances modulate the integration time window in DNLL neurons.

5.6 Viral vectors as a tool for neural circuit analysis

In the second part of our study we analyzed the properties of several viral constructs to test their suitability as a tool for neural circuit analysis in the ascending auditory pathway in Mongolian gerbils. We found that the used lentiviral vectors fulfil several of the requirements necessary for a useful viral vector. However, due to low expression of the transgenic protein and the difficulty in selecting a suitable promoter their usefulness is limited. The second viral vector tested based on a Semliki Forest virus, led to a sufficient expression of the reporter gene and the general functionality of the transgenic protein. Only the strong cytotoxicity of the SFV itself inhibits the application of this viral vector for our purposes as it limits the time window for experiments and obviously induces major changes in the infected cell's properties. The eGFP expressing PRV based viral vector fulfilled nearly all of the requirements for a viral vector. It produced stable and intense expression in juvenile and adult animals. PRV infection could be started in different nuclei of the auditory brainstem, the first 2^{nd} order infected cells expressed eGFP $\sim$ 26 hpi and the vector's neurospecificity was high. Those properties turn PRV-152 into a very useful anatomical tool. Unfortunately we also observed the previously reported substantial change in the electrophysiological properties of PRV-152 infected cells (McCarthy et al., 2009). This inhibits the application of this vector for physiological analysis of neural networks in Mongolian gerbils.

5.7 Lentivirus based vectors

Lentiviruses are widely used as viral vectors as they conduct relatively high and stable expression of transgenic proteins, induce only minor changes in the infected cell's properties and are able to infect also non proliferating cells (Weinberg et al. (1991);

Ailles and Naldini (2002); Dittgen et al. (2004), for review see Trono (2000)). The first lentiviral construct tested in our study, CamKII-ChR2, did not induce GFP expression in the IC of Mongolian gerbils. Whether this malfunction was caused by a lack of infection or is due to problems with the expression of the transgenic protein can not be concluded from our data. Nevertheless, previous studies reported that CamKII-α is mainly expressed in the mammalian cortex (Burgin et al., 1990; Dittgen et al., 2004). This could indicate that in our experiments cells in the IC were infected by the lentiviral CamKII-ChR2 vector but that no expression was induced by the CamKII-α promoter.

We therefore exchanged the CamKII-α with rat synapsin I promoter, which has been reported to drive expression throughout the brain (Melloni et al., 1993). We tested three different lentiviral constructs: SynGFP, SynChR2, SynNpHR. SynGFP and SynNpHR showed intense and wide spread GFP expression around the injection site, while SynChR2 induced a somehow diminished expression of GFP. These results show that the lentiviral constructs work in Mongolian gerbils and that synapsin I can drive expression in the IC of Mongolian gerbils. Furthermore, the function of two different synapsin I controlled lentiviral constructs indicates that the malfunction of the SynChR2 construct is likely due to the SynChR2 construct itself rather than a general problem with the synapsin I controlled lentiviral constructs. A re-cloning of the SynChR2 construct may eliminate this problem.

Despite the general functionality of the synapsin I controlled lentiviral vectors and the expression of the transgenic protein in the IC of Mongolian gerbils we could show that it was not possible to induce expression in MNTB principal neurons in juvenile gerbils. Whether the infection with SynNpHR in the MNTB is restricted to glia cells only or whether also presynaptic terminals are infected could not be determined. It is also possible that MNTB principal neurons are infected but that synapsin I does not drive expression in MNTB principal neurons, similar to the

situation with the CamKII-constructs. Although former studies reported at least moderate synapsin I expression in the MNTB (Melloni et al., 1993; Sun et al., 2006), other studies indicate that synapsin I expression in the MNTB is restricted to the presynaptic terminals (Saitoh et al., 2001; Hsieh et al., 2010). However, our results show that the lentiviral vectors employed in this study are not suited for the use in Mongolian gerbils as none meet all of the requirements for an applicable viral vector.

5.8 Semliki Forest virus based vector

Due to the short expression time needed by SFV based viral vectors we also tested a SFV expressing ChR2 tagged with RFP1. This viral construct was able to infect cells in the IC and in the MNTB of juvenile Mongolian gerbils. Further, we showed that the expressed transgenic protein is functional. However, the use of SFV as a viral vector is restricted by its already previously reported high cytotoxicity (Lundstrom, 1999; Smerdou and Liljeström, 1999). In our experiments the cytotoxicity significantly shortened the time window for experiments as most infected cells deteriorated within a day after virus injection. Moreover, during the experiment SFV infected cells seemed to be more fragile than not infected cells. This indicates that infected cells are rapidly and detrimentally affected by the SFV infection, which further restricts the suitability of the SFV based viral vector. This effect was seen in both SFV infected brain areas, IC and MNTB. A minor draw back but still unfavourable is the spread of infection to glia cells. Ehrengruber et al. (2003) reported that the increase of SFV infection in glia cells is caused by high incubation temperatures. As in our experiments the viral vector was stereotactically injected *in vivo* this limitation cannot be circumvented by changing experimental settings.

An unexpected result was the difference in functionality of the expressed transgenic

protein between different cell types. In MNTB neurons, APs could not be induced by light exposure. Due to the lack of voltage clamp recordings it is difficult to say if the transgenic protein was functional or not. In the MNTB surrounds, large stellate-shaped neurons could be driven to produce APs. As in the MNTB, no APs could be evoked in the IC, but voltage clamp recordings showed the presence of ChR2 driven currents. These differences could be caused by different expression levels of the ChR2 protein between the different cell types. The single channel conductance of ChR2 is quite low at between 40 - 100 fS (Nagel et al., 2003; Feldbauer et al., 2009). This is significantly smaller than the single channel conductance of sodium channels (14 pS; Bezanilla, 1987). Thus, if the expression level of ChR2 is not high enough it might be that AP threshold is not reached even upon full activation. Another reason could be that the cells may be equipped with different conductances. If the observed large stellate-shaped neurons typically possess a high input resistance, the small currents induced by the ChR2 conductances may be able to induce an AP. MNTB cells in contrast are outfitted with fast and low voltage activated potassium conductances to enable their function as a fast and reliable inhibitory relay (Brew and Forsythe, 1995). These characteristics may lead directly to a rapid shunt of the ChR2 evoked depolarization in MNTB principal neurons.

Taken together, the high cytotoxicity alone is a severely limiting factor in the use of SFV as a viral vector. In combination with the general malfunction of ChR2 in MNTB principal neurons this viral construct fulfilled only 2-3 out of 4 necessary conditions and was therefore judged unsuitable for our purposes.

5.9 PRV based vector

PRV-152 was claimed to be a useful tool for neural circuit analysis (Smith et al., 2000; Davis et al., 2003; Glatzer et al., 2003; Gao et al., 2009; Derbenev et al., 2010).

The expression of eGFP in connected neurons in combination with the possible soundness of the infected cells and the high neurospecificity of PRV infection allows for a wide range of experimental approaches.

Previous studies showed that the wild-type PRV-Becker and the attenuated PRV-Bartha strains are capable of infecting neurons in Mongolian gerbils (Kaufman et al., 1996; Metts et al., 2006). Here we confirm that also PRV-152, the eGFP expressing PRV-Bartha based vector infects neurons in juvenile and adult Mongolian gerbils after stereotactic injection into different brain areas. The highly reproducible fluorescence patterns obtained during our experiments suggest that the infection spreads through functionally connected neurons as was reported previously (Card et al., 1990, 1993; Rinaman et al., 2000). Furthermore, the fluorescence pattern indicates that PRV-152 infection is spread only retrogradely as could be expected for a PRV-Bartha based viral vector (Brittle et al., 2004; Smeraski et al., 2004).

The time course of infection in Mongolian gerbils is relatively stable, resulting in first 2^{nd} order eGFP expressing cells $\sim$ 26 hpi. Taking into account the 4-6 hours necessary for the biosynthesis of eGFP the synaptic spread happened $\sim$ 20 hpi (Heim et al., 1994; Vordermark et al., 2001). This time course seems to be similar in both juvenile and adult animals. The fact that the number of 2^{nd} order infected neurons continues to increase over time gives rise to the assumption that the synaptic spread happens over a certain time span rather than at a defined time point. This is coherent with results from studies saying that the speed of the neuronal spread depends on the distance the virus particles have to cross (Lycke et al., 1984; Bearer et al., 2000). Single eGFP expressing cells in the ipsilateral MNTB and the contralateral MSO in brain sections obtained 50 hpi indicate that at this time first 3^{rd} order neurons may be infected. However, this conclusion is difficult to interpret as this holds true only if the initial virus infection was restricted to the center of the IC (Adams, 1979; Spangler et al., 1985; Coleman and Clerici, 1987;

Kelly et al., 2009).

The immunohistochemical staining showed that PRV infection in the Mongolian gerbil is mostly neurospecific. Only around 10% of infected cells were identified as glia cells emphasising the highly neurotropic properties of PRV (Rinaman et al., 1993; Card et al., 1993). Furthermore, this rate of glia infection was expected from our use of the CMV promoter, which is known to drive expression of this magnitude in glia cells (Blömer et al., 1997). Interestingly, there is a difference in infected glia and overall infection rate between different auditory nuclei. In the IC at the injection site, infection rate is high compared to the other infected nuclei. This higher infection rate can be explained by the existence of interneurons or at least collateral axons by which IC neurons contribute to local circuits (Morest, 1966; Sukhovskaya, 1966; Rockel and Jones, 1973; Oliver et al., 1994). Due to these connections there are 1st and 2nd order PRV infected neurons present at the injection site. At the level of the DNLL the quantitative analysis shows that no significant difference in infection rate is apparent between the ipsi- and contralateral DNLL. This contradicts the impression obtained from the first PRV-152 infected brain sections (50 hpi; see fig. 4.3), which suggests that the contralateral DNLL shows a higher rate of infection than the DNLL ipsilateral to the injection site. This impression was probably created by an asymmetric section plane. We cannot confirm findings of previous studies, which reported that the ICs receive more projections from the contralateral DNLLs (Merchán et al., 1994; Kelly et al., 2009). However, the accuracy of stereotactic injection in our experiments and even more the course of virus infection itself were variable so that the data we collected is far from strong enough to doubt or contradict published findings.

The high expression level of eGFP induced by PRV-152 infection allows for the detailed visualization of the fine structure of infected cells. Single projections in the commissure of Probst were clearly distinguishable and single axons were de-

tectable. The fluorescence was intense enough to allow for the visualisation of even fine structures on the dendritic tree of fusiform cells in the CN without immunohistochemical amplification of fluorescence. Thus, immunohistochemical staining with eGFP antibody could be used to further amplify the fluorescence. This measure would probably further enhance the visibility of details in PRV-152 infected cells.

Taken together, PRV-152 is a promising tool for neural circuit analysis. The crossing to functionally connected neurons, the stable time course of neural spread and the high neurotropism make PRV-152 into a suitable tool for anatomical analysis. The high expression rate of the virus increases its usefulness. The details in fine structures such as neurites from fibres and axon collaterals seen in PRV-152 infected neurons without further amplification of fluorescence is stunning.

It was reported that PRV-152 infection does not affect the electrophysiological properties of *in vitro* and *in vivo* infected neurons of hamsters and rats (Smith et al., 2000; Davis et al., 2003; Glatzer et al., 2003; Gao et al., 2009; Derbenev et al., 2010). However, data from a recent *in vitro* study in dissociated rat superior cervical ganglia cells showed alterations in the infected cell's electrophysiological properties (McCarthy et al., 2009). We therefore tested the electrophysiological properties of 1st and 2nd order PRV-152 infected neurons after *in vivo* injection in Mongolian gerbils.

1st order infected neurons did not show any significant changes in their basic electrophysiological properties such as membrane resting potential, membrane time constant, input resistance or current threshold for AP generation. Nevertheless, 37% of PRV-152 infected neurons showed a deficit in excitability. At least 6 of these non excitable cells were verifiably neurons as they showed AP like waveforms when longer current injections were applied. In 2nd order infected neurons changes in basic electrophysiological properties such as membrane resting potential, input resistance and current threshold were slightly more pronounced. But even here the

extent of alteration only became apparent when the excitability of infected neurons was tested. 78% of eGFP expressing 2nd order infected neurons did not show any sign of excitability 36 hpi. Immunohistochemical staining of acute brain slices after patching were not successful, so that none of these non-excitable cells could be unambiguously identified as either neuron or glia. However, the high number of non-excitable cells cannot be explained by mistakenly patched glia cells, as the ratio of infected glia was only around 10%. It may be that the relatively unchanged basic electrophysiological properties of PRV-152 infected cells did prevent the detection of alterations in electrophysiology of PRV-152 infected neurons in previous *in vivo* studies (Smith et al., 2000; Gao et al., 2009; Derbenev et al., 2010). McCarthy et al. (2009) also suggested that the lack of observed electrophsiological changes in the previous studies might originate in the difficulty to specify the time point of infection in *in vivo* studies. Electrophysiological changes occur late in PRV-152 infected cells and recordings might have been performed in recently infected neurons only. It could also be possible that the alteration of electrophysiological properties of PRV-152 infected neurons is different between infected species. This would explain why in Mongolian gerbils no hyperexcitability in PRV-152 infected neurons was observed, but a lack of excitability. Thus, the results obtained here may only be of significance to PRV-152 infected Mongolian gerbils.

In our study we showed the properties and utility of PRV-152 as a transneuronal tracer in Mongolian gerbils especially for use in anatomical studies. The combination with PRV-Bartha virus strains expressing other fluorescent proteins like PRV-614 (Banfield et al., 2003) would allow for the anatomical analysis of parallel neural circuits. An example for such an experiment would be the injection of PRV-152 into the IC and PRV-614 into the superior colliculus in Mongolian gerbils. PRV-152 would retrogradely label the neurons of the ascending auditory pathway containing the nuclei of the lateral lemniscus, SOC and the CN. PRV-614 would mark the nuclei of the central acoustic tract down to the CN. Double la-

belled neurons would indicate the nuclei where both neural circuits diverge. This experimental design could allow for the anatomical investigation of the nucleus of the central acoustic tract in Mongolian gerbils (Casseday et al., 1989). Beside its possibilities in anatomical studies the use of PRV as a tool for physiological neural network analysis in Mongolian gerbils, however, is largely restricted as excitability of infected neurons is significantly decreased. It is yet to be seen if this restriction must be extended to other species.

5.10 Conclusion II

Altogether, none of the tested viral vectors was fully suited for the planned experimental strategies for neural network analysis as none fulfilled the previously defined requirements. PRV-152 fulfilled most of the desired characteristics (3/4), but induced severe changes in the physiology of the infected neurons. A viral vector which does not affect the electrophysiology of infected neurons, would allow for the investigation of synaptic integration of different inputs to the same neuron in strongly converging neural networks. Vectors expressing different fluorescent proteins could be stereotactically injected into several nuclei (DNLL,MSO and LSO) projecting to the same neurons in a different nucleus (IC). The inputs from different nuclei now labelled with different fluorescent proteins could be visually distinguished. Fibre stimulation experiments could then be used to isolate and analyse the integration of different inputs to the same neuron. The expression of ChR2 and NpHR with those vectors would simplify the experiment as electrical fibre stimulation could be substituted by light exposure (Petreanu et al., 2007; Cruikshank et al., 2010). Additionally this would allow the application of this experimental design *in vivo*.

A lentivirus, with a promoter suitable for nuclei of the auditory brainstem remains one of the must promising possibilities for this experimental paradigm. One can-

didate for such a promoter would be the CMV promoter used in the PRV-152 construct as we have already shown that this promoter can drive expression in all nuclei of interest to us. This promoter could also be combined with adeno associated viruses (AAVs), which have similar properties to lentiviruses but induce an even smaller immunological response in infected cells (Zaiss et al., 2002; for review Jooss and Chirmule, 2003). AAVs are also interesting viral vectors as it was shown that the tropism of AAVs to excitatory and inhibitory cortical neurons can be modulated by the viral titer (Nathanson et al., 2009). In combination with the ongoing investigation on promoters specific to only a subpopulation of neurons the expression of transgenic proteins could be restricted to small groups of neurons allowing for more and more sophisticated experimental designs. Boëda et al. (2001) for example characterised a promoter specific to inner hair cells. Promoters driving expression specifically in inhibitory neurons have also been identified (Nathanson et al., 2009) and recently it was shown that the combination of a CMV promoter with a synthetic promoter can improve the efficiency of expression (Jianwei et al., 2011).

No matter which combination of virus and promoter is chosen, it is very probable that the resulting virus will not fit every single experimental approach. A more promising strategy is the development of a toolbox of different viruses, from which the most fitting could be selected for specific experimental strategies. Even then such new approaches cannot be a full substitute for traditional electrophysiological methods. It is much more likely that the combination of old and new approaches will give the best results in neural circuit analysis.

Bibliography

Adams JC (1979) Ascending projections to the inferior colliculus. *J Comp Neurol* 183:519–538.

Adams JC, Mugnaini E (1984) Dorsal nucleus of the lateral lemniscus: a nucleus of gabaergic projection neurons. *Brain Res Bull* 13:585–590.

Ailles LE, Naldini L (2002) Hiv-1-derived lentiviral vectors. *Curr Top Microbiol Immunol* 261:31–52.

Anis NA, Berry SC, Burton NR, Lodge D (1983) The dissociative anaesthetics, ketamine and phencyclidine, selectively reduce excitation of central mammalian neurones by n-methyl-aspartate. *Br J Pharmacol* 79:565–575.

Aston-Jones G, Card JP (2000) Use of pseudorabies virus to delineate multisynaptic circuits in brain: opportunities and limitations. *J Neurosci Methods* 103:51–61.

Atkins GJ, Sheahan BJ, Mooney DA (1990) Pathogenicity of semliki forest virus for the rat central nervous system and primary rat neural cell cultures: possible implications for the pathogenesis of multiple sclerosis. *Neuropathol Appl Neurobiol* 16:57–68.

Aujeszky A (1902) Über eine neue infektionskrankheit bei haustieren. *Zentralbl Bakteriol* 32:Seiten 353–357.

Bajo VM, Villa AE, de Ribaupierre F, Rouiller EM (1998) Discharge properties of single neurons in the dorsal nucleus of the lateral lemniscus of the rat. *Brain Res Bull* 47:595–610.

Banfield BW, Yap GS, Knapp AC, Enquist LW (1998) A chicken embryo eye model for the analysis of alphaherpesvirus neuronal spread and virulence. *J Virol* 72:4580–4588.

Banfield BW, Kaufman JD, Randall JA, Pickard GE (2003) Development of pseudorabies virus strains expressing red fluorescent proteins: new tools for multisynaptic labeling applications. *J Virol* 77:10106–10112.

Bearer EL, Breakefield XO, Schuback D, Reese TS, LaVail JH (2000) Retrograde axonal transport of herpes simplex virus: evidence for a single mechanism and a role for tegument. *Proc Natl Acad Sci U S A* 97:8146–8150.

Bezanilla F (1987) Single sodium channels from the squid giant axon. *Biophys J* 52:1087–1090.

Blauert J (1997) *Spatial hearing: The psychopysics of human sound localization* Cambridge MA: MIT Press.

Blömer U, Naldini L, Kafri T, Trono D, Verma IM, Gage FH (1997) Highly efficient and sustained gene transfer in adult neurons with a lentivirus vector. *J Virol* 71:6641–6649.

Boëda B, Weil D, Petit C (2001) A specific promoter of the sensory cells of the inner ear defined by transgenesis. *Hum Mol Genet* 10:1581–1589.

Bokhoven M, Stephen SL, Knight S, Gevers EF, Robinson IC, Takeuchi Y, Collins MK (2009) Insertional gene activation by lentiviral and gammaretroviral vectors. *J Virol* 83:283–294.

Boyden ES, Zhang F, Bamberg E, Nagel G, Deisseroth K (2005) Millisecond-timescale, genetically targeted optical control of neural activity. *Nat Neurosci* 8:1263–1268.

Bradish CJ, Allner K, Maber HB (1971) The virulence of original and derived strains of semliki forest virus for mice, guinea-pigs and rabbits. *J Gen Virol* 12:141–160.

Brand A, Behrend O, Marquardt T, McAlpine D, Grothe B (2002) Precise inhibition is essential for microsecond interaural time difference coding. *Nature* 417:543–547.

Brew HM, Forsythe ID (1995) Two voltage-dependent k+ conductances with complementary functions in postsynaptic integration at a central auditory synapse. *J Neurosci* 15:8011–8022.

Brittle EE, Reynolds AE, Enquist LW (2004) Two modes of pseudorabies virus neuroinvasion and lethality in mice. *J Virol* 78:12951–12963.

Browner RH, Baruch A (1982) The cytoarchitecture of the dorsal cochlear nucleus in the 3-month- and 26-month-old c57bl/6 mouse: a golgi impregnation study. *J Comp Neurol* 211:115–138.

Brugge JF, Anderson DJ, Aitkin LM (1970) Responses of neurons in the dorsal nucleus of the lateral lemniscus of cat to binaural tonal stimulation. *J Neurophysiol* 33:441–458.

Brungart DS, Rabinowitz WM (1999) Auditory localization of nearby sources. head-related transfer functions. *J Acoust Soc Am* 106:1465–1479.

Brunso-Bechtold JK, Thompson GC, Masterton RB (1981) Hrp study of the organization of auditory afferents ascending to central nucleus of inferior colliculus in cat. *J Comp Neurol* 197:705–722.

Burger RM, Pollak GD (2001) Reversible inactivation of the dorsal nucleus of the lateral lemniscus reveals its role in the processing of multiple sound sources in the inferior colliculus of bats. *J Neurosci* 21:4830–4843.

Burgin KE, Waxham MN, Rickling S, Westgate SA, Mobley WC, Kelly PT (1990) In situ hybridization histochemistry of ca2+/calmodulin-dependent protein kinase in developing rat brain. *J Neurosci* 10:1788–1798.

Campeau E, Ruhl VE, Rodier F, Smith CL, Rahmberg BL, Fuss JO, Campisi J, Yaswen P, Cooper PK, Kaufman PD (2009) A versatile viral system for expression and depletion of proteins in mammalian cells. *PLoS One* 4:e6529.

Cant NB, Casseday JH (1986) Projections from the anteroventral cochlear nucleus to the lateral and medial superior olivary nuclei. *J Comp Neurol* 247:457–476.

Cant NB, Hyson RL (1992) Projections from the lateral nucleus of the trapezoid body to the medial superior olivary nucleus in the gerbil. *Hear Res* 58:26–34.

Card JP, Levitt P, Enquist LW (1998) Different patterns of neuronal infection after intracerebral injection of two strains of pseudorabies virus. *J Virol* 72:4434–4441.

Card JP, Rinaman L, Lynn RB, Lee BH, Meade RP, Miselis RR, Enquist LW (1993) Pseudorabies virus infection of the rat central nervous system: ultrastructural characterization of viral replication, transport, and pathogenesis. *J Neurosci* 13:2515–2539.

Card JP, Rinaman L, Schwaber JS, Miselis RR, Whealy ME, Robbins AK, Enquist LW (1990) Neurotropic properties of pseudorabies virus: uptake and transneuronal passage in the rat central nervous system. *J Neurosci* 10:1974–1994.

Carr CE, Konishi M (1990) A circuit for detection of interaural time differences in the brain stem of the barn owl. *J Neurosci* 10:3227–3246.

Casseday JH, Kobler JB, Isbey SF, Covey E (1989) Central acoustic tract in an echolocating bat: an extralemniscal auditory pathway to the thalamus. *J Comp Neurol* 287:247–259.

Cazzin C, Piccoli L, Massagrande M, Garbati N, Michielin F, Knaus HG, Ring CJA, Morrison AD, Merlo-Pich E, Rovo Z, Astori S, Lüthi A, Corti C, Corsi M (2011) rkv1.2 overexpression in the central medial thalamic area decreases caffeine-induced arousal. *Genes Brain Behav* .

Chanda S, Xu-Friedman MA (2010) Neuromodulation by gaba converts a relay into a coincidence detector. *J Neurophysiol* 104:2063–2074.

Clark GM (1969) The ultrastructure of nerve endings in the medial superior olive of the cat. *Brain Res* 14:293–305.

Clifton RK (1987) Breakdown of echo suppression in the precedence effect. *J Acoust Soc Am* 82:1834–1835.

Coleman JR, Clerici WJ (1987) Sources of projections to subdivisions of the inferior colliculus in the rat. *J Comp Neurol* 262:215–226.

Collingridge GL, Herron CE, Lester RA (1988) Frequency-dependent n-methyl-d-aspartate receptor-mediated synaptic transmission in rat hippocampus. *J Physiol* 399:301–312.

Couchman K (2011) Receptors and Synapses in the MSO Ph.D. diss., Graduate School of Systemic Neurosciences of Ludwig-Maximilians-Universität München.

Couchman K, Grothe B, Felmy F (2010) Medial superior olivary neurons receive surprisingly few excitatory and inhibitory inputs with balanced strength and short-term dynamics. *J Neurosci* 30:17111–17121.

Covey E (1993) Response properties of single units in the dorsal nucleus of the lateral lemniscus and paralemniscal zone of an echolocating bat. *J Neurophysiol* 69:842–859.

Cruikshank SJ, Urabe H, Nurmikko AV, Connors BW (2010) Pathway-specific feedforward circuits between thalamus and neocortex revealed by selective optical stimulation of axons. *Neuron* 65:230–245.

D'Angelo WR, Sterbing SJ, Ostapoff EM, Kuwada S (2005) Role of gabaergic inhibition in the coding of interaural time differences of low-frequency sounds in the inferior colliculus. *J Neurophysiol* 93:3390–3400.

Davis SF, Williams KW, Xu W, Glatzer NR, Smith BN (2003) Selective enhancement of synaptic inhibition by hypocretin (orexin) in rat vagal motor neurons: implications for autonomic regulation. *J Neurosci* 23:3844–3854.

Derbenev AV, Duale H, Rabchevsky AG, Smith BN (2010) Electrophysiological characteristics of identified kidney-related neurons in adult rat spinal cord slices. *Neurosci Lett* 474:168–172.

DiCiommo DP, Bremner R (1998) Rapid, high level protein production using dna-based semliki forest virus vectors. *J Biol Chem* 273:18060–18066.

Dittgen T, Nimmerjahn A, Komai S, Licznerski P, Waters J, Margrie TW, Helmchen F, Denk W, Brecht M, Osten P (2004) Lentivirus-based genetic manipulations of cortical neurons and their optical and electrophysiological monitoring in vivo. *Proc Natl Acad Sci U S A* 101:18206–18211.

Dolivo M, Beretta E, Bonifas V, Foroglou C (1978) Ultrastructure and function in sympathetic ganglia isolated from rats infected with pseudorabies virus. *Brain Res* 140:111–123.

Ehrengruber MU, Hennou S, Büeler H, Naim HY, Déglon N, Lundstrom K (2001) Gene transfer into neurons from hippocampal slices: comparison of recombinant semliki forest virus, adenovirus, adeno-associated virus, lentivirus, and measles virus. *Mol Cell Neurosci* 17:855–871.

Ehrengruber MU (2002) Alphaviral vectors for gene transfer into neurons. *Mol Neurobiol* 26:183–201.

Ehrengruber MU, Renggli M, Raineteau O, Hennou S, Vähä-Koskela MJV, Hinkkanen AE, Lundstrom K (2003) Semliki forest virus a7(74) transduces hippocampal neurons and glial cells in a temperature-dependent dual manner. *J Neurovirol* 9:16–28.

Ekstrand MI, Enquist LW, Pomeranz LE (2008) The alpha-herpesviruses: molecular pathfinders in nervous system circuits. *Trends Mol Med* 14:134–140.

Enquist LW (1999) Life beyond eradication: veterinary viruses in basic science. *Arch Virol Suppl* 15:87–109.

Enquist LW (2002) Exploiting circuit-specific spread of pseudorabies virus in the central nervous system: insights to pathogenesis and circuit tracers. *J Infect Dis* 186 Suppl 2:S209–S214.

Feldbauer K, Zimmermann D, Pintschovius V, Spitz J, Bamann C, Bamberg E (2009) Channelrhodopsin-2 is a leaky proton pump. *Proc Natl Acad Sci U S A* 106:12317–12322.

Felix RA, Kadner A, Berrebi AS (2012) Effects of ketamine on response properties of neurons in the superior paraolivary nucleus of the mouse. *Neuroscience* 201:307–319.

Field HJ, Hill TJ (1974) The pathogenesis of pseudorabies in mice following peripheral inoculation. *J Gen Virol* 23:145–157.

Fitzpatrick DC, Batra R, Stanford TR, Kuwada S (1997) A neuronal population code for sound localization. *Nature* 388:871–874.

Fitzpatrick DC, Kuwada S (2001) Tuning to interaural time differences across frequency. *J Neurosci* 21:4844–4851.

Fitzpatrick DC, Kuwada S, Batra R (2000) Neural sensitivity to interaural time differences: beyond the jeffress model. *J Neurosci* 20:1605–1615.

Forsythe ID (1994) Direct patch recording from identified presynaptic terminals mediating glutamatergic epscs in the rat cns, in vitro. *J Physiol* 479 (Pt 3):381–387.

Forsythe ID, Westbrook GL (1988) Slow excitatory postsynaptic currents mediated by n-methyl-d-aspartate receptors on cultured mouse central neurones. *J Physiol* 396:515–533.

Fragkoudis R, Tamberg N, Siu R, Kiiver K, Kohl A, Merits A, Fazakerley JK (2009) Neurons and oligodendrocytes in the mouse brain differ in their ability to replicate semliki forest virus. *J Neurovirol* 15:57–70.

Fu XW, Brezden BL, Kelly JB, Wu SH (1997) Synaptic excitation in the dorsal nucleus of the lateral lemniscus: whole-cell patch-clamp recordings from rat brain slice. *Neuroscience* 78:815–827.

Fujita I, Konishi M (1991) The role of gabaergic inhibition in processing of interaural time difference in the owl's auditory system. *J Neurosci* 11:722–739.

Galambos R, Davis H (1943) The repsonse of single auditory-nerve fibres to acoustic stimulation. *J Neurophysiol* 6:39–57.

Gao H, Glatzer NR, Williams KW, Derbenev AV, Liu D, Smith BN (2009) Morphological and electrophysiological features of motor neurons and putative interneurons in the dorsal vagal complex of rats and mice. *Brain Res* 1291:40–52.

Glasgow GM, McGee MM, Sheahan BJ, Atkins GJ (1997) Death mechanisms in cultured cells infected by semliki forest virus. *J Gen Virol* 78 (Pt 7):1559–1563.

Glatzer NR, Hasney CP, Bhaskaran MD, Smith BN (2003) Synaptic and morphologic properties in vitro of premotor rat nucleus tractus solitarius neurons labeled transneuronally from the stomach. *J Comp Neurol* 464:525–539.

Glendenning KK, Brunso-Bechtold JK, Thompson GC, Masterton RB (1981) Ascending auditory afferents to the nuclei of the lateral lemniscus. *J Comp Neurol* 197:673–703.

Goldberg JM, Brown PB (1969) Response of binaural neurons of dog superior olivary complex to dichotic tonal stimuli: some physiological mechanisms of sound localization. *J Neurophysiol* 32:613–636.

Griffin DE (1998) A review of alphavirus replication in neurons. *Neurosci Biobehav Rev* 22:721–723.

Griffin DE (2001) *Alphaviruses. In: Fields virology* Lippincott Williams & Wilkins.

Griffin DR, Galambos R (1941) The sensory basis of obstacle avoidance by flying bats. *J Exp Zool* 86, 3:481–506.

Griffin SJ, Bernstein LR, Ingham NJ, McAlpine D (2005) Neural sensitivity to interaural envelope delays in the inferior colliculus of the guinea pig. *J Neurophysiol* 93:3463–3478.

Grothe B, Sanes DH (1993) Bilateral inhibition by glycinergic afferents in the medial superior olive. *J Neurophysiol* 69:1192–1196.

Grothe B (2003) New roles for synaptic inhibition in sound localization. *Nat Rev Neurosci* 4:540–550.

Grothe B, Pecka M, McAlpine D (2010) Mechanisms of sound localization in mammals. *Physiol Rev* 90:983–1012.

Gruber CM, Ellis FW, Freedman G (1944) A toxicological and pharmacological investigation of sodium sec-butyl ethyl barbituric acid (butisol sodium). *JPET* 81:254–268.

Hacein-Bey-Abina S, Kalle CV, Schmidt M, McCormack MP, Wulffraat N, Leboulch P, Lim A, Osborne CS, Pawliuk R, Morillon E, Sorensen R, Forster A, Fraser P, Cohen JI, de Saint Basile G, Alexander I, Wintergerst U, Frebourg T, Aurias A, Stoppa-Lyonnet D, Romana S, Radford-Weiss I, Gross F, Valensi F, Delabesse E, Macintyre E, Sigaux F, Soulier J, Leiva LE, Wissler M, Prinz C, Rabbitts TH, Deist FL, Fischer A, Cavazzana-Calvo M (2003) Lmo2-associated clonal t cell proliferation in two patients after gene therapy for scid-x1. *Science* 302:415–419.

Harrison NL, Simmonds MA (1985) Quantitative studies on some antagonists of n-methyl d-aspartate in slices of rat cerebral cortex. *Br J Pharmacol* 84:381–391.

Heffner R, Heffner H (1980) Hearing in the elephant (elephas maximus). *Science* 208:518–520.

Heffner RS, Heffner HE (1988) Sound localization and use of binaural cues by the gerbil (meriones unguiculatus). *Behav Neurosci* 102:422–428.

Heffner RS, Heffner HE (1989) Sound localization, use of binaural cues and the superior olivary complex in pigs. *Brain Behav Evol* 33:248–258.

Heim R, Prasher DC, Tsien RY (1994) Wavelength mutations and posttranslational autoxidation of green fluorescent protein. *Proc Natl Acad Sci U S A* 91:12501–12504.

Held H (1893) Die centrale gehörleitung. *Archiv f. Anat. u. Physiol. anat. Abt.* 17:201–248.

Henkel CK (1997) Axonal morphology in fibrodendritic laminae of the dorsal nucleus of the lateral lemniscus: afferent projections from the medial superior olivary nucleus. *J Comp Neurol* 380:136–144.

Hirtz JJ, Boesen M, Braun N, Deitmer JW, Kramer F, Lohr C, Müller B, Nothwang HG, Striessnig J, Löhrke S, Friauf E (2011) Cav1.3 calcium channels are required for normal development of the auditory brainstem. *J Neurosci* 31:8280–8294.

Hong S, Hwang DY, Yoon S, Isacson O, Ramezani A, Hawley RG, Kim KS (2007) Functional analysis of various promoters in lentiviral vectors at different stages of in vitro differentiation of mouse embryonic stem cells. *Mol Ther* 15:1630–1639.

Hsieh CY, Nakamura PA, Luk SO, Miko IJ, Henkemeyer M, Cramer KS (2010) Ephrin-b reverse signaling is required for formation of strictly contralateral auditory brainstem pathways. *J Neurosci* 30:9840–9849.

Huffman RF, Covey E (1995) Origin of ascending projections to the nuclei of the lateral lemniscus in the big brown bat, eptesicus fuscus. *J Comp Neurol* 357:532–545.

Iwahori N (1986) A golgi study on the dorsal nucleus of the lateral lemniscus in the mouse. *Neurosci Res* 3:196–212.

Jeffress LA (1948) A place theory of sound localization. *J Comp Physiol Psychol* 41:35–39.

Jianwei D, Qianqian Z, Songcai L, Mingjun Z, Xiaohui R, Linlin H, Qingyan J, Yongliang Z (2011) The combination of a synthetic promoter and a cmv promoter improves foreign gene expression efficiency in myocytes. *J Biotechnol* .

Jooss K, Chirmule N (2003) Immunity to adenovirus and adeno-associated viral vectors: implications for gene therapy. *Gene Ther* 10:955–963.

Joris PX, Yin TC (1995) Envelope coding in the lateral superior olive. i. sensitivity to interaural time differences. *J Neurophysiol* 73:1043–1062.

Joseph AW, Hyson RL (1993) Coincidence detection by binaural neurons in the chick brain stem. *J Neurophysiol* 69:1197–1211.

Kapfer C, Seidl AH, Schweizer H, Grothe B (2002) Experience-dependent refinement of inhibitory inputs to auditory coincidence-detector neurons. *Nat Neurosci* 5:247–253.

Kaufman GD, Mustari MJ, Miselis RR, Perachio AA (1996) Transneuronal pathways to the vestibulocerebellum. *J Comp Neurol* 370:501–523.

Köbbert C, Apps R, Bechmann I, Lanciego JL, Mey J, Thanos S (2000) Current concepts in neuroanatomical tracing. *Prog Neurobiol* 62:327–351.

Kelly JB, Buckthought AD, Kidd SA (1998) Monaural and binaural response properties of single neurons in the rat's dorsal nucleus of the lateral lemniscus. *Hear Res* 122:25–40.

Kelly JB, Kidd SA (2000) Nmda and ampa receptors in the dorsal nucleus of the lateral lemniscus shape binaural responses in rat inferior colliculus. *J Neurophysiol* 83:1403–1414.

Kelly JB, van Adel BA, Ito M (2009) Anatomical projections of the nuclei of the lateral lemniscus in the albino rat (rattus norvegicus). *J Comp Neurol* 512:573–593.

Khimich D, Nouvian R, Pujol R, Dieck ST, Egner A, Gundelfinger ED, Moser T (2005) Hair cell synaptic ribbons are essential for synchronous auditory signalling. *Nature* 434:889–894.

Kiang NY, Watanabe T, Thomas C, Clark LF (1965) Discharge patterns of single fibres in the cat's auditory nerve. *MIT Press* .

Kimman TG, Binkhorst GJ, van den Ingh TS, Pol JM, Gielkens AL, Roelvink ME (1991) Aujeszky's disease in horses fulfils koch's postulates. *Vet Rec* 128:103–106.

Kootstra NA, Verma IM (2003) Gene therapy with viral vectors. *Annu Rev Pharmacol Toxicol* 43:413–439.

Kääriäinen L, Takkinen K, Keränen S, Söderlund H (1987) Replication of the genome of alphaviruses. *J Cell Sci Suppl* 7:231–250.

Kurumaji A, Nehls DG, Park CK, McCulloch J (1989) Effects of nmda antagonists, mk-801 and cpp, upon local cerebral glucose use. *Brain Res* 496:268–284.

Kuwabara N, DiCaprio RA, Zook JM (1991) Afferents to the medial nucleus of the trapezoid body and their collateral projections. *J Comp Neurol* 314:684–706.

Kuwada S, Fitzpatrick DC, Batra R, Ostapoff EM (2006) Sensitivity to interaural time differences in the dorsal nucleus of the lateral lemniscus of the unanesthetized rabbit: comparison with other structures. *J Neurophysiol* 95:1309–1322.

Lewis P, Hensel M, Emerman M (1992) Human immunodeficiency virus infection of cells arrested in the cell cycle. *EMBO J* 11:3053–3058.

Li W, Kaczmarek LK, Perney TM (2001) Localization of two high-threshold potassium channel subunits in the rat central auditory system. *J Comp Neurol* 437:196–218.

Liao GS, Maillard M, Kiraly M (1991) Ion channels involved in the presynaptic hyperexcitability induced by herpes virus suis in rat superior cervical ganglion. *Neuroscience* 41:797–807.

Litovsky RY, Colburn HS, Yost WA, Guzman SJ (1999) The precedence effect. *J Acoust Soc Am* 106:1633–1654.

Livet J, Weissman TA, Kang H, Draft RW, Lu J, Bennis RA, Sanes JR, Lichtman JW (2007) Transgenic strategies for combinatorial expression of fluorescent proteins in the nervous system. *Nature* 450:56–62.

Lo DC, McAllister AK, Katz LC (1994) Neuronal transfection in brain slices using particle-mediated gene transfer. *Neuron* 13:1263–1268.

Loewy AD (1998) Viruses as transneuronal tracers for defining neural circuits. *Neurosci Biobehav Rev* 22:679–684.

Lois C, Refaeli Y, Qin XF, Parijs LV (2001) Retroviruses as tools to study the immune system. *Curr Opin Immunol* 13:496–504.

Lomniczi B, Watanabe S, Ben-Porat T, Kaplan AS (1987) Genome location and identification of functions defective in the bartha vaccine strain of pseudorabies virus. *J Virol* 61:796–801.

Lundstrom K (1999) Alphaviruses as tools in neurobiology and gene therapy. *J Recept Signal Transduct Res* 19:673–686.

Lycke E, Kristensson K, Svennerholm B, Vahlne A, Ziegler R (1984) Uptake and transport of herpes simplex virus in neurites of rat dorsal root ganglia cells in culture. *J Gen Virol* 65 (Pt 1):55–64.

Maier JK, Kindermann T, Grothe B, Klump GM (2008) Effects of omni-directional noise-exposure during hearing onset and age on auditory spatial resolution in the mongolian gerbil (meriones unguiculatus) – a behavioral approach. *Brain Res* 1220:47–57.

Maier JK, Klump GM (2006) Resolution in azimuth sound localization in the mongolian gerbil (meriones unguiculatus). *J Acoust Soc Am* 119:1029–1036.

Marie RLS, Shneiderman A, Stanforth DA (1997) Patterns of gamma-aminobutyric acid and glycine immunoreactivities reflect structural and functional differences of the cat lateral lemniscal nuclei. *J Comp Neurol* 389:264–276.

Markovitz NS, Pollak GD (1994) Binaural processing in the dorsal nucleus of the lateral lemniscus. *Hear Res* 73:121–140.

Martin X, Dolivo M (1983) Neuronal and transneuronal tracing in the trigeminal system of the rat using the herpes virus suis. *Brain Res* 273:253–276.

Mathie A, Wooltorton JR, Watkins CS (1998) Voltage-activated potassium channels in mammalian neurons and their block by novel pharmacological agents. *Gen Pharmacol* 30:13–24.

Matsumoto Y, ichi Katayama K, Okamoto T, Yamada K, Takashima N, Nagao S, Aruga J (2011) Impaired auditory-vestibular functions and behavioral abnormalities of slitrk6-deficient mice. *PLoS One* 6:e16497.

Mayer ML, Westbrook GL, Guthrie PB (1984) Voltage-dependent block by mg2+ of nmda responses in spinal cord neurones. *Nature* 309:261–263.

McAlpine D, Jiang D, Palmer AR (2001) A neural code for low-frequency sound localization in mammals. *Nat Neurosci* 4:396–401.

McAlpine D, Grothe B (2003) Sound localization and delay lines–do mammals fit the model? *Trends Neurosci* 26:347–350.

McBain CJ, Mayer ML (1994) N-methyl-d-aspartic acid receptor structure and function. *Physiol Rev* 74:723–760.

McCarthy KM, Tank DW, Enquist LW (2009) Pseudorabies virus infection alters neuronal activity and connectivity in vitro. *PLoS Pathog* 5:e1000640.

Meffin H, Grothe B (2009) Selective filtering to spurious localization cues in the mammalian auditory brainstem. *J Acoust Soc Am* 126:2437–2454.

Melloni RH, Hemmendinger LM, Hamos JE, DeGennaro LJ (1993) Synapsin i gene expression in the adult rat brain with comparative analysis of mrna and protein in the hippocampus. *J Comp Neurol* 327:507–520.

Merchán MA, Saldaña E, Plaza I (1994) Dorsal nucleus of the lateral lemniscus in the rat: concentric organization and tonotopic projection to the inferior colliculus. *J Comp Neurol* 342:259–278.

Mettenleiter TC, Lukàcs N, Rziha HJ (1985) Pseudorabies virus avirulent strains fail to express a major glycoprotein. *J Virol* 56:307–311.

Metts BA, Kaufman GD, Perachio AA (2006) Polysynaptic inputs to vestibular efferent neurons as revealed by viral transneuronal tracing. *Exp Brain Res* 172:261–274.

Meyer M, de Angelis MH, Wurst W, Kühn R (2010) Gene targeting by homologous recombination in mouse zygotes mediated by zinc-finger nucleases. *Proc Natl Acad Sci U S A* 107:15022–15026.

Mills A (1958) On the minimum audible angle. *JASA* 30:237–246.

Mistrík P, Mader R, Michalakis S, Weidinger M, Pfeifer A, Biel M (2005) The murine hcn3 gene encodes a hyperpolarization-activated cation channel with slow kinetics and unique response to cyclic nucleotides. *J Biol Chem* 280:27056–27061.

Moore B (1977) *An introduction to the psychology of hearing* Elsivier Science & Technology Books.

Moore JK, Moore RY (1987) Glutamic acid decarboxylase-like immunoreactivity in brainstem auditory nuclei of the rat. *J Comp Neurol* 260:157–174.

Moore MJ, Caspary DM (1983) Strychnine blocks binaural inhibition in lateral superior olivary neurons. *J Neurosci* 3:237–242.

Morest D (1966) cortical structure of the inferior quadrigeminal laminae of the cat:. *Anat Rec* 154:389.

Moser T, Beutner D (2000) Kinetics of exocytosis and endocytosis at the cochlear inner hair cell afferent synapse of the mouse. *Proc Natl Acad Sci U S A* 97:883–888.

Mysore SP, Knudsen EI (2012) Reciprocal inhibition of inhibition: a circuit motif for flexible categorization in stimulus selection. *Neuron* 73:193–205.

Nagel G, Szellas T, Huhn W, Kateriya S, Adeishvili N, Berthold P, Ollig D, Hegemann P, Bamberg E (2003) Channelrhodopsin-2, a directly light-gated cation-selective membrane channel. *Proc Natl Acad Sci U S A* 100:13940–13945.

Naldini L, Blömer U, Gallay P, Ory D, Mulligan R, Gage FH, Verma IM, Trono D (1996) In vivo gene delivery and stable transduction of nondividing cells by a lentiviral vector. *Science* 272:263–267.

Nathanson JL, Jappelli R, Scheeff ED, Manning G, Obata K, Brenner S, Callaway EM (2009) Short promoters in viral vectors drive selective expression in mammalian inhibitory neurons, but do not restrict activity to specific inhibitory cell-types. *Front Neural Circuits* 3:19.

Neumann E, Schaefer-Ridder M, Wang Y, Hofschneider PH (1982) Gene transfer into mouse lyoma cells by electroporation in high electric fields. *EMBO J* 1:841–845.

Nowak L, Bregestovski P, Ascher P, Herbet A, Prochiantz A (1984) Magnesium gates glutamate-activated channels in mouse central neurones. *Nature* 307:462–465.

Oliver DL, Shneiderman A (1989) An em study of the dorsal nucleus of the lateral lemniscus: inhibitory, commissural, synaptic connections between ascending auditory pathways. *J Neurosci* 9:967–982.

Oliver DL, Winer JA, Beckius GE, Marie RLS (1994) Morphology of gabaergic neurons in the inferior colliculus of the cat. *J Comp Neurol* 340:27–42.

Olkkonen VM, Liljeström P, Garoff H, Simons K, Dotti CG (1993) Expression of heterologous proteins in cultured rat hippocampal neurons using the semliki forest virus vector. *J Neurosci Res* 35:445–451.

Olsen LM, Ch'ng TH, Card JP, Enquist LW (2006) Role of pseudorabies virus us3 protein kinase during neuronal infection. *J Virol* 80:6387–6398.

Overholt EM, Rubel EW, Hyson RL (1992) A circuit for coding interaural time differences in the chick brainstem. *J Neurosci* 12:1698–1708.

Palmer AR, Russell IJ (1986) Phase-locking in the cochlear nerve of the guinea-pig and its relation to the receptor potential of inner hair-cells. *Hear Res* 24:1–15.

Park TJ, Klug A, Holinstat M, Grothe B (2004) Interaural level difference processing in the lateral superior olive and the inferior colliculus. *J Neurophysiol* 92:289–301.

Parks TN, Rubel EW (1975) Organization and development of brain stem auditory nuclei of the chicken: organization of projections from n. magnocellularis to n. laminaris. *J Comp Neurol* 164:435–448.

Payne KB, Jr. WRL, Thomas EM (1986) Infrasonic calls of the asian elephant (elephas maximus). *Behav Ecol Sociobiol* 18:297–301.

Pecka M, Brand A, Behrend O, Grothe B (2008) Interaural time difference processing in the mammalian medial superior olive: the role of glycinergic inhibition. *J Neurosci* 28:6914–6925.

Pecka M, Siveke I, Grothe B, Lesica NA (2010) Enhancement of itd coding within the initial stages of the auditory pathway. *J Neurophysiol* 103:38–46.

Pecka M, Zahn TP, Saunier-Rebori B, Siveke I, Felmy F, Wiegrebe L, Klug A, Pollak GD, Grothe B (2007) Inhibiting the inhibition: a neuronal network for sound localization in reverberant environments. *J Neurosci* 27:1782–1790.

Perrott DR, Saberi K (1990) Minimum audible angle thresholds for sources varying in both elevation and azimuth. *J Acoust Soc Am* 87:1728–1731.

Petreanu L, Huber D, Sobczyk A, Svoboda K (2007) Channelrhodopsin-2-assisted circuit mapping of long-range callosal projections. *Nat Neurosci* 10:663–668.

Petrovskis EA, Timmins JG, Gierman TM, Post LE (1986) Deletions in vaccine strains of pseudorabies virus and their effect on synthesis of glycoprotein gp63. *J Virol* 60:1166–1169.

Pfeifer A, Brandon EP, Kootstra N, Gage FH, Verma IM (2001) Delivery of the cre recombinase by a self-deleting lentiviral vector: efficient gene targeting in vivo. *Proc Natl Acad Sci U S A* 98:11450–11455.

Pollak GD, Burger RM, Klug A (2003) Dissecting the circuitry of the auditory system. *Trends Neurosci* 26:33–39.

Pomeranz LE, Reynolds AE, Hengartner CJ (2005) Molecular biology of pseudorabies virus: impact on neurovirology and veterinary medicine. *Microbiol Mol Biol Rev* 69:462–500.

Poole JH, Payne K, Jr. WRL, Moss CJ (1988) The social contexts of some very low frequency calls of african elephants. *Behav Ecol Sociobiol* 22:385–392.

Porres CP, Meyer EMM, Grothe B, Felmy F (2011) Nmda currents modulate the synaptic input-output functions of neurons in the dorsal nucleus of the lateral lemniscus in mongolian gerbils. *J Neurosci* 31:4511–4523.

Pusztai R, Gould EA, Smith H (1971) Infection patterns in mice of an avirulent and virulent strain of semliki forest virus. *Br J Exp Pathol* 52:669–677.

Rayleigh JWS (1907) On our perception of sound direction. *Philos Mag Series 6* 13:214–232.

Reyes AD, Rubel EW, Spain WJ (1996) In vitro analysis of optimal stimuli for phase-locking and time-delayed modulation of firing in avian nucleus laminaris neurons. *J Neurosci* 16:993–1007.

Rinaman L, Card JP, Enquist LW (1993) Spatiotemporal responses of astrocytes, ramified microglia, and brain macrophages to central neuronal infection with pseudorabies virus. *J Neurosci* 13:685–702.

Rinaman L, Levitt P, Card JP (2000) Progressive postnatal assembly of limbic-autonomic circuits revealed by central transneuronal transport of pseudorabies virus. *J Neurosci* 20:2731–2741.

Rockel AJ, Jones EG (1973) The neuronal organization of the inferior colliculus of the adult cat. i. the central nucleus. *J Comp Neurol* 147:11–60.

Rosenberger MH, Fremouw T, Casseday JH, Covey E (2003) Expression of the kv1.1 ion channel subunit in the auditory brainstem of the big brown bat, eptesicus fuscus. *J Comp Neurol* 462:101–120.

Saitoh N, Hori T, Takahashi T (2001) Activation of the epsilon isoform of protein kinase c in the mammalian nerve terminal. *Proc Natl Acad Sci U S A* 98:14017–14021.

Schlesinger S, Schlesinger JM (2001) *Togaviridae: the viruses and their replicatio. In: Fields virology.* Lippincott Williams & Wilkins.

Schneggenburger R, Meyer AC, Neher E (1999) Released fraction and total size of a pool of immediately available transmitter quanta at a calyx synapse. *Neuron* 23:399–409.

Schuller G, Radtke-Schuller S, Betz M (1986) A stereotaxic method for small animals using experimentally determined reference profiles. *J Neurosci Methods* 18:339–350.

Seidl AH, Grothe B (2005) Development of sound localization mechanisms in the mongolian gerbil is shaped by early acoustic experience. *J Neurophysiol* 94:1028–1036.

Seiler MJ, Sagdullaev BT, Woch G, Thomas BB, Aramant RB (2005) Transsynaptic virus tracing from host brain to subretinal transplants. *Eur J Neurosci* 21:161–172.

Shinn-Cunningham BG, Santarelli S, Kopco N (2000) Tori of confusion: binaural localization cues for sources within reach of a listener. *J Acoust Soc Am* 107:1627–1636.

Shneiderman A, Oliver DL, Henkel CK (1988) Connections of the dorsal nucleus of the lateral lemniscus: an inhibitory parallel pathway in the ascending auditory system? *J Comp Neurol* 276:188–208.

Shope RE (1932) Identity of the viruses causing "mad itch" and pseudorabies. *Exp Biol Med* 30 (3):308–309.

Siveke I, Leibold C, Grothe B (2007) Spectral composition of concurrent noise affects neuronal sensitivity to interaural time differences of tones in the dorsal nucleus of the lateral lemniscus. *J Neurophysiol* 98:2705–2715.

Siveke I, Pecka M, Seidl AH, Baudoux S, Grothe B (2006) Binaural response properties of low-frequency neurons in the gerbil dorsal nucleus of the lateral lemniscus. *J Neurophysiol* 96:1425–1440.

Smeraski CA, Sollars PJ, Ogilvie MD, Enquist LW, Pickard GE (2004) Suprachiasmatic nucleus input to autonomic circuits identified by retrograde transsynaptic transport of pseudorabies virus from the eye. *J Comp Neurol* 471:298–313.

Smerdou C, Liljeström P (1999) Non-viral amplification systems for gene transfer: vectors based on alphaviruses. *Curr Opin Mol Ther* 1:244–251.

Smith BN, Banfield BW, Smeraski CA, Wilcox CL, Dudek FE, Enquist LW, Pickard GE (2000) Pseudorabies virus expressing enhanced green fluorescent protein: A tool for in vitro electrophysiological analysis of transsynaptically labeled neurons in identified central nervous system circuits. *Proc Natl Acad Sci U S A* 97:9264–9269.

Smith PH, Joris PX, Yin TC (1993) Projections of physiologically characterized spherical bushy cell axons from the cochlear nucleus of the cat: evidence for delay lines to the medial superior olive. *J Comp Neurol* 331:245–260.

Smithburn KC, Haddow AJ (1944) Semliki forest virus: I. isolation and pathogenic properties. *J Immunol* 49:141–157.

Spangler KM, Warr WB, Henkel CK (1985) The projections of principal cells of the medial nucleus of the trapezoid body in the cat. *J Comp Neurol* 238:249–262.

Stanford TR, Kuwada S, Batra R (1992) A comparison of the interaural time sensitivity of neurons in the inferior colliculus and thalamus of the unanesthetized rabbit. *J Neurosci* 12:3200–3216.

Stein V, House DRC, Bredt DS, Nicoll RA (2003) Postsynaptic density-95 mimics and occludes hippocampal long-term potentiation and enhances long-term depression. *J Neurosci* 23:5503–5506.

Stotler WA (1953) An experimental study of the cells and connections of the superior olivary complex of the cat. *J Comp Neurol* 98:401–431.

Sukhovskaya LI (1966) Neuronal types and interneuronal connections of the inferior colliculus of the bat. *Arkhiv Anatomii, Gistologii i Embriologii,* 51:33.

Sun J, Bronk P, Liu X, Han W, Südhof TC (2006) Synapsins regulate use-dependent synaptic plasticity in the calyx of held by a ca2+/calmodulin-dependent pathway. *Proc Natl Acad Sci U S A* 103:2880–2885.

Taschenberger H, von Gersdorff H (2000) Fine-tuning an auditory synapse for speed and fidelity: developmental changes in presynaptic waveform, epsc kinetics, and synaptic plasticity. *J Neurosci* 20:9162–9173.

Taschenberger H, Scheuss V, Neher E (2005) Release kinetics, quantal parameters and their modulation during short-term depression at a developing synapse in the rat cns. *J Physiol* 568:513–537.

Thomas PB, Samant DM, Selvam S, Wei RH, Wang Y, Stevenson D, Schechter JE, Apparailly F, Mircheff AK, Trousdale MD (2010) Adeno-associated virus-mediated il-10 gene transfer suppresses lacrimal gland immunopathology in a rabbit model of autoimmune dacryoadenitis. *Invest Ophthalmol Vis Sci* 51:5137–5144.

Thompson AM, Thompson GC (1987) Efferent projections from posteroventral cochlear nucleus to lateral superior olive in guinea pig. *Brain Res* 421:382–386.

Thompson S (1882) On the function of the two ears in the perception of space. *Philos Mag Series 5* 13:406–416.

Thomson AM, West DC, Lodge D (1985) An n-methylaspartate receptor-mediated synapse in rat cerebral cortex: a site of action of ketamine? *Nature* 313:479–481.

Tirabassi RS, Townley RA, Eldridge MG, Enquist LW (1997) Characterization of pseudorabies virus mutants expressing carboxy-terminal truncations of ge: evidence for envelope incorporation, virulence, and neurotropism domains. *J Virol* 71:6455–6464.

Tiscornia G, Singer O, Ikawa M, Verma IM (2003) A general method for gene knockdown in mice by using lentiviral vectors expressing small interfering rna. *Proc Natl Acad Sci U S A* 100:1844–1848.

Tomishima MJ, Enquist LW (2002) In vivo egress of an alphaherpesvirus from axons. *J Virol* 76:8310–8317.

Trono D (2000) Lentiviral vectors: turning a deadly foe into a therapeutic agent. *Gene Ther* 7:20–23.

Tsuchitani C, Boudreau JC (1966) Single unit analysis of cat superior olive s segment with tonal stimuli. *J Neurophysiol* 29:684–697.

Ugolini G (2010) Advances in viral transneuronal tracing. *J Neurosci Methods* 194:2–20.

von Békésy G (1960) *Experiments in hearing.* New York, McGraw-Hill.

Vordermark D, Shibata T, Brown JM (2001) Green fluorescent protein is a suitable reporter of tumor hypoxia despite an oxygen requirement for chromophore formation. *Neoplasia* 3:527–534.

Wallach H, Newman EB, Rosenzweig MR (1949) The precedence effect in sound localization. *Am J Psychol* 62:315–336.

Walther W, Stein U (2000) Viral vectors for gene transfer: a review of their use in the treatment of human diseases. *Drugs* 60:249–271.

Weinberg JB, Matthews TJ, Cullen BR, Malim MH (1991) Productive human immunodeficiency virus type 1 (hiv-1) infection of nonproliferating human monocytes. *J Exp Med* 174:1477–1482.

Wickersham IR, Finke S, Conzelmann KK, Callaway EM (2007) Retrograde neuronal tracing with a deletion-mutant rabies virus. *Nat Methods* 4:47–49.

Wu SH, Kelly JB (1995) In vitro brain slice studies of the rat's dorsal nucleus of the lateral lemniscus. ii. physiological properties of biocytin-labeled neurons. *J Neurophysiol* 73:794–809.

Wu SH, Kelly JB (1996) In vitro brain slice studies of the rat's dorsal nucleus of the lateral lemniscus. iii. synaptic pharmacology. *J Neurophysiol* 75:1271–1282.

Yang L, Pollak GD (1994) The roles of gabaergic and glycinergic inhibition on binaural processing in the dorsal nucleus of the lateral lemniscus of the mustache bat. *J Neurophysiol* 71:1999–2013.

Yang L, Pollak GD (1998) Features of ipsilaterally evoked inhibition in the dorsal nucleus of the lateral lemniscus. *Hear Res* 122:125–141.

Yang M, Card JP, Tirabassi RS, Miselis RR, Enquist LW (1999) Retrograde, transneuronal spread of pseudorabies virus in defined neuronal circuitry of the rat brain is facilitated by ge mutations that reduce virulence. *J Virol* 73:4350–4359.

Yin TC, Carney LH, Joris PX (1990) Interaural time sensitivity in the inferior colliculus of the albino cat. *J Comp Neurol* 295:438–448.

Yizhar O, Fenno LE, Davidson TJ, Mogri M, Deisseroth K (2011) Optogenetics in neural systems. *Neuron* 71:9–34.

Yost WA, Wightman FL, Green DM (1971) Lateralization of filtered clicks. *J Acoust Soc Am* 50:1526–1531.

Zaiss AK, Liu Q, Bowen GP, Wong NCW, Bartlett JS, Muruve DA (2002) Differential activation of innate immune responses by adenovirus and adeno-associated virus vectors. *J Virol* 76:4580–4590.

Zeilhofer HU, Swandulla D, Geisslinger G, Brune K (1992) Differential effects of ketamine enantiomers on nmda receptor currents in cultured neurons. *Eur J Pharmacol* 213:155–158.

Zhang F, Wang LP, Brauner M, Liewald JF, Kay K, Watzke N, Wood PG, Bamberg E, Nagel G, Gottschalk A, Deisseroth K (2007) Multimodal fast optical interrogation of neural circuitry. *Nature* 446:633–639.

Zhang K, Sejnowski TJ (1999) Neuronal tuning: To sharpen or broaden? *Neural Comput* 11:75–84.

Zufferey R, Nagy D, Mandel RJ, Naldini L, Trono D (1997) Multiply attenuated lentiviral vector achieves efficient gene delivery in vivo. *Nat Biotechnol* 15:871–875.

List of Figures

Abbreviations

4-AP	4-aminopyridine
AAV	adeno associated virus
AFN	antagonist of MMF consisting of Atipamezol/Flumazenil/Naloxon
AMPA	(2-amino-3-(5-methyl-3-oxo-1,2-oxazol-4-yl)propanoic acid)
AMPAR	AMPA receptor
aoi	area of interest
AVCN	anteroventral cochlear nucleus
CamKII	CamKinase II promoter
CamKII-α	calmodulin dependent kinase II alpha
CamKIIChR2	lentivirus with CamKII promoter, coding for GFP tagged to ChR2
ChR2	hhannelrhodopsin-2, a light-sensitive ion channel
CMV	cytomegalovirus immediate early promoter
CN	cochlear nucleus
CPP	NMDA receptor antagonist (3-(2-Carboxypiperazin-4-yl)propyl-1-phosphonic acid)
D-AP5	NMDA receptor antagonist (D-2-Amino-5-phosphonovalerate)
DNLL	dorsal nucleus of the lateral lemniscus
DNQX	AMPA and Kainat receptor antagonist, 6,7-dinitroquinoxaline-2,3-dione
dpi	days post injection
EI neuron	Neurons, which are excited by one ear and inhibited by the other.
EPSC	miniature excitatory postsynaptic current
EPSP	miniature excitatory postsynaptic potential
Fluo-4	fluorescent calcium indicator
GFP	green fluorescent protein
hpi	hours post injection
IC	inferior colliculus
IID	interaural intensity difference

IO-F	input-output function
ITD	interaural time difference
LNTB	lateral nucleus of the trapezoid body
LSO	lateral superior olive
MAP2	microtubule associated protein 2
mEPSC	miniature excitatory postsynaptic current
MMF	anaesthetic consisting of Medetomidin/Midazolam/Fentanyl
MNTB	medial nucleus of the trapezoid body
mRFP1	monomeric red fluorescent protein 1
MSO	medial superior olive
NMDA	N-methyl-D-aspartic acid
NMDAR	NMDA receptor
NpHR	halorhodopsin of *Natronomonas pharaonis* , a light-sensitive proton pump
P	postnatal day
PBS	phosphate buffered saline
PFA	paraformaldehyde
PI	persistent inhibition
PK15	pig kidney cell line 15
PRV	pseudorabies virus
PRV152	eGFP expressing PRV-Bartha strain
PRV614	mRFP1 expressing PRV-Bartha strain
roi	region of interest
RT	room temperature
S100β	β subunit of the S100 protein
SFV	Semliki Forest virus
simEPSC	simulated EPSC, a previously recorded AMPA mediated EPSC was background corrected, scaled to different sizes and then current injected into a patched cell as command template
simEPSP	simulated EPSP, previously recorded EPSPs were background corrected and then injected as a command template into a patched cell from a holding potential of -60 mV
SOC	superior olivary complex
SR95531	SR95531 hydrobromide
SynChR2	lentivirus with synaspin 1 promoter, coding for GFP tagged to ChR2
SynGFP	lentivirus with synaspin 1 promoter, coding for eGFP

SynNpHR	lentivirus with synaspin 1 promoter, coding for eGFP tagged to NpHR
TEA	tetraethylammonium chloride
TTX	sodium channel blocker, Tetrodotoxin
ZD7288	4-(N-ethyl-N-phenylamino)-1,2-dimethyl-6-(methylamino) pyrimidinium chloride

Danksagung

Ich danke Benedikt Grothe für die Möglichkeit, daß ich meine Dissertation in seiner Arbeitsgruppe anfertigen konnte und für die Unterstützung die ich während dieser Zeit erhalten habe.
Bei Achim Klug bedanke ich mich für das erste Jahr der Betreuung bis zu seinem Weggang nach Denver, CO, USA.
Besonderer Dank gilt Felix Felmy dafür, daß er sich um den herrenlosen Doktoranden gekümmert hat, für einen Großteil dessen, was ich in den letzten Jahren gelernt habe, für Pizza und Bier und für die Geduld, die er während meiner Schreibtätigkeit aufgebracht hat.

Bedanken möchte ich mich außerdem bei allen Mitarbeitern der neurobiologischen Abteilung des Department Biologie II. Namentlich erwähnt werden sollen hier vor allem jene, denen oft nicht genug gedankt wird, deren Arbeit und Mithilfe aber einen großen Teil zum Gelingen von Veröffentlichungen und Dissertationen beitragen: Claudia Aerdker, Olga Alexandrova, Maj-Cahterine Botheroyd, Simone Fischer, Monika Holik, Horst König, Dieter Leippert, Andrea Okolie, Nadschman Rahimi, Sabrina Schenk, Melanie Sotgia, Kristina Vaupel, Hilde Wohlfrom.
Dank für das Korrekturlesen der Arbeit und für hilfreiche Verbesserungsvorschläge gilt: Julian Ammer, Kiri Couchman, Lars Kunz und Moritz Paehler.

Besonderer Dank gilt den Freunden, Mitdoktoranden und anderen Labormitgliedern, die durch ihren steten Einsatz sowohl im, als auch außerhalb des Labors geholfen haben wissenschaftliche Probleme zu lösen oder einfach nur dazu beigetragen haben die Situation erträglich zu gestalten. Hervorgehoben werden müssen hier vor allem die “Schwabenland-Australien-Konnektion” und die Doktoranden-WG von gegenüber. Ebenso muß hier Felix Oppermann erwähnt werden, der sowohl seine Wohnung als Schreibstube zur Verfügung gestellt, als auch tatkräftig bei der Bekämpfung von Schreibblockaden im Mariandl geholfen hat.

Ich danke meiner Familie, die mich stets unterstützt hat.

Eidesstattliche Versicherung

Hiermit versichere ich an Eides statt, daß die hier vorliegende Dissertation von mir selbständig und ohne unerlaubte Hilfe angefertigt wurde. Ich habe weder anderweitig versucht diese Dissertation einzureichen, noch habe ich Teile derselben einer anderen Prüfungskommission vorgelegt.

Christian Porres

München, den 8. November 2012